Università degli Studi della Basilicata

International Ph.D. programme in

"Applied Biology and Environmental Safeguard"

Rare Earth Elements distribution and geochemical behavior in the Mt. Vulture volcanic groundwater, southern Italy

Scientific Disciplinary sector

"GEO/08

PhD Coordinator

Prof.ssa Patrizia FALABELLA

Supervisor

Prof. Giovanni MONGELLI

Co-Supervisor

Dr. Michele PATERNOSTER

PhD candidate

Ferdinando DELUCA

Cycle: XXXIII

Dedicated to Simona and Samuele

Summary

ABSTRACT

The Mount Vulture basin is one of the most important aquifers for drinking water and irrigation supply in southern Italy. The volcanic aquifer mainly consists of pyroclastic and subordinate lava flow layers. Aim of this study is to investigate for the first time the REEs' geochemical behaviour in the Mount Vulture groundwater assessing concentrations and fractionation patterns and performing speciation calculation, in order to verify whether REEs' geochemistry records the geochemical processes occurring in this aquatic system. The study will also discuss the flow system of the groundwater's basin and possible controls on the REEs' distribution along the studied groundwater flow paths in the Mt Vulture.

The water samples were collected from springs and drilled wells during a field trip in the dry season to record the highest concentration of dissolved elements. A cluster analysis highlights the existence of two main subsets: a high EC (HEC, average EC = 2,495 µs/cm) subset with lower pH (average = 6.12), Eh (average = 421 mV), and DO (average = 2.48 µmol/kg), and higher T (average = 18.7 °C) values; and a low EC (LEC, average EC = 382 µs/cm) characterised by higher pH (average = 6.50), Eh (average = 543 mV), and DO (average = 7.31 µmol/kg), and lower T values (average = 15.4 °C). In the HEC subset, the Na^+ and HCO_3^- are significantly higher (Na^+ average = 410.7 mg/l, HCO_3^- average = 1176.6 mg/l) than in the LEC subset (Na^+ average = 31.7 mg/l, HCO_3^- average = 198.6 mg/l). That suggests that the HEC and LEC waters correspond roughly to the waters from the discharge zone and recharge zone, respectively.

Overall, the groundwater exhibited REE concentrations well below 1000 ng/l, and the average content measured in the discharge water is approximately three times higher than that of the recharge water. In the recharge water, the shale normalised patterns are characterised by a more negative average Ce anomaly ($logCe^*_{PAAS} = -0.56$), a more positive average Eu anomaly ($logEu^*_{PAAS} = 0.75$), and a larger average $(La/Yb)_{PAAS}$ ($log(La/Yb)_{PAAS} = -0.12$).

The observed relationship between Ce anomalies (Ce*) and dissolved oxygen (DO) supports the idea that Ce oxidative scavenging, probably involving Fe/Mn oxyhydroxides, has a role in determining the size and shape of the Ce^*. Further, the less negative average size of the Ce* in the discharge zone also suggests desorption of Ce as Ce^{3+}, according to previous findings on the content of dissolved Fe and Mn. The desorption is related to changes in redox conditions, according to the lower Eh and DO average values observed in the discharge zone compared to

the recharge zone. The lack of a significant correlation between Eh and Ce anomalies indicates that, in addition to the aqueous chemistry, the source composition affects Ce*.

Although a significant correlation is observed between Eu anomalies (Eu*) and Eh and DO, the strongly reducing condition promoting Eu^{3+} and Eu^{2+} is never attained in the Mt. Vulture aquifer. The largest Eu* are associated with the recharge zone where the average Eh and DO values are higher. The volcanics occurring in the Mt. Vulture lithologies are characterised by PAAS-normalised patterns with positive Eu anomalies due to the presence of feldspars. This constraint indicates that, in the recharge zone, the size and shape of the Eu* of groundwater are largely due to the dissolution of feldspars. In the discharge zone, most samples are in equilibrium in terms of smectite content, and Eu^{2+} adsorption onto the clay phase surface or its inclusion in the mineral structure as an exchangeable cation, due to vicariance with Ca^{2+} and Sr^{2+}, could explain the smaller average size of the Eu anomaly.

Further, the occurrence of secondary minerals preferentially scavenging LREE also explains the difference in the LREE/HREE fractionation, indicated by the $(La/Yb)_{PAAS}$ index and observed between the recharge and discharge zones.

Finally, speciation calculations reveal that dissolved REEs consist mainly of carbonato complexes ($LnCO_3^+$), whereas the percentage of the dicarbonato complexes ($Ln(CO_3)_2^-$) increases in samples with circa-neutral pH. At acidic pH, the Ln^{3+} species are important, and, in the samples from discharge zone affected by a large amount of dissolved sulphate derived by feldspathoids dissolution, the percentage of $LnSO_4^+$ species is not negligible.

Overall the REEs' distribution in the Mt. Vulture aquifer is originated by several mechanisms, including weathering reactions involving volcanic rocks, the occurrence of secondary minerals, and pH and redox control. Therefore, the REEs' geochemistry is a powerful tool in assessing the geochemical processes affecting the groundwater environment.

INTRODUCTION

Drinking water is a natural resource of increasing importance due to an intensifying demand. Therefore, its major and trace elements content, as well as the environment influence on its composition, are of special interest (Gob et al., 2013). The chemical composition of natural water is determined by the interaction with rocks at depth (Frape et al., 2003; Bucher and Stober, 2010) or soil (Aubert et al., 2002) and by anthropogenic impacts (Kulaksiz and Bau, 2013). For the protection and safe use of groundwater, it is important to recognize water origin, circulation patterns and environmental influence.

In this scenario, Rare earth elements (REEs) distribution in groundwater has gained growing attention due to the capability of this group, also consequently to the improvement of analysis accuracy (e.g. Willis and Johannesson, 2011; Yuan et al., 2014), to elucidate water-rock interaction (Dia et al., 2000; Leybourne et al., 2000; Hannigan and Sholkovitz, 2001; Worrall et al., 2001; Biddau et al., 2002; Munemoto et al., 2015). In addition, the REEs distribution in groundwater provides important information about physico-chemical conditions of the aqueous system (Janssen and Verweij, 2003; Otsuda and Terakado, 2003; Gruau et al., 2004; Johannesson et al., 2004; Tang and Johannesson, 2003, 2006; Choi et al., 2009; Johannesson et al., 2005, 2011; Marsac et al., 2011; Stolpe et al., 2013; Davranche et al., 2015), and groundwater flow paths and mixing (Johannesson et al., 1997, 1999; Ojiambo et al., 2003; Tweed et al., 2006; Guo et al., 2010; Siebert et al., 2012).

REEs' content in aqueous systems strongly depends on the degree of rock weathering (Moller, 2002). However, after REEs' dissolution from the aquifer rocks, REEs' removal from solution by sorption and coprecipitation can occur. Therefore, in groundwater REEs' concentrations and fractionations patterns (e.g. Noack et al., 2014 and reference therein) are capable to add valuable constraints on the evolutions experienced by the aquatic system during the flow in the aquifer rock(s). In this respect, besides sorption mechanism (Liu et al., 2017, 2018, and reference therein), the redox conditions, which may strongly affect the occurrence and the size of both the Ce and Eu anomalies in groundwater (Smedley, 1991; Leybourne et al., 2000; Duncan and Shaw, 2003; Gruau et al., 2004; Pourret et al., 2010; Guo et al., 2010; Yuan et al., 2014), as well as, complexation processes (e.g. Johannesson et al., 1999; Dia et al., 2000; Willis and Johannesson, 2011; Munemoto et al., 2015; Liu et al., 2016) can result in extensive fractionation between the dissolved REE composition of groundwaters and that of the parent rocks during the flow path.

It has to stress that, within this general scenario, there are relatively few studies on the concentration and distribution patterns of REEs in CO_2-rich groundwater (Négrel et al., 2000; Möller et al. 2004, Choi et al., 2009).

In southern Italy, the Mt. Vulture hydro-mineral basin represents one of the most important aquifer systems, pumped for drinking and irrigation supply. The aquifer core is mainly composed of pyroclastic and subordinate lava flow layers of different permeability, which give rise to distinct aquifer layers. The principal hydrogeological complexes are therefore volcanic products, with high-medium permeability values. The structural hydraulic parameters and anisotropy features of the aquifer are the major factors that control groundwater flow pathways (Parisi et al., 2011a; Paternoster et al., 2016). The tectonic discontinuities act as deep preferential groundwater flow and promote the mineralization processes of groundwater (Paternoster et al., 2010).

The input of CO_2-rich volcanic gases strongly influences the groundwater chemistry in the Mt. Vulture area, which is heterogeneous between different sectors.

In the Mt. Vulture basin, they have recognized two different water types so far: a bicarbonate alkaline-earth and alkaline type and sulfate-bicarbonate alkaline type (Paternoster, 2019 and reference therein). The differences in composition suggest to be related to the complex geological and hydrogeological contexts of the system, involving water interaction with different aquifer rocks (Parisi et al., 2011b).

The following study aims to investigate for the first time the REEs' geochemical behaviour in the Mount Vulture groundwater assessing concentrations and fractionation patterns and performing speciation calculation, in order to verify whether REEs' geochemistry records the geochemical processes occurring in this aquatic system. The study will also discuss the flow system of the groundwater's basin and possible controls on the REEs' distribution along the studied groundwater flow paths in the Mt Vulture.

CHAPTER 1
RARE EARTH ELEMENTS (REEs)

1.1 Rare Earth Elements (REEs)

The Rare Earth Element (hereafter REEs) are 15 elements (Tab.1) that range in atomic number from 57 (lanthanum) to 71 (lutetium); they are commonly referred to as the "lanthanides". The REE promethium (atomic number 61) is not included in discussion of REE because the element is extremely rare and unstable in nature. In addition, Yttrium (atomic number 39) is commonly regarded as an REE because it shares chemical and physical similarities and has affinities with the lanthanides (Van Gosen et al., 2017).

So REE are (ordered by their atomic number): 57 – Lanthanum (La); 58 – Cerium (Ce); 59 – Praseodymium (Pr); 60 – Neodymium (Nd); 61 – Promethium (Pm); 62 – Samarium (Sm); 63 – Europium (Eu); 64 – Gadolinium (Gd); 65 – Terbium (Tb); 66 – Dysprosium (Dy); 67 – Holmium (Ho); 68 – Erbium (Er); 69 – Thulium (Tm); 70 – Ytterbium (Yb); 71 – Lutetium (Lu). Traditionally, they divide into three groups: Light Rare Earth Elements (LREE), from lanthanum to promethium; Medium Rare Earth Elements (MREE), from samarium to holmium; and Heavy Rare Earth Elements (HREE), from erbium to lutetium.

Table 1 *– lanthanide (REE) symbols, atomic weight, and ionic radius for coordination number 6 (Shannon, 1976).*

	SYMBOL	**ATOMIC NUMBER** ($g\ mol^{-1}$)	**IONIC RADIUS** (Å)
Lanthanum	La	138.9	1.03
Cerium	Ce	140.1	1.01
Praseodymium	Pr	140.9	0.99
Neodymium	Nd	144.2	0.98
Promethium	Pr		
Samarium	Sm	150.4	0.96
Europium	Eu	152	0.95
Gadolinium	Gd	157.2	0.94
Terbium	Tb	158.9	0.92
Dysprosium	Dy	162.5	0.91
Holmium	Ho	164.9	0.9
Erbium	Er	167.3	0.89
Thulium	Tm	168.9	0.88
Ytterbium	Yb	173	0.87
Lutetium	Lu	175	0.86

Most of the REEs are not as rare as the group's name suggests. We name them "rare earth" elements because during the 18^{th} and 19^{th} centuries, most of them were identified as "earths", and, in comparison with other "earths", such as lime or magnesia, they were relatively rare (Van Gosen et al., 2017). Cerium is the most abundant REE, and it is actually more common in Earth's crust than is copper or lead (Lide, 2004).

All the REEs except promethium are more abundant than silver, gold or platinum in Earth's crust, on average (Lide, 2004). Thus, REEs are not rare in terms of average crustal abundance but concentrated and economic deposits of REEs are unusual (Adams and Staatz, 1973).

1.1.1 REEs geochemistry

All REEs are cations and electropositive and are commonly found together in Earth's crust because they share a trivalent charge ($REEs^{3+}$) and similar ionic radii. Exceptions to the trivalent charge are cerium, which may occur in a Ce^{4+} valence state and europium which can exist as Eu^{2+} (Van Gosen et al., 2017). Moreover, the lanthanides (lanthanum to lutetium) have a unique property referred to as "Lanthanide contraction" (a term coined by Norwegian geochemist Victor Goldschmidt). With each increase in the atomic number across the lanthanides group, we add an electron to an inner incomplete subshell (4*f*) rather than an outer level. This property of selectively filling inner levels results in a progressive decrease in the ionic radius of the trivalent lanthanides ions from La^{3+} to Lu^{3+} (Fig.1).

The lanthanide contraction has two significant consequences: (1) it affects the fractionations of the REEs to a high degree, which allows for their individual separation in geological environments and in ore processing, and (2) it leads the REEs unusual and useful chemical and physical properties, such as unique magnetic and (or) optical properties (Van Gosen et al., 2017).

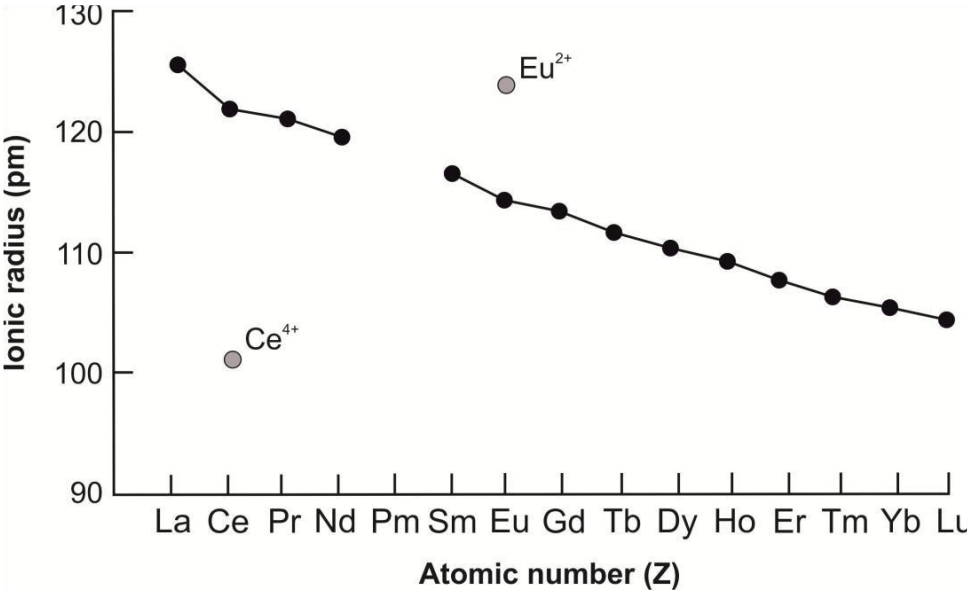

Figure 1 *– example of lanthanidic contraction.*

In addition to the lanthanide contraction, REE abundances reflect the Oddo-Harkins rule (Fig.2): REE with even atomic numbers have greater cosmic and terrestrial abundances then adjacent REE with odd atomic numbers. Therefore, LREEs are more strongly concentrated in the continental crust than the HREEs (Fig.3).

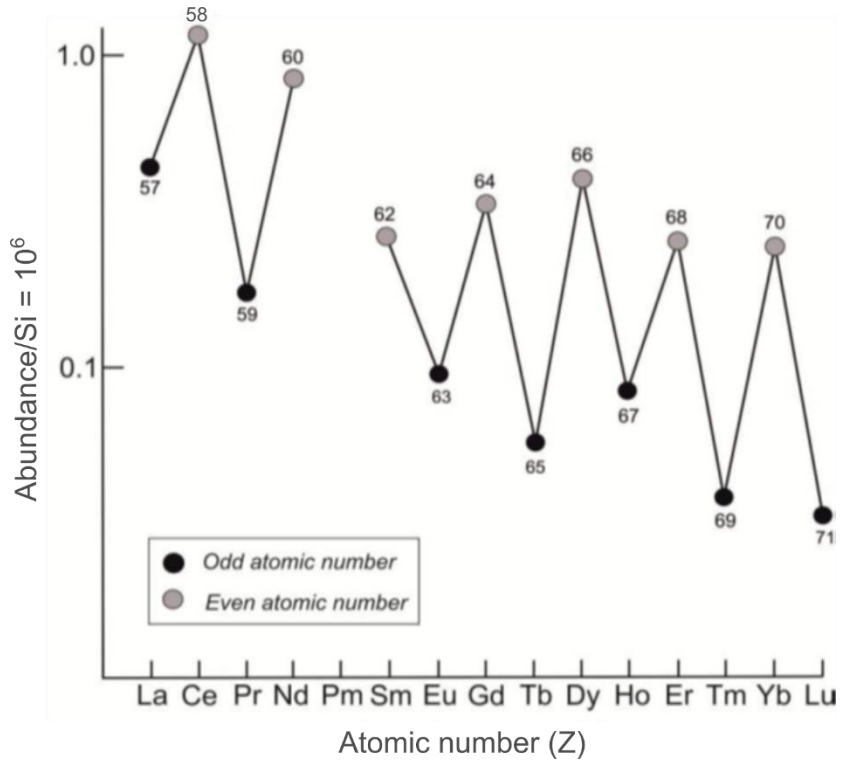

Figure 2 *– example of Hoddo – Harkins effect.*

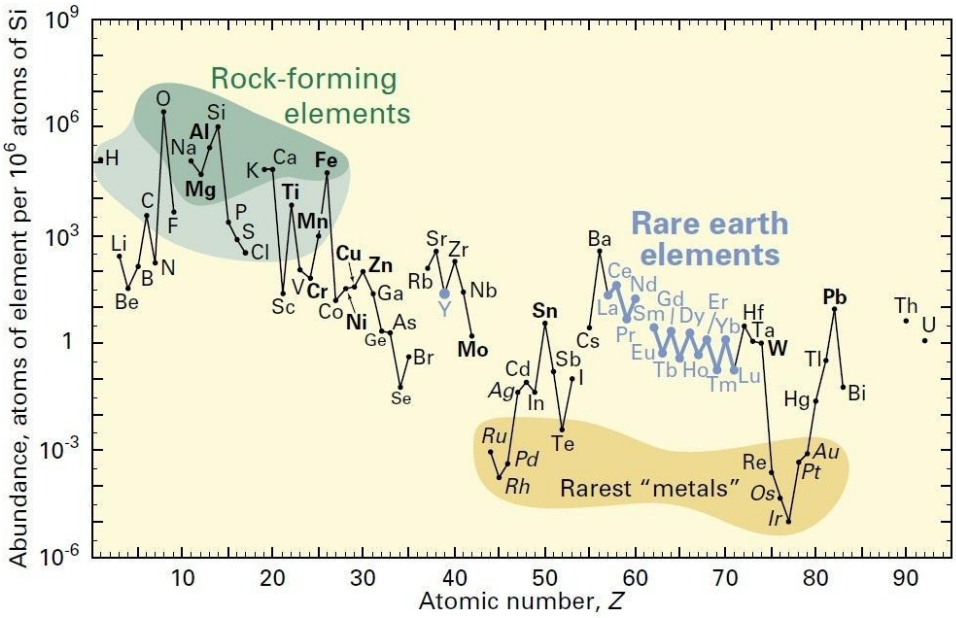

Figure 3 *– rare earth elements abundances in the Earth's crust (USGS).*

In magmatic systems, the high-charge of the REEs cations hinders the aptitude of these elements to achieve charge balance and fit into the structure of the common rock-forming minerals, which have coordination sites best suited for valence state of 2 or 1. As a result, when common silicate minerals (such as amphiboles, feldspars, and olivine) crystallize, most of the REEs tend to remain in the coexisting melt. In contrast, europium often depletes in magmas because it is incorporated into feldspar owing to its Eu^{2+} valence state. Successive generations of this process referred to as crystal fractionations, increase the concentrations of REEs in the remaining melt until individual REE-mineral-rich phases crystallize (Van Gosen et al., 2017). Other factors such as temperature, pressure, fluid composition, magmatic convection, and variation in mineral settling velocities can affect the partitioning of the REEs between a mineral and the coexisting magma in addition to valence state (Henderson, 1984; McKay, 1989; Kogarko et al., 2006).

In most rock-forming processes the REE are dispersed as minor or trace constituents of phases in which they are not essential components. Nevertheless, all minerals could be divided into three main groups according to their total REE content:

1) Minerals usually with very low REE concentrations. These include many of the common rock-forming minerals.
2) Minerals containing minor amounts of REE, but not as essential constituents. Around 200 minerals contain more than 0.01 wt.% of the REE (Herrmann, 1970).

3) Minerals with major and usually essential contents of the REE. Over 70 minerals fall in this category and include all the REE species together with a few minerals, which are lanthanide-rich equivalents of low-REE minerals, such as allanite and yttrofluorite (REE varieties of epidote and fluorite, respectively).

Igneous rocks can contain several hundred parts per million of the lanthanides, distributed across both the major and accessory minerals (Henderson, 2013). Many of the REEs world deposits are associated with carbonatites, which are igneous rocks derived from carbonate-rich magmas rather than silica-rich magmas. This type of rocks has the highest REE concentrations of any igneous rocks (Chakhmouradian and Zaitsev, 2012). In addition to carbonatites, the REEs have a strong genetic association with alkaline igneous processes, particularly peralkaline magmatism. Alkaline igneous rocks crystallize from silicate magmas and fluids enriched in alkali elements and precipitate sodium- and potassium-bearing minerals, such as sodium- or potassium-rich amphiboles and pyroxenes. Typically, alkaline igneous rocks are undersaturated in silica so they could contain a little of quartz or none. Peralkaline igneous rocks are associated with enrichments in REEs, typically more than most other igneous rocks.

In sedimentary rocks, such as carbonates and sandstones, clay minerals are usually present in abundance. The latter have much higher REE concentrations than carbonate minerals or quartz and may therefore contain the bulk of the REE in the rock as whole. The phyllosilicate minerals (the clay and mica groups) do not concentrate the REE in igneous rocks, but acquire them through surface adsorption as clays developed during weathering (Roaldset, 1975). Clay minerals, as products of weathering of igneous minerals, tend to inherit and average the REE distributions of their sources.

1.2 .1 Aqueous geochemistry of Rare Earth Elements

In aquatic systems, due to their slight solubility, REE concentrations are low, if we compare them to REE concentrations in rocks. We ascribe the REE abundance in groundwater to the interaction- along flow paths- with REE-bearing minerals, and it varies with groundwater conditions including pH, redox conditions, and dissolved anions (Johannesson et al., 1999; Smedley, 1991, Inguaggiato et al., 2015; Munemoto et al., 2015; Oliveri et al., 2019). However, global REE variability in natural groundwater is very complex and dependent on local geology, water flow paths mixing and chemical condition of groundwater (Noak et al., 2014).

In the last years, with the development of inductively coupled plasma – mass spectrometry (ICP-MS), analysis of REEs in aqueous solutions has become routines and consequently the number of studies that analysed and interpreted REEs behaviour in different groundwater environments has increased substantially (Willis and Johannesson, 2011; Yuan et al., 2014; Van Gosen et al., 2017; Liu et al., 2019).

Numerous studies suggest that the solution and interface chemistry are the major controlling factors of the REE concentration in aquatic systems (Goldstein and Jacobsen, 1988; Elderfield et al., 1990; Sholkovitz, 1995, Tweed et al., 2006; Devranche et al., 2016). For example, groundwater REE signatures have been shown to reflect those of host aquifers, and are, therefore, useful tracers of flow where the mineralogy of different aquifers varies (e.g. Smedley, 1991; Johannesson et al., 1997a, b, 2000; Takahashi et al., 2002; Moller et al., 2003; Inguaggiato et al, 2015; Oliveri et al., 2019). However, subsequent to REE dissolution from the aquifer rocks, processes such as REE co-precipitation with secondary minerals (Patino et al., 2003; Tweed et al., 2006; Inguaggiato et al., 2015; Oliveri et al., 2019), REE adsorption onto ferromanganese oxides (Leybourne et al., 2008), and ferromanganese precipitation (Ohta and Kawabe, 2001) sequestrate, largely, the aqueous REE from bulk solution. Bau (1999) showed that the scavenged REE increased from approximately 10% at pH < 4.6 to more than 90% at pH > 6 in the presence of dissolved Fe oxyhydroxide.

The decrease in ionic radius with atomic number (La^{3+} = 1.03 Å, Lu = 0.861 Å) can result in preferential sorption of LREEs while HREEs remain in solution (e.g. Byrne and Kim, 1990; Smedley, 1991; Johannesson et al., 2000; Biddau et al., 2002). In addition, the formation of complexes influences the stability of REEs in solution. REE can form strong complexes with a number of different ligands like carbonate complexes (Johannesson et al., 1997a, 1999 and 2000; Inguaggiato et al., 2015), sulphate ion complexes (Johannesson et al., 1996; Inguaggiato et al., 2015, 2017; Oliveri et al., 2019), and phosphate ion complexes (Lee and Byrne, 1992). Water is a strong ligand for trivalent (REE^{3+}) and therefore forms a hydration shell around the REE^{3+} ions. The number of water molecules that a REE^{3+} can bind varies between 8 and 9, depending on the element and species considered (Ohta et al., 2008). In aqueous environments, water molecules displace only if ligands with a small ionic radius are present at a high oxidation state and with high electronegativity. In general, REE^{3+} ions prefer donor atoms in the following order of affinity: O > N > S. The resulting chemical species tend to form mainly ionic bonds with REE within their unoccupied lower high-energy orbitals (Weber 2008). Furthermore, the solution complexation and partition coefficients, describing the sorption of REE on amorphous

ferric hydroxide, are influenced by dissolved carbonate ion (CO_3^{2-}) (Kawabe et al., 1999; Ohta and Kawabe, 2000; Quinn et al., 2006). The enhanced REE solution complexation by carbonate ions was reported to be a mechanism of the Fe distribution coefficient decrease (Quinn et al., 2006). REE showed greater affinity for Mn oxides as compared to Fe oxides (Liu et al., 2018). However, complexation with both of these oxides could be a bet sink of aqueous REE (German and Elderfield, 1990). The REE sorptive behaviour showed a preferential uptake by Mn oxides of LREE relative to HREE that resulted in a LREE enrichment in the solid phase (Koeppenkastrop and De Carlo, 1992).

1.2.1.1 Normalized REE patterns

Usually, for the sake of convenience, the REE distribution in water and in natural materials is reported as normalized REE patterns. Two geological reservoirs are used for the normalization, the shales and upper continental crust. Therefore, the REE abundance is normalized to the Post-Archean Australian Shale, PAAS (McLennan, 1989), North American shale composite, NASC (Gromet et al., 1984), or upper continental crust, UCC (Taylor and McLennan, 1985).

A normalized REE pattern allows for the recognition of an anomalous concentration for an individual REE as a positive or negative anomaly in an otherwise smooth pattern. This kind of anomaly can occur in response to the redox behaviour of Ce and Eu quantified via Ce and Eu anomalies such as Ce*= Ce(N)/$\sqrt{La(N) \times Pr(N)}$ and Eu* = Eu(N)/$\sqrt{Sm(N) \times Gd(N)}$ with N equal to the normalized abundance. Process that convert Ce^{3+} to Ce^{4+} include biologically mediated oxidation (Moffett, 1990, 1994a, b) and abiotic oxidations on the surfaces of Mn oxides (Koeppenkastrop and De Carlo, 1992; Sholkovitz et al., 1994; Ohta and Kawabe, 2001). The reductions of Eu generally occurs a high temperatures and pressures, such as in hydrothermal fluids (e.g., Michard et al., 1983; German et al., 1991; Klinkhammer et al., 1994).

Therefore, the REE pattern results from the combination of several processes able to induce their fractionation like precipitation/dissolution, sorption onto colloids and particles and complexation in solution with organic and inorganic ligands. Thus, the REE patterns correspond to the REE pattern for the mineral sources modified by the sorption/complexation constants of REE with ligands, colloids and particles. The result is highly diverse REE patterns that can be measured by a degree of depletion or enrichment relative to heavy REE (La/Yb or Sm/Yb ratios) or by whether or not anomalies are present (Davranche et al., 2015, 2016; Inguaggiato et al., 2015; Oliveri et al., 2019).

CHAPTER 2
GEOLOGICAL SETTING

2.1 Regional geological setting

The southern Apennine is an east-verging orogenic chain formed along the western edge of the Apula microplate from Oligocene (Schiattarella et al., 2005). It is the segment of the circum-Mediterranean orogenic system between the central Apennine to the north and the Calabria-Peloritani arc to the south, bounded by the *Ortona-Roccamonfina* and the *Sangineto* tectonic lines (Fig.4). Processes related to the genesis of the Tyrrhenian-Apenninic-Adriatic system governed the evolution of the accretionary wedge. The Apennine deformation took place during the Neogene until the lower Pliocene with an initial compressional deformation phase.

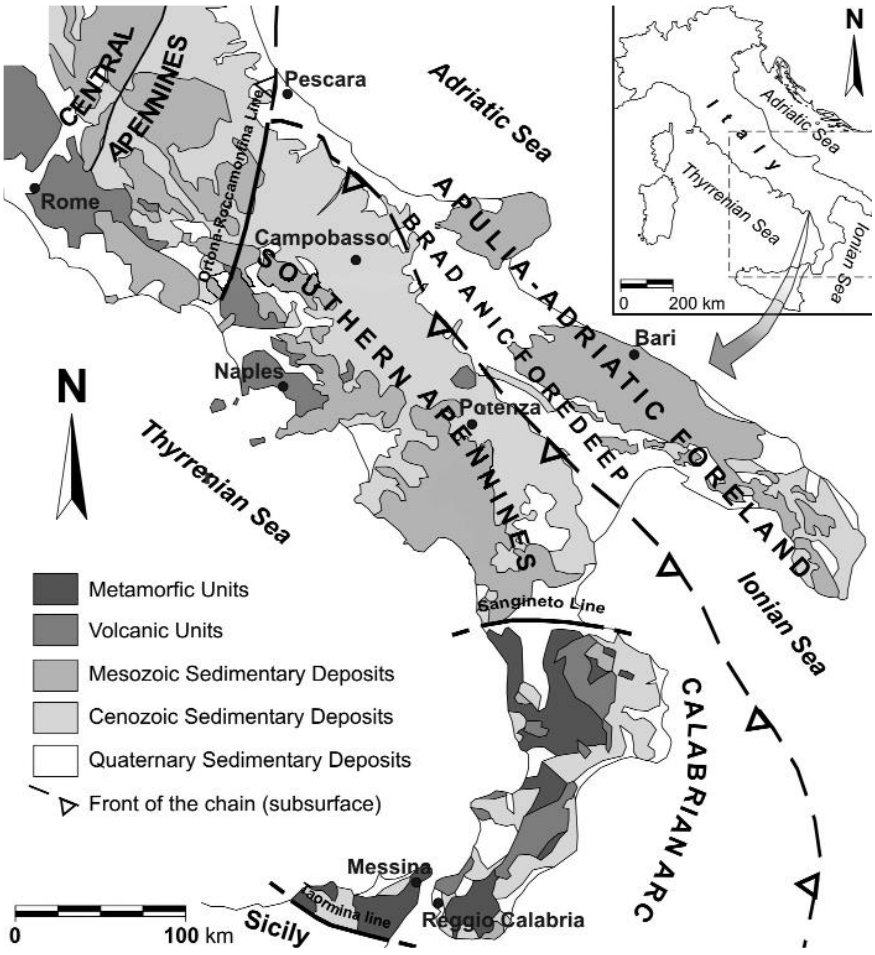

Figure 4 *– Sketch geological map of the central-southern Italy (from Bonardi et al., 2009).*

Its evolution has been directly determined by the relative motions of the European and African plates and involves sedimentary successions of different paleogeographic domains (Dewey et al., 1989). Therefore, the southern Apennine consists of a northeast verging thrust and fold belt interposed between the back-arc Tyrrhenian basin, next to the westward subducting Ionian-Adriatic plate and the undeformed Apulian-Adriatic foreland to the East (Boccaletti et al., 1971; Malinverno and Ryan, 1986; Beccaluva et al., 1989; Mantovani et al., 1993; Doglioni et al., 1999). Its current structural settings are the result of both mainly compressive tectonic events, related to the subduction followed by the rollback of the Adria plate, and the extensional tectonics related to the opening, since the late Miocene, of the Tyrrhenian Sea (Malinverno and Ryan, 1986; Patacca and Scandone, 1989; Doglioni, 1991). Constraints related to GPS measurements (Hollenstein et al., 2003; Rosenbaum and Lister, 2004; Serpelloni et al., 2005, 2006), earthquake depths (Meletti et al., 2000; Chiarabba et al., 2005), focal mechanisms (Pondrelli et al., 2002, 2006) and stress orientations (Hippolyte et al., 1994; Montone et al., 2004) suggest the cessation of subduction/rollback of the Adriatic microplate. It also suggests a development of extensional forces in the southern Apennines after the mid-Pleistocene (Ökeler et al., 2009).

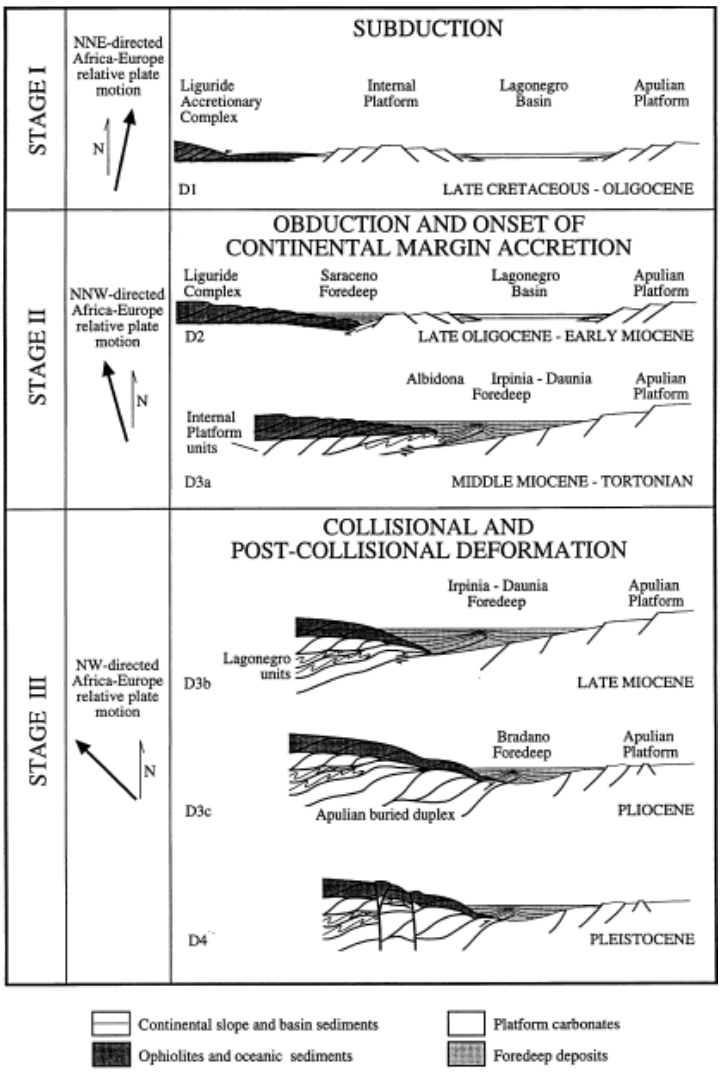

Figure 5 *– Main stages in tectonic evolution of the southern Apennines and related deformation phases (D1-D4). Relative plate motion from Dewey et al., (1989), Mazzoli and Helman (1994) and Cello and Mazzoli (1999).*

Except for the remnants of an internal Cretaceous-Paleogene accretionary complex (Liguride and Sicilide units, Ogniben, 1969; Bonardi et al., 1988; Mauro and Schiattarella, 1988; Patacca and Scandone, 2007), the southern Apennine allochthony wedge is composed by Trias-Middle Miocene sediments. They derived

from the deformations of two different paleogeographic domains: the *Apenninic peritidal carbonate platform (*also known as Campania-Lucania platform or western platform), and the *Lagonegro basin (Pescatore et al., 1999).* The development of the southern Apennines can be divided into three main evolutionary stages. They base on the structural signature of the different rock units, on the available biostratigraphic and radiometric data (Monaco and Tortorici, 1995) and on plate tectonic reconstruction (Dewey et al., 1989; Mazzoli and Helman, 1994; Cello et al., 1995; Cello and Mazzoli, 1999; Mazzoli et al., 2001) (Fig.5):

- An oceanic subduction stage (*Stage 1*);
- An obduction stage followed by the onset of accretion of the Apulian continental margin (Stage 2);
- A collisional to post-collisional stage (Stage 3).

The deepest tectono-stratigraphic units of the southern Apennines Thrust Systems are Mesozoic-Tertiary shallow-water carbonates stratigraphically overlain by upper Messinian and Pliocene terrigenous marine deposits (Fig.6a). These rocks units constitute the buried Apulian belt (Cello et al., 1989), which is tectonically overlapped, from bottom to top, by: (i) thrust sheets derived from a Triassic to Miocene sedimentary succession deposited in a relatively deep basinal domains located between the Internal and Apulian platforms (the Lagonegro-Molise basin; e.g. Mostardini and Morlini, 1986 and reference therein) (Fig.6b); (ii) thrust sheets derived from the deformation of platform carbonates and associated marginal areas bordering the southern margins of Neothetys (the Internal platform; e.g. Scandone, 1982); (iii) thrust sheets belonging to two groups of nappes derived from different paleotectonic domains which are considered to be internal (i.e. located to the west) with respect to Internal Platform.

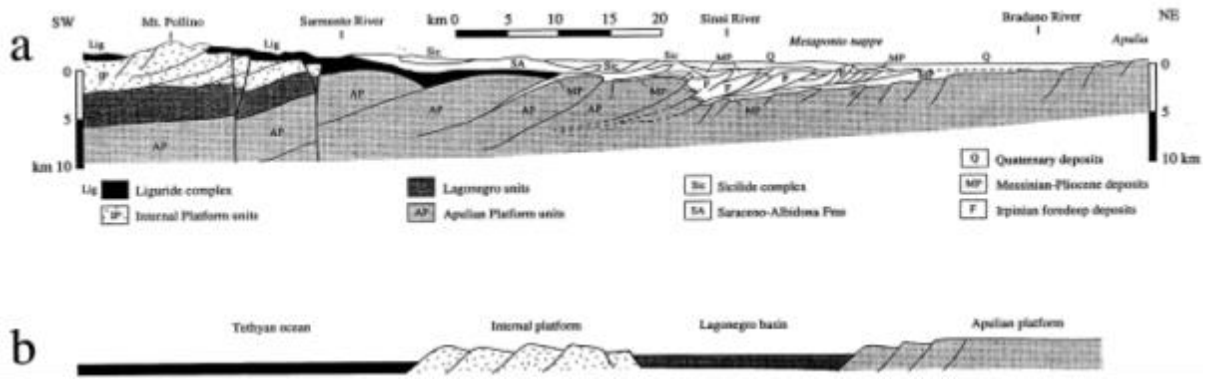

Figure 6 *– a) Simplified geological profile across the Calabr+ia-Lucania borderland area of the southern Apennines (modified after Cello et al., 1990); b) schematic paleogeographic setting of the Apulian continental margin in Cretaceous times (not in scale).*

The latter thrust sheets crop out extensively in the Calabria-Lucania borderland and in Cilento, where they represent the highest structural units in the tectonic pile of the southern Apennines Thrust Systems (Ogniben, 1969). They consist of:

1. *Liguride complex* – Upper Jurassic to Upper Oligocene sedimentary successions incorporating ophiolitic suites (Bonardi et al., 1988) and including both blueschist-facies rocks (Metamorphosed Liguride Terrain) and non-metamorphic to very low grade lithologies (unmetamorphosed Liguride Terrain).
2. *Calabrian complex* – tectonic element made up of crystalline rocks traditionally considered to be of Austroalpine (i.e. south Tethyan) affinity and to represent part of an originally continuous Early Tertiary chain extending from the western Alps over Alpine Corsica to southern Italy, Sicily and North Africa (e.g. Haccard et al., 1972; Alvarez, 1976; Amodio-Morelli et al., 1976). However, in more recent studies the Calabrian nappes have been re-interpreted as representing remnants of the European-Iberian plates (e.g. Dietrich,1988; Cello et al., 1995 and reference therein).
3. *Sicilide complex* – Upper Cretaceous to lower Tertiary sedimentary succession composed mainly of varicoloured clays.

The paleogeographic attribution of these units is still uncertain, as the sedimentary succession of the Sicilide complex has been considered either of internal origin (i.e., deposited west of the Internal Platform) (e.g. Cinque et al., 1993; Monaco and Tortorici, 1995) or as part of the higher portion of the Lagonegro basin succession, detached from its Mesozoic substratum during the early phases of contractions and basin inversion (e.g. Mostardini and Merlini, 1986, and reference therein; Casero et al., 1988). A further hypothesis, involving an early activation of major detachment horizons cutting across the original basin architecture, possibly preceded by minor normal fault reactivation (e.g. Butler, 1989), could also explain the occurrence of truncated folds and faults within the detached tectonic units cropping out in southern Lucania (e.g. Torrente, 1990; Mazzoli, 1992, 1993a).

2.2 Geodynamics and deformation pattern of southern Apennines

A system of left strike-slip faults, locally accompanied by tensional and compressional features, dissected the Lucania Apennines since the middle Pleistocene (e.g. Patacca et al., 1990; Turco et al., 1990; Catalano et al., 1993,2004; Cinque et al., 1993; Monaco 1993). In the northern sector of the southern Apennines, from the Irpinia to the Matese zones, a series of tectonic troughs, associated with NE-SW extension, were generated.

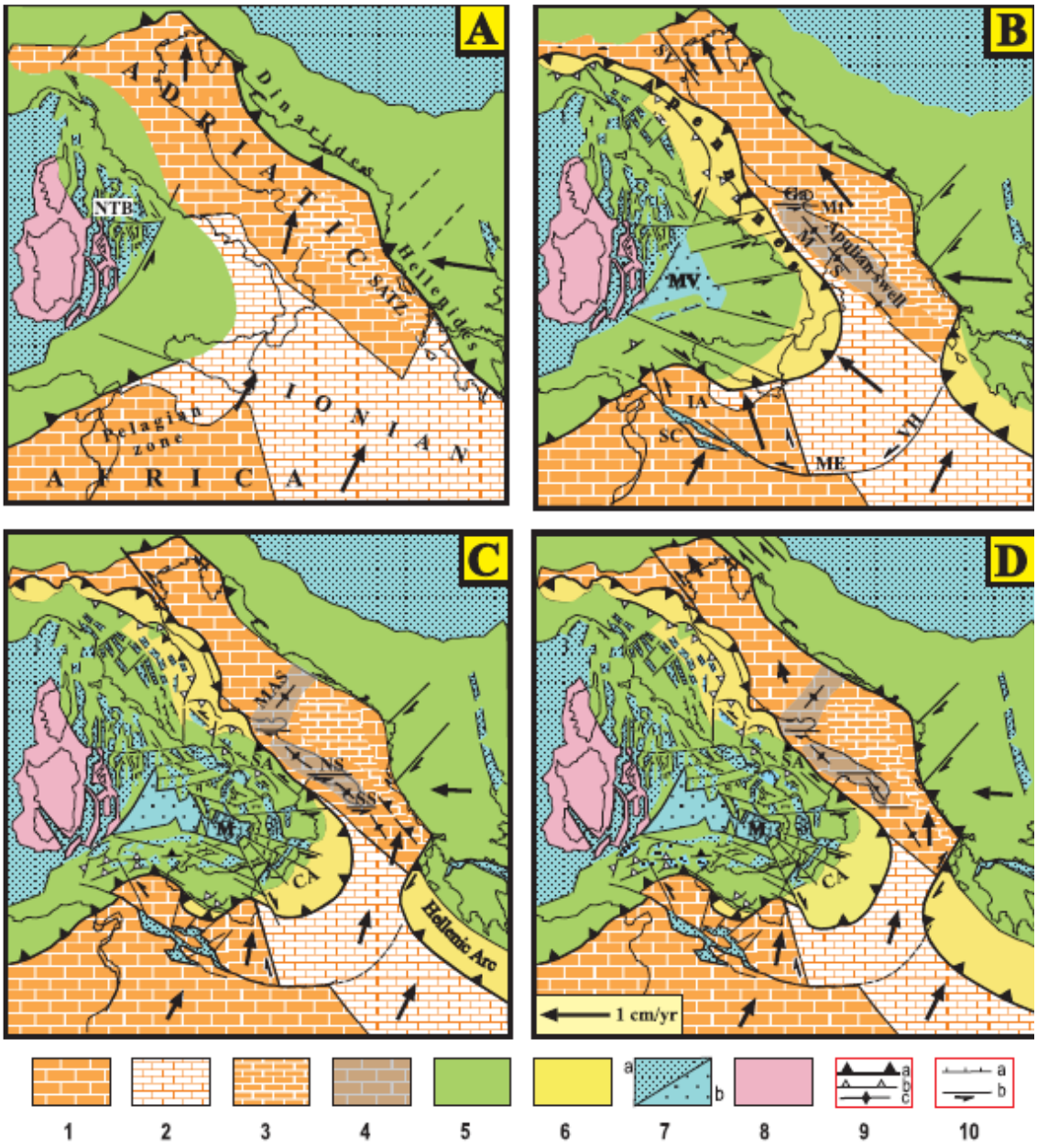

Figure 7 - *Plio-Quaternary evolution of the central Mediterranean region (from Viti et al., 2006). 1) Africa and Adriatic continental domains; 2) Ionian oceanic domain; 3) Thinned continental sector of the southern Adriatic plate; 4) Mid-Adriatic and Apulian swells; 5) Pre-Late Miocene orogenic belts; 6) Plio- Quaternary accretionary belts; 7) Zones affected by moderate (a) and intense (b) crustal thinning; 8) Corsica-Sardinia microplate; 9) Compressional features: outer front of the orogenic belts (a), internal thrusts (b), anticline axes (c); 10) Main fault systems: normal (a), transcurrent (b). Plate motions (arrows) are based on Dercourt et al., (1986) and Mantovani (2005). Motion rates are only indicative. Present coastlines and the paleo position of Africa (thick line) are reported for reference in each evolutionary phase. A) Upper Miocene. NTB = North Tyrrhenian Basin, SATZ = southern Adriatic Thinned Zone. B) Pliocene. Ga, M, S = Gargano, Murge and Salento sectors of the Apulian swell, IA = Iblean-Adventure block, ME, SC, VH= Medina, Sicily Channel and Victor Hensen tectonic belt, Mt = Mattinata fault, MV = Magnaghi-Vavilov basin, SV = Schio-Vicenza fault system. C) Lower Pleistocene. CA = Calabrian Arc, M = Marsili basin, MAS = Middle Adriatic swell, NS = north Salento fault zone, SA = southern Apennines, SS = south Salento fault zone. D) Upper Pleistocene.*

Contemporaneously, the axial and outer sectors of the belt underwent a fast uplift along with the Calabrian Arc (e.g. Cinque et al., 1993; Westaway, 1993; Bordoni and Valensise, 1998; Schiattarella et al., 2003), whereas subsidence occurred in some zone of the Tyrrhenian margin of the belt (e.g. Romano, 1992). Some authors (e.g. Westaway, 1993; Cinque et al., 1993; Mazzoli et al., 2006) suggested that the Quaternary accelerations of the uplift in the southern Apennines and Calabrian Arc can be interpreted as an effect of the elastic rebound of the crust in response to the detachment of the subducted lithosphere beneath that zone. Other authors (e.g. Patacca and Scandone, 1989; Dewey et al., 1989; Turco and Zuppetta, 1998; Mattei et al., 2004) explained the evolutions of the Tyrrhenian-southern Apennines system as an effect of the gravitational sinking (*slab-pull*) of the Ionian subducted lithosphere. Therefore, in the framework of this interpretation, the system of left faults in the Lucania Apennines is interpreted as the decoupling shear zone between the migrating Calabrian-Tyrrhenian wedge (driven by the retreating Ionian slab) and the Apenninic belt (Fig.7).

However, this interpretation is not consistent with a large amount of geological and geophysical evidence (e.g. Finetti and Del Ben, 1986; Finetti et al., 2005a, and reference therein). This evidence strongly suggests that the extruding wedge does not include the southern Apennines since it is only constituted by the Calabrian block, bounded by the NE-SW Sangineto (e.g. Patacca and Scandone, 2004) or by the E-W Palinuro decoupling strike-slip fault systems (e.g. Finetti and Del Ben, 1986; Del Ben, 1993; Catalano et al., 2004). The last hypothesis effectively explains the Quaternary deformation pattern in the surrounding regions, with particular regard to the compressional (External Calabrian Arc) and tensional (Marsili basin) (Fig.7) features respectively generated in the outer and internal boundaries of the escaping Calabrian wedge (e.g. Finetti and Del Ben, 1986; Mantovani et al., 1997, 2001, 2006a; Catalano et al., 2004; Mantovani, 2005). Furthermore, the development of the NW-SE left-lateral fault system in the Lucania Apennines postdates the outward migration of the Calabrian wedge concerning the southern Apennines which started from Pleistocene (e.g. Finetti and Del Ben, 1986; Patacca et al., 1990; Catalano et al., 1993, 2004; Van Dijk and Scheepers, 1995). Anderson and Jackson (1987) and Westaway (1992) hypothesized that the Quaternary extensional deformation in the southern Apennines, such as in the whole belt, is the effect of divergence between Tyrrhenian and the Adriatic plate (Fig.7). However, this hypothesis does not explain other major tectonic events, such as the Quaternary fast uplift of the chain, the formation of the Matese-Benevento and Campania-Lucania arcs in the late Pliocene-lower Pleistocene and the development of a left-lateral strike-slip fault system in the Lucania Apennines since the middle Pleistocene.

Mantovani (2005) and Mantovani et al. (1997, 2002, 2006a) attempted to provide a coherent explanation of the space-time distribution of all major tectonic events in the central Mediterranean region. Around the middle Pleistocene, the deformation pattern in the southern Apennines underwent a considerable change. The southernmost sector, the Lucania Apennines, was dissected by a system of NW-SE left-lateral strike-slip faults, such as the *Satanasso, Montesano, Valsinni, Scuorciabuoi* and *Stigliano* faults, accompanied by compressional and tensional features at restraining and releasing stepovers respectively (e.g. Turco et al., 1990; Catalano et al., 1993, 2004; Monaco, 1993; Casciello et al., 2002b).

Locally, as for instance in Mount Vulture area, NE-SW dextral strike-slip lineaments accompany the main left-lateral features (e.g. Bonini and Sani, 2000). Transtensional and transcurrent deformation continued in the Cilento-Pollino, Sele, Agri, Diano and Tanagro troughs (e.g. Caiazzo et al., 1992; Cello et al., 2003; Maschio et al., 2005). Transpressional deformation occurred in the Santarcangelo basin (e.g. Turco et al., 1990; Monaco et al., 1998; Catalano et al., 2004).

CHAPTER 3

MAGMATISM IN THE ITALIAN REGION

3.1 Magmatism in the Italian region

The kinematic reconstruction highlights an apparent link between the propagating tear faults and the spatial and temporal distribution of magmatism (Fig.8). The Italian magmatism is represented by a large spectrum of magmas ranging from subduction-related calc-alkaline and ultra-potassic magmas to intraplate oceanic island basalts (OIB), and Mid Oceanic Ridge Basalts (MORB) (Fig.9) (Peccerillo, 2005; Rosenbaum et al., 2008, and reference therein).

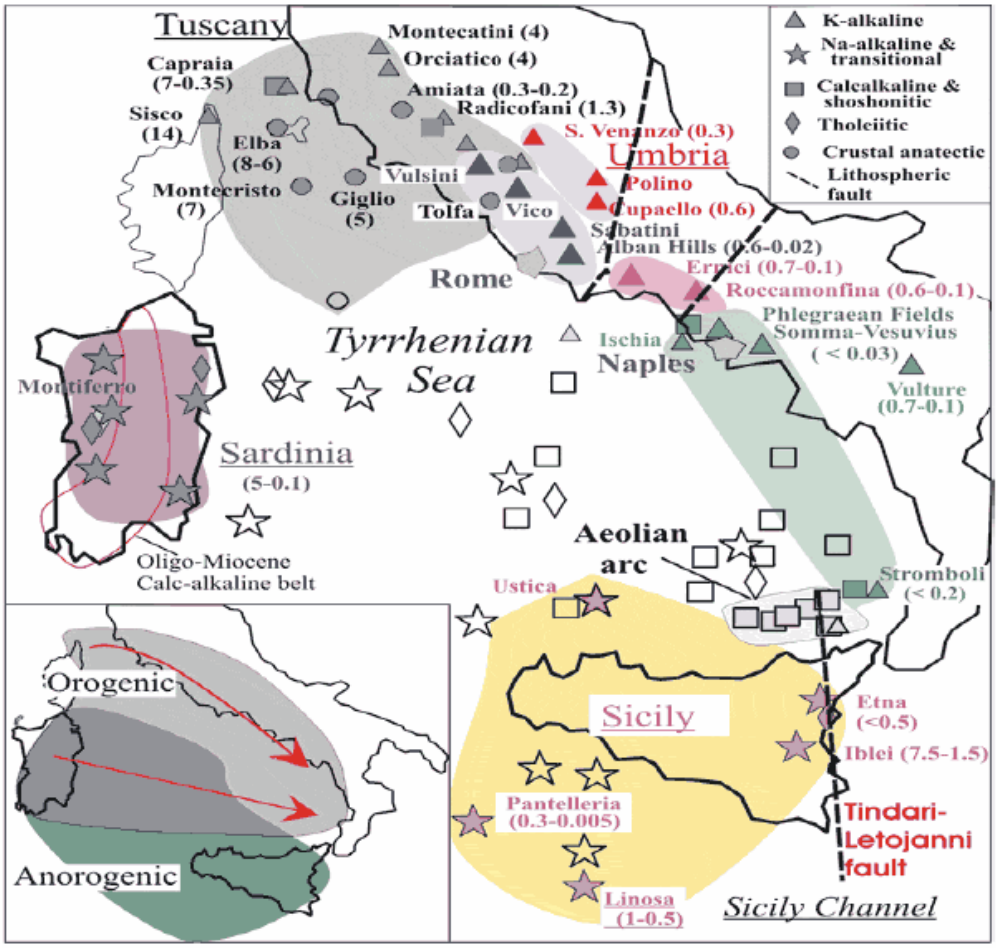

Figure 8 *- Reconstruction of the kinematic evolution of the Tyrrhenian Sea and the Apennine belt. The reconstruction shows the development and propagation of slab tear faults during the segmentation of the retreating subduction zone. The reconstruction images are snapshots at the minimum age of each time interval and show the accumulated magmatic activity during each interval. The classification of magmas based on their geodynamic context is supported by geochemical evidence from Rosenbaum et al., (2008; modified).*

Rosenbaum et al. (2008) proved that the geochemical affinities of the Italian magmas are generally consistent with their geodynamic model, thus further supporting the hypothesis that the Apennine subduction zone was subjected to the segmentation through slab tear faulting. However, this model does not attempt to explain all the complex features of the petrology of the volcanic edifices (e.g. Peccerillo, 2001, 2005; Gasperini et al., 2002; Panza et al., 2007).

In the Tyrrhenian sea the early stage of magmatic activity, which followed abundant calc-alkaline magmatism in Sardinia, was associated with 9-6 Ma intrusive and extrusive magmatism in Capraia (3 – see the *Fig.9 a, b, c, d and e* for the number), Elba (12,13), Montecristo (16) and Vercelli seamount (Fig.9a and Fig.9b). Magmatism appears immediately above the Miocene subducting slab and is attributed to the subduction-related magmatic arc. This magmatic arc was migrated eastward (Civetta et al., 1978) from Capraia, Vercelli Seamount, Montecristo, and western Elba to eastern Elba and Giglio islands (17 – Fig.9c). Direct evidence for subductions-related magmas is less clear in southern Tyrrhenian but there have been suggestions for the existence of a submerged Pliocene subduction-related volcanic arc (Sartori, 1989; Sartori et al., 2004). The location of this arc exactly corresponds to the geometry of the subduction zone at 6-4 Ma (Fig.9c).

Moreover, further magmatism was generated by decompression melting of the asthenospheric mantle in extensional regions and gaps in the slab corresponding to tear faults simultaneously with the production of Pliocene subduction-related magmas. One of these tear faults propagated from the northern tip of Corsica to southern Tuscany, producing mantle-derived shoshonites in Capraia at ~ 4.8 Ma. Further east, the crustal uplift in southern Tuscany and the production of anatectic felsic magmas (San Vincenzo (5), Castel di Pietra and Gevorrano (8)) along the same fault (Fig.9c) are also interpreted to result from the combination of slab tearing and arc magmatism. Contemporaneous volcanism located along tear faults also occurred further south in Anchise Seamount (42) and Ponza Island (27).

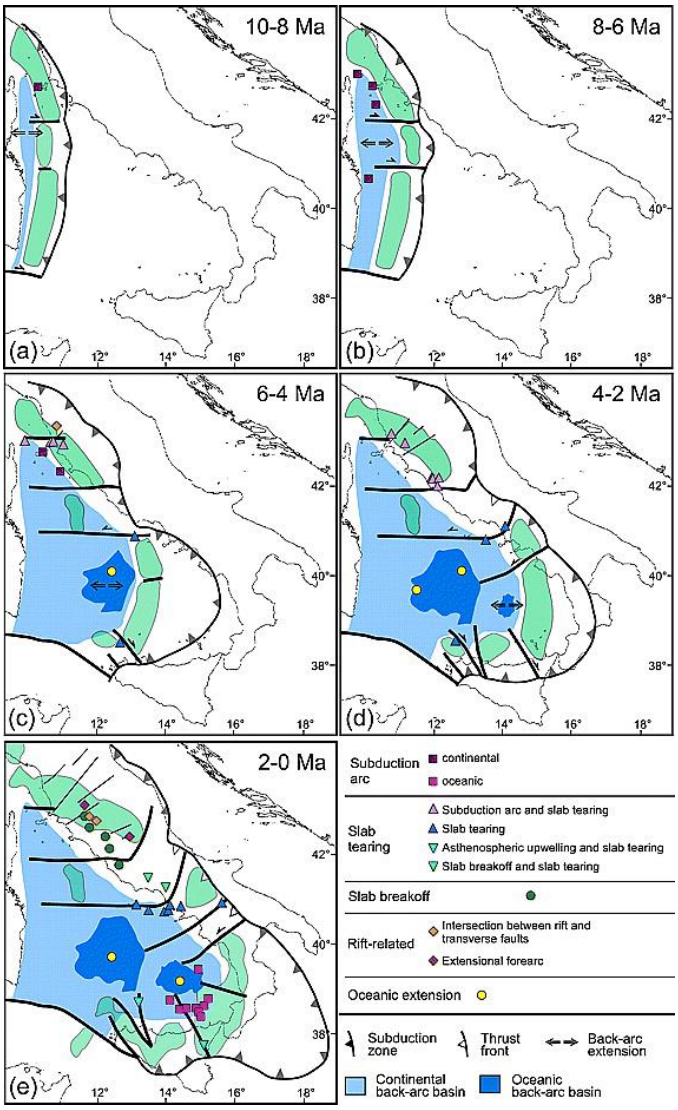

Figure 9 *- Spatial distribution and petrochemical affinity of young (<10 Ma) magmatic centres in the Italian peninsula, Sicily and the Tyrrhenian Sea (after Peccerillo, 2005). OIB type magmatic centres in the African foreland (e.g., Hyblean Mountains, Pantelerria, Linosa) and in Sardinia are not included. (From Rosenbaum et al., 2008; modified).*

The latter was subjected to magmatism from 4.2 to 1 Ma (Cadoux et al., 2005), and is considered as the northern end of the southern Tyrrhenian Pliocene arc (Sartori, 1989), which was transected by the tear fault of the 41°N parallel line.

The distribution of some of the younger (4-2 Ma) magmatic activity was also focused along the deeper tear faults (Fig.9d). This includes a cluster of subduction/tear-related magmatic centers (Tolfa (19), Manziana (20), and Cerite (21)). In the south, the occurrence of magmatism in Volturno (26) (> 2 Ma) and Ponza (27) (4.2 to 1 Ma) also coincide with slab tearing. Subsequently, during the last 2 Ma (Fig.9e), the central Apennines were subjected to a widespread tear-related magmatic activity and magmatism induced by *breakoff* of the lithospheric slab (De Astis et al., 2006; Panza et al., 2007). This magmatic phase represents the

geodynamic expression for the formation of the central Apennine asthenospheric window following slab segmentation, and the local destruction of the subduction system (Rosenbaum et al., 2008). Further south, arc magmatism in the Aeolian Islands was generated by the subduction of the narrow Ionian slab.

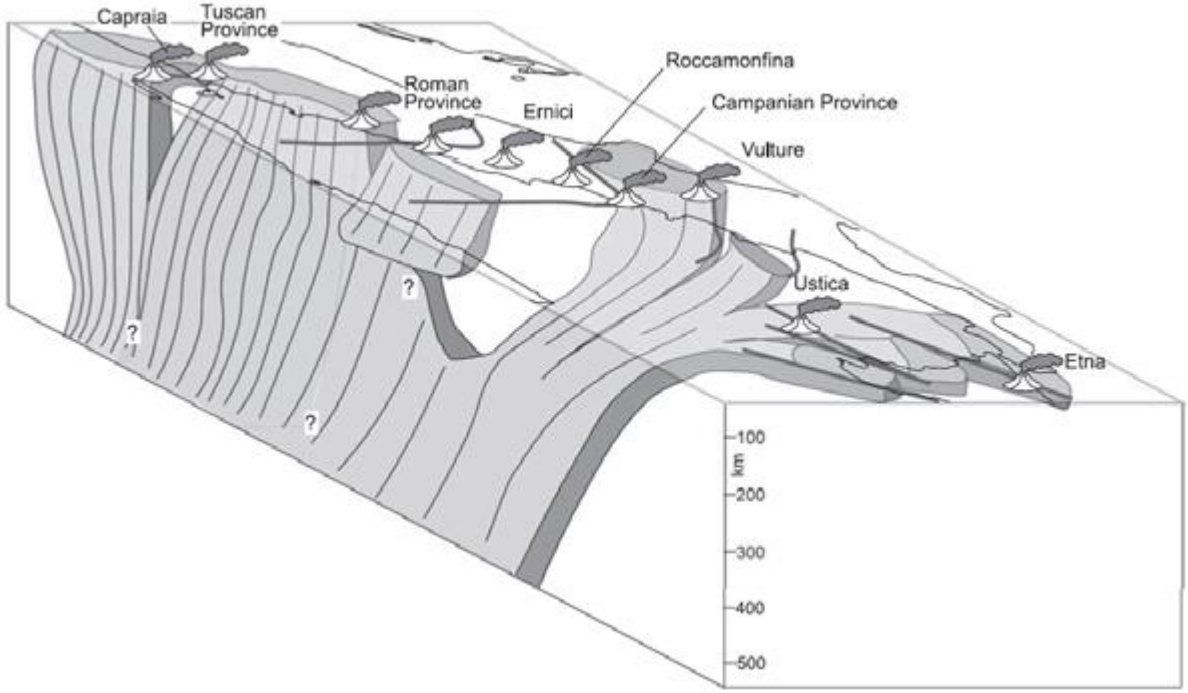

Figure 10 *- Simplified 3-D sketch of the subducting lithosphere beneath Italy showing the approximate spatial distribution of tear faults and the geometry of the central Apennine slab window. Selected tear related and slab break off-related magmatic centers are also shown (from Rosenbaum et al., 2008).*

Mount Etna and Mount Vulture represent two most striking examples of asthenospheric upwelling along with slab tear faults (Gvirtzman and Nur, 1999; Doglioni et al., 2001; Trua et al., 2003; De Astis et al., 2006), (Fig.10). These volcanoes are located on the margin of the Apulian foreland and are therefore much less affected by subduction processes. Mt. Etna is characterized by a typical Ocean Island Basalt (OIB) composition with some arc signatures in the younger products (Schiano et al., 2001) whereas the Mt. Vulture magmatic source is similar to the Campanian-Pontine volcanoes (Vesuvius, Phlegraen Fields), but its position over the edge of the Adriatic continental lithosphere resulted in a higher level of intraplate (OIB type) mantle influence (De Astis et al., 2006; among many authors). The mineralogical variations and chemical compositions of Plio-Quaternary Italian volcanic rocks cover one of the greatest petrological ranges observed anywhere on Earth (e.g. Cundari, 1979; Peccerillo and Manetti, 1985; Civetta et al., 1989; Conticelli and Peccerillo, 1992; Serri et al., 1993; Cundari, 1994;

Stoppa and Wooley, 1997; Wilson and Bianchini, 1999; Lustrino et al., 2000; Conticelli et al., 2002; De Astis et al., 2003; Peccerillo, 2005; Beccaluva et al., 2004).

The researchers who sustain the subductions-related models assume that many of these rocks are similar to those found in active subduction zones, and commonly cite those rocks found in the Aeolian Islands. However, when major and trace elements are plotted in various geochemical diagrams the findings are ambiguous and it remains unclear as to whether the rocks are subduction-related or whether they are the products of intra-plate magmatism (e.g. Lavecchia and Stoppa, 1996). The potassic and SiO_2-undersaturated nature of these rocks is of particular interest since those features are difficult to assign to a particular tectonic setting using the standard major and trace element geochemical diagrams. Transitional basalts and basaltic calc-alkaline rocks mainly occur in the Tyrrhenian region and in the Aeolian insular arc. However, rocks belonging to the so-called *Mediterranean Series* of Washington (1906) dominate in peninsular Italy (Fig.8). The Mediterranean Series is composed of leucite-bearing, SiO_2-undersatured rocks (the HK-series, Appleton, 1972) such as leucite tephrites, leucite phonolitic tephrites, leucite tephritic phonolites and leucites, which are atypical of subduction-related environments. Italian leucites, commonly associated with leucite-free rocks (the K-series) are located in the Roman-Campanian Region at Vulsini, Cimini, Sabatini, Albani, Ernici, Roccamonfina, Vesuvius, at Vulture in Basilicata and Vulcanello in the Aeolian Islands. These series contrast with most subduction-related rocks which are generally SiO_2-saturated. Leucite-bearing rocks can be found, but in very isolated cases, in subduction related settings although shoshonites and calc-alkaline rocks (andesite-dacite) can also be found in continental rift environments (Gupta and Fyfe, 2003).

The isolated occurrences of shoshonitic or leucitites rocks do not automatically imply consuming plate margins. Na-alkaline rocks mainly occur in Sardinia, Sicily and the Sicily Channel at the inner and southern side of the Tyrrhenian rift zone, whereas carbonatites and kamafugites (e.g. K-melilitites) are present along the intra-Apennine graben system, at the outer side of the Tyrrhenian zone. They occur in Umbria (San Venanzo, Polino, Collefabbri), in Latium (Cupaello), in Abruzzo (Oricola, Grotta del Corvo) and Basilicata (Mount Vulture) (Stoppa, 1988; Cundari and Ferguson, 1991; Stoppa and Lavecchia, 1992; Stoppa and Lupini, 1993; Stoppa and Cundari, 1995; Stoppa, 1996; Stoppa and Woolley, 1997; Stoppa and Cundari, 1998; Stoppa and Principe, 1998; Comodi et al., 1999; Bailey and Collier, 2000; Jones et al., 2000; Rosatelli et al., 2000; Barbieri et al., 2002; Panina et al., 2003; Stoppa, 2003; Capitanio et al., 2004; Lavecchia and Creati, 2006; De Astis et al., 2006; D'Orazio et al., 2007).

CHAPTER 4

MOUNT VULTURE VOLCANIC COMPLEX: GEOLOGICAL AND PETROGRAPHYCAL FEATURES

4.1 Origin, tectonic evolution and volcanic history of Mount Vulture volcano

Mount Vulture is located at the easternmost border of the Apennine compressive front (Fig.11), on the leading edge of the southern Apennines accretionary prism, along the southern border of the ENE-trending Ofanto graben. It represents the easternmost occurrence of the Quaternary Italian volcanism and is the only volcano of peninsular central-southern Italy.

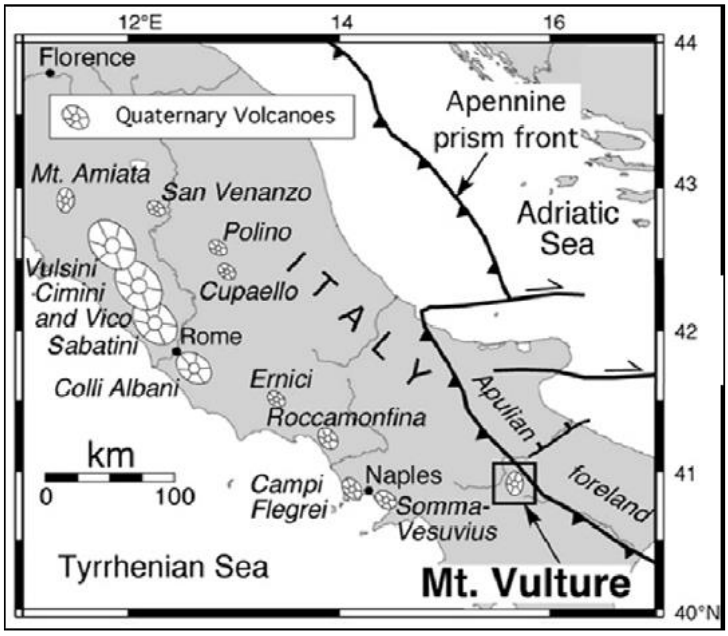

Figure 11 *- Sketch map of central-southern Italy with the main occurrences of the Quaternary volcanism and the front of the Apennine prism (Scrocca, 2006); (by D'Orazio et al., 2007).*

The genesis and evolution of Mt. Vulture volcano took place during the recent deformation of the frontal part of the south Apennines chain. More recent tectonic shortening occurred at the belt front, leading the deformation of both Plio-Pleistocene sediments (Pieri et al., 1997b) and Quaternary volcanic (Beneduce and Schiattarella, 1997). Moreover, a widely documented extension is still active along the Apennines axis (Ortolani et al., 1992; Amato and Selvaggi, 1993). The active belt is also affected by Plio-Quaternary strike-slip faults mainly oriented according to N120±10° and N50-60° trends (Schiattarella, 1996, 1998, and reference therein) and locally by low-angle normal faults (Ferranti et al., 1996, and reference therein). The continental crust has a maximum thickness of about 30 km beneath the axis of the Southern Apennines chain (Locardi and Nicolich, 1988), decreasing to 10-15 km in Tyrrhenian area whereas reaches to 30-35 km in the foreland (Ventura et al., 2007) and beneath the Mt. Vulture complex (Corrado and Rapolla,

1981; Corrado et al., 2005). Moving from the Tyrrhenian Sea toward the chain axis, the lithosphere thickness increases from 30 to 90 Km and reaches up to 100 Km in the Mount Vulture area and Adriatic foreland (Calcagnile and Panza, 1981).

The volcanic building of Mt. Vulture was formed at the intersection between the NW-SE (Apenninic) and NE-SW (Ofanto-Sele) fault system (Ciaranfi et al., 1983), changing from transpressional to transtentional conditions during the Middle Pleistocene (Beneduce and Schiattarella, 1997), on the eastern side of the Apennine chain, where the Apennine thrust front overlaps the Apulia carbonate foreland (La Volpe et al., 1984; Schaittarella et al., 2003). The faults and fracture populations system, occurring in both volcanic units and sedimentary bedrocks, highlight the interplay between volcanogenic deformation and tectonic evolution. The orientations of faults and fracture sets mirror the arrangement of the morpho-lineaments and changes concerning the centre of the volcano. Three main morpho-tectonic stages, characterized by different fault kinematics, affected the Quaternary volcanic deposits and the adjoining sedimentary successions. An important tectonic deformation occurred between the early and middle Pleistocene. The presence in the volcanic units of N120°±10° trending strike-slip faults, which represent a regional feature of the southern Apennines, and NE-SW directed extensional faults suggest a tectonic control over the deformation of the volcanic complex (Schiattarella et al., 2005). In this setting, a set of N40-50° trending deep faults was generated. The transfer structure, known as the *Vulture line*, crosses the entire chain-foreland system (Schiattarella et al., 2005). It was active both during the Upper Pliocene – Lower Pleistocene contractional regime and the Middle-Upper Pleistocene extensional stages (Fig. 12). The

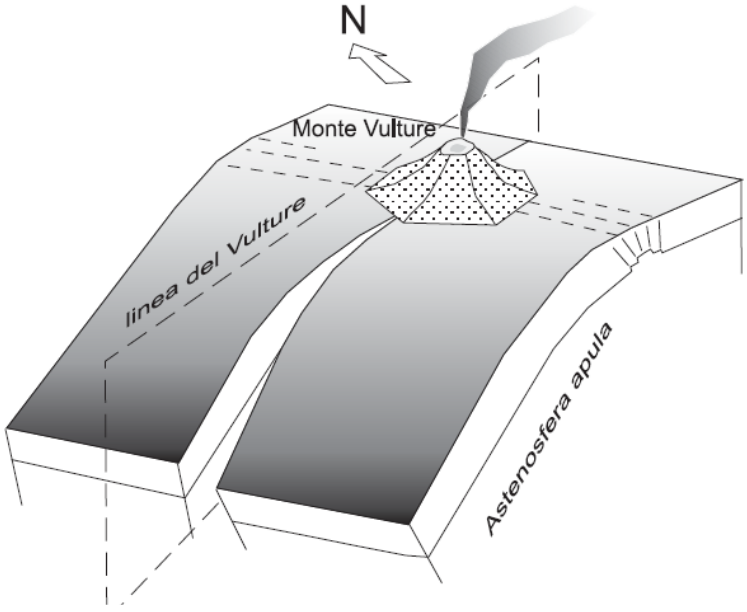

Figure 12 – *Block-diagram showing the possible lithospheric setting of the areas adjoining the Vulture Line (from Schiattarella et al., 2005, modified).*

Vulture line is the expression of system faults cutting the entire chain-foreland system (Schiattarella et al., 2005).

This discontinuity could be considered as the surface expression of sub-vertical lithospheric tear faults in the Adriatic slab below the southern Apennines originated as a consequence of variation in the velocity of subduction rollback along the length of the subduction system (Govers and Wortle, 2005; D'Orazio et al., 2007). Rosenbaum et al., (2008), based on the deep structure revealed by seismic tomography, proved the presence of a slab tear faults in the southern Apennines, which acted at depth of 100-340 km with NE-SW surface orientation.

The lithospheric tear faults are linear seismic velocity discontinuity that separates a distinct slab segment with positive P wave seismic anomalies. Some authors suggest that Mt. Vulture is located on an along-dip vertical slab window (Doglioni et al., 1994; Schiattarella et al., 2005; D'Orazio et al., 2007).

The volcanic activity took place from Middle to Upper Pleistocene, starting about 0.75 Ma and ending about 0.13 Ma, years ago (Brocchini et al., 1994; Buettner et al., 2006). Over the years several studies have tried to explain the origin of the Mt. Vulture magmas. Beccaluva et al. (2002) suggested that the magmas of Mt. Vulture were generated by lithospheric mantle sources and enriched in Na-alkali silicate/carbonatite anorogenic components, that were subsequently affected by orogenic subduction-related K-metasomatism, analogous to that which modified the magma sources of RCP. Moreover, Downes et al. (2002), based on trace elements studies, indicated that the lithosphere beneath Mt. Vulture had already undergone an extensive partial melting before being affected by silicate melt metasomatism, related to subduction. A few years later De Astis et al. (2006) observed that the magmatism was principally derived from an intraplate mantle source (OIB-like), originated from eastern inflow from beneath the Adria-Africa plate after subduction and detachment of the Adria slab (Fig.13), but which was modified by subduction-related processes (Beccaluva et al., 2002; Melluso et al., 1996).

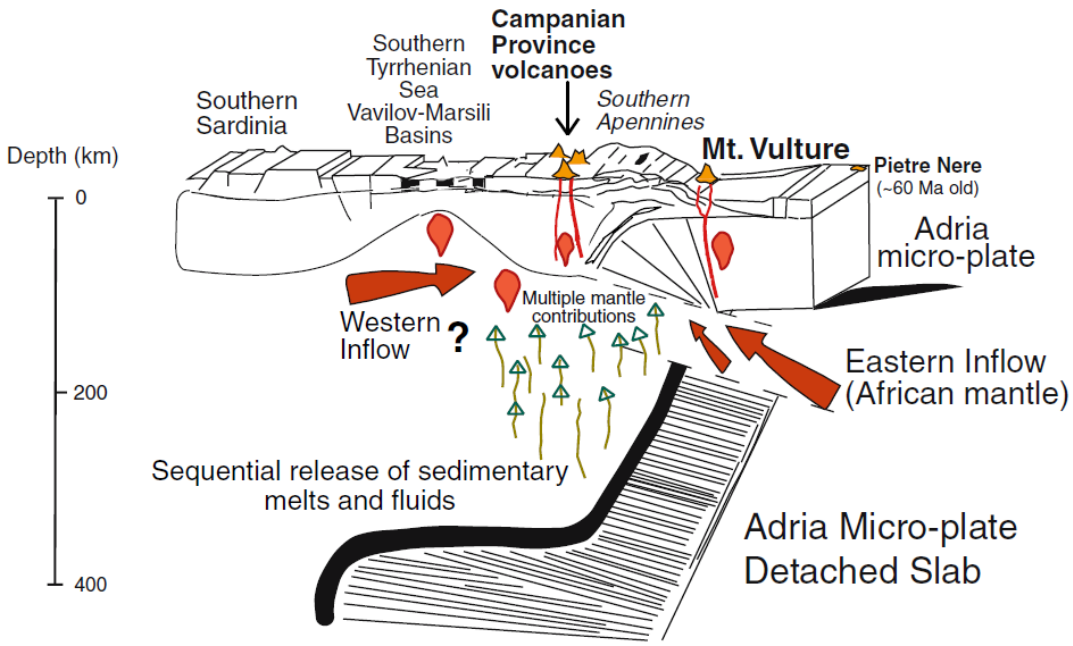

Figure 13 *- Three-dimensional cartoon of the southern Italy and southern Tyrrhenian Sea (from De Astis et al., 2006). Thick arrows indicate the hypothesized directions of mantle inflows from the Adria (Africa) plate and the Tyrrhenian Basins. The southern Italy mantle experienced different types of metasomatism by subduction-related sedimentary melts or supercritical liquids (Mount Vulture) and fluids (Campanian Province volcanoes). The depths of the detached and lying flat slab beneath southern Apennines are derived from tomographic images of P-wave velocity anomalies (in Wortel and Spakman 2000).*

Recently, D'Orazio et al. (2007) showed that the metasomatized mantle wedge below the Campanian/Tyrrhenian region flows eastward and eventually joins the Adriatic mantle beneath Mount Vulture area through its injection into the vertical slab window, creating the hybrid source of the magmas feeding Mt. Vulture volcano (Fig.14).

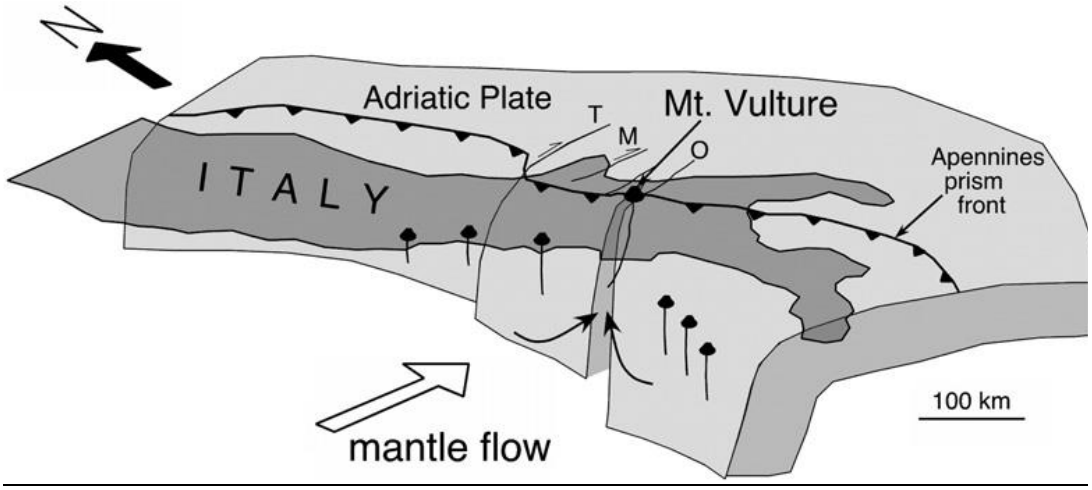

Figure 14 *- Cartoon showing the vertical slab window inferred beneath the Southern Apennines. The relative eastward mantle flow enriched of fluids/melts from the Adria Plate subduction could have converged and flowed into the slab tear sourcing Mount Vulture volcano. T, Tremiti line (E–W); M, Mattinata line (E–W); O, Ofanto graben (ENE–WSW) (from D'Orazio et al., 2007).*

4.2 Geological and petrological framework of the study area

The volcanic building of Mt. Vulture consists of about 700 m thick mainly pyroclastic deposits and subordinate lava flows and domes, owing to both explosive and effusive activities (Brocchini et al., 1994; Serri et al., 2001; Giannandrea et al., 2004). A first stratigraphic study, which allowed to reconstruct the geological history of the Mt. Vulture volcano, was proposed by La Volpe and Principe, (1991). Several years later, Schiattarella et al. (2005) and Giannandrea et al. (2006) revised the whole previous volcanic stratigraphic units proposed by La Volpe and Principe (1991) performing a new study based on UBSU (*Unconformity Boundary Stratigraphic Units;* Salvador, 1987; 1994). The hold six volcanic units were grouped into two main *Supersynthems*: The Monticchio and Mt. Vulture Supersynthems. These two supersynthems are separated by paleosol suturing the pseudo-tectonic structure, called Grigi Valley - Fosso del Corbo Fault, responsible for the down-throwing, of about 100 meters, of the southern half volcanic edifice probably with a south-western sector calderic collapse (Boenzi et al., 1987). The Mt. Vulture Supersynthem is composed of lava and pyroclastic flows ranging in composition from basanites and foidites to phonolites; it is attributed to older volcanic products. The Monticchio Supersynthem represents the result of the most recent explosive eruptions containing ultramafic xenoliths and megacrysts of clinopyroxene, amphibole, olivine, and phlogopite. These last volcanic deposits have a carbonatite-melilitic composition (Stoppa and Principe, 1997), although the primary origin of the carbonatite fraction is still a topic of debate (D'Orazio et al., 2007, 2008; Stoppa et al., 2008).

The volcanic products have a strongly silica undersaturated character with alkaline potassic to ultrapotassic affinities (De Fino et al., 1982, 1986) and range in compositions from foidites (nephelinites, haüynites, leucitites) and melilites (plus basanites and tephrites) to phonolitic tephrites, phonolites and trachytes (Melluso et al., 1996; Beccaluva et al., 2002; De Astis et al., 2006). The large Na and S contents of the Vulture magmas (Marini et al., 1994) result in the widespread presence of sodalite-group phases among the feldspathoids (De Fino et al., 1982; Di Muro et al., 2004). Feldspars and feldspathoids are the main mineralogical phases of pyroclastic deposits and lava flows (De Fino et al., 1986; Beccaluva et al., 2002). The last eruptions produced multiple WNW-ESE aligned monogenic cones (Giannandrea et al., 2004) with a carbonatitic-melilititic composition (Stoppa and Principe, 1997). The fluvio-lacustrine sediments are pre-, syn-, and post-volcanic deposits and crop out in the southern and peripheral sectors of the volcano. These deposits consist of clayey-sandy conglomerate with intercalations

of pyroclastic products (*Units of the Fiumara di Atella and Fosso dello stroppito catchments*; Giannandrea et al., 2006). The bedrock consists mainly of deep-sea sediments belonging to units ranging from the early Triassic to the lower-middle Miocene (Fig. 15) (Boenzi et al., 1987; Principe and Giannandrea, 2002). Radiolarites and limestones of the Apulian platform reach a depth of about 5 km beneath the Meso-Cenozoic substratum units (La Volpe et al., 1984). Martinis and Pieri (1964) reported a Triassic evaporate horizon in the carbonates of the Mesozoic Apulian platform in a well (*Forestay Umbra – 1*) drilled not far from the volcanic structure of Mt. Vulture. Morphological features and structural analysis show that the geomorphology of the Mt. Vulture area is widely due to the interplay between volcanogenic doming and regional tectonics. The fracture-fault system consists of two main orthogonal sets oriented N120°±10° and N40°- 50° (Schiattarella et al., 2005).

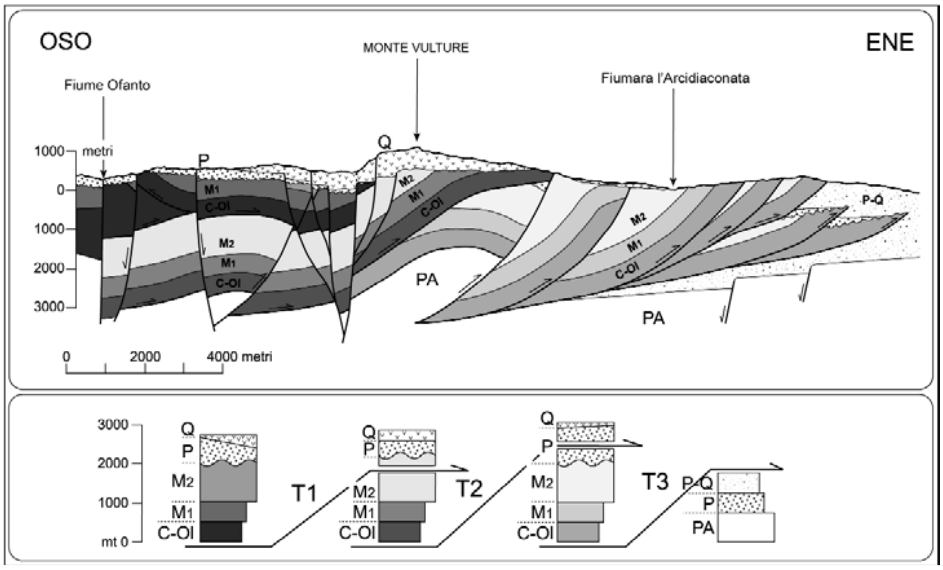

Figure 15 *- Deep geological cross-section through the Vulture area (from Schiattarella et al., 2005). Labels: C-Ol = Cretaceous to Oligocene "Argille Varicolori" – and "Flysch Rosso" – like successions; M1 = Numidian sandstone (lower middle Miocene); M2 = Serra Palazzo Fm (upper Miocene); P = Pliocene clastic deposits; P-Q = Plio-Quaternary foredeep deposits; Q = Quaternary volcanics and epiclastic sediments; T1, T2 and T3 = thrust sequence (different tones of grey show different tectonic units).*

4.2.1 Structural framework

The morpho-structural evolution of the Mt. Vulture volcano is contemporary with the more recent deformation phases of the front of the South-Apennine chain, which was typically contractional in the Pleistocene (Pieri et al., 1997). The control of the tectonic structure of the chain front on the deformation of the volcanic apparatus is highlighted by some faults that follow the orientations of the regional tectonic lines with direction N120° ± 10° (Schiattarella,

1998). Some researchers studied the interactions between these deformations through the analysis of tectonic lineaments families, present both in volcanic deposits and in quaternary sediments (Beneduce and Giano, 1996; Beneduce and Schiattarella, 1997; Schiattarella, 1998). Fractures consist of high-angle systems, grouped in two main orthogonal families, (Fig.16).

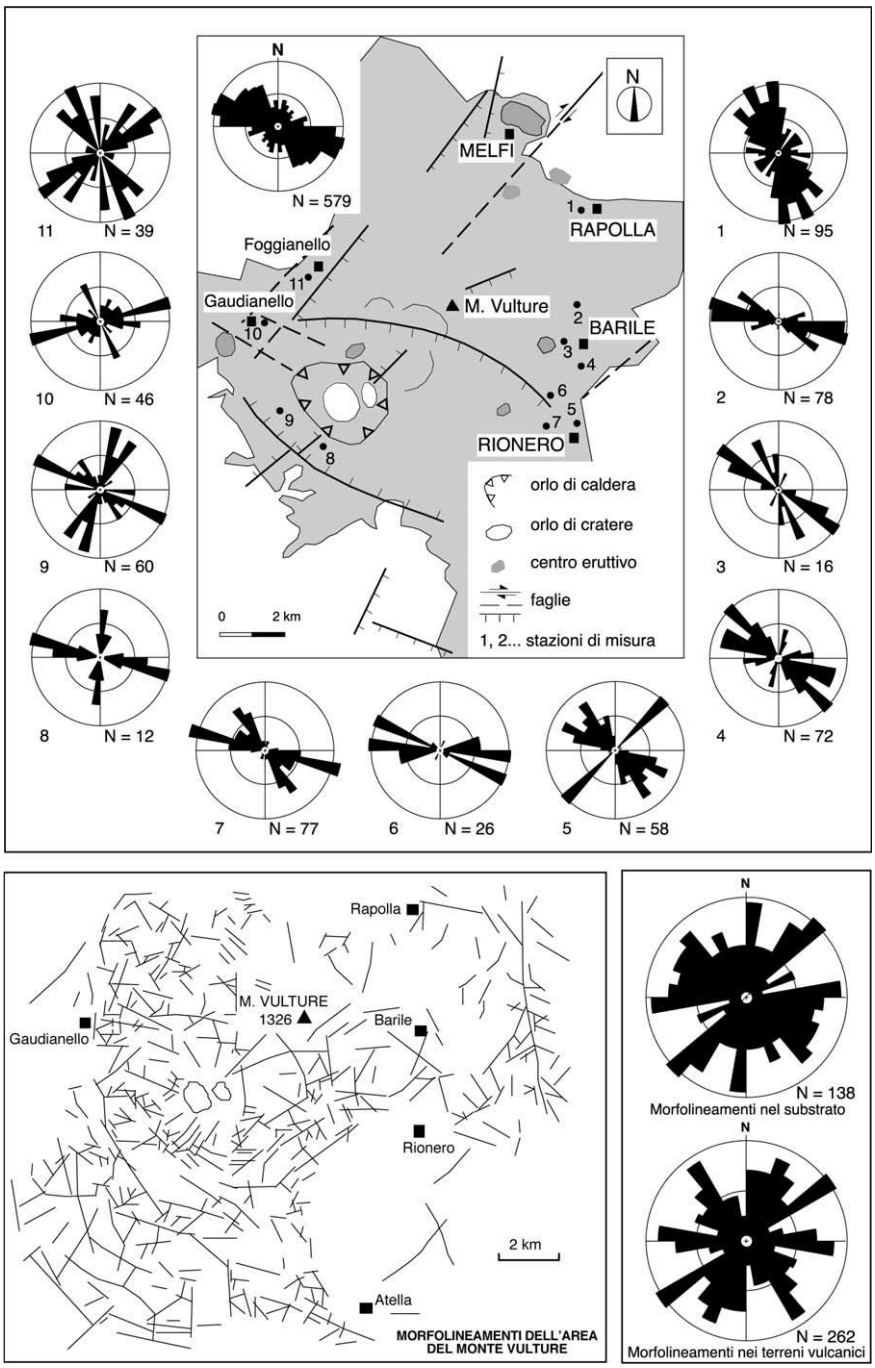

Figure 16 *– Azimuthal diagrams of high angle or subvertical fracture systems in the Vulture volcanites (from Beneduce and Schaittarella, 1997; modified); in the box, diagram of total fractures. Morpholineaments of the Mount Vulture area and adjacent areas (from Beneduce and Giano, 1996; modified); on the side, azimuthal diagrams relating to the morpholineaments of the volcanic area and those of the pre-volcanic substrate.*

The orientations of these pairs varies with the position concerning the centre of the volcanic building and shows a typically concentric-radial pattern (Beneduce and Giano, 1996). This pattern results from the volcanic activity, i.e. pulsations of magma chamber and pre-eruptive deformation of the soil, eruptions, and calderic collapse. The presence of reverse or transpressive fault is relevant in several places. A paleo-soil fossilized a flower structure (Fig.17), generated by left-transcurrency along surfaces with direction N120°. The synthematic unity of the Valle dei Grigi-Fosso del Corbo (484 ± 8 ka; Brocchini et al., 1994) lies on the paleo-soil.

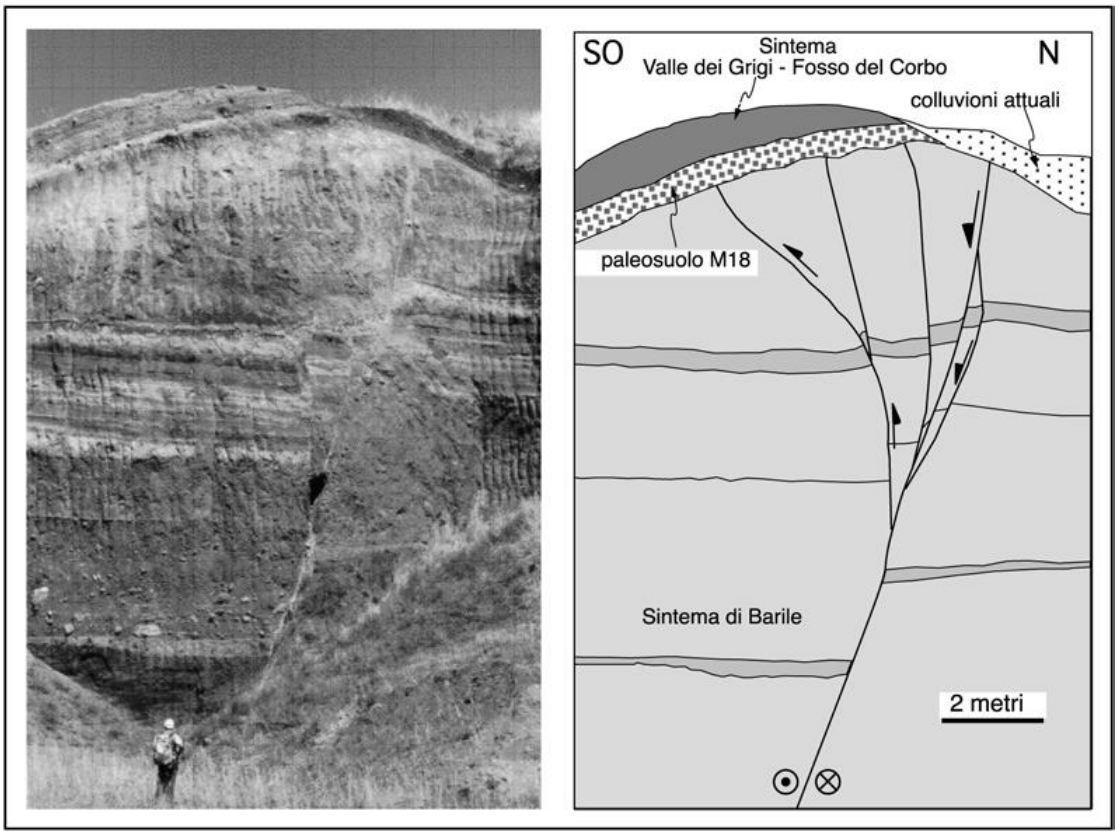

Figure 17 *- Flower structure affecting the Barile Synthem, located close to Case Lopes locality (Schiattarella et al., 2005).*

The normal faults, with an anti-Apenninic trend, instead form conjugate systems, generated by extension in the anti-Apenninic direction (NE-SW). The conjugate systems affect all Mt. Vulture's products to testify to a more recent extensional deformation affecting the front of the chain with the axis of maximum extension in an anti-Apenninic direction (Schiattarella, 2005). These elements allow to place a chronological upper constraint on the deformation activity expressed by transcurrent faults with a reverse component in the Vulture area, which confirm the transition from transpressive to extensional conditions during the middle Pleistocene also in Vulture zone. The landscape changed radically with the extensional activity. Faults with

different orientations and pluridecametric displacement disarticulated the volcanic building. The last phases of volcanic activity take place on an apparatus already dismembered by tectonic events and dissected by the hydrographic network, which appears as a landscape with strong structural control. In conclusion, the three tectonic-evolutionary stages that affected the Quaternary volcanites and the adjacent sedimentary deposits during the Pleistocene, were preceded by an important tectonic event under contractional conditions accompanied by structural transfers and local extension to the NW-SE axis.

4.2.2 Bedrock sedimentary Units

Meso-Cenozoic bedrock Units

The Meso-Cenozoic bedrock is mainly composed of Neogene orogenic prism elements (Prosser et al., 1996) which include both basin pelagic sediments (*Lagonegro Units*, Scandone, 1967; 1972) and the terrigenous sediments of the Irpinia Units (Cocco et al., 1972; Pescatore, 1978). It was produced by the initial compressional tectonic phases due to the westward subduction of the Adriatic microplate. The sedimentary successions of the Meso-Cenozoic bedrock from the oldest to the youngest are:

- *PESCOPAGANO FORMATION – "FLYSH ROSSO AUCTT."* (CRETACIC-OLIGOCENE; PESCATORE ET AL., 1999). The formation is constituted mainly by marly clay, grey, brown, and red, laminated, with intercalation of massive and gradated calcarenites, thickness 10-50 cm (pelagic and turbiditic deposits).
- *PAOLA DOCE FORMATION* (UPPER OLIGOCENE- LOWER MIOCENE; PESCATORE ET AL., 1999). It is composed of medium and fine grain calcarenites alternated with marly limestones, marls, and calci-siltites; bed thickness 10-40 cm. The total thickness of 150 m.
- *NUMIDIAN SANDSTONE "FLYSCH NUMIDICO AUCTT."* (BURDIGALIAN-LANGHIAN?). The Numidian sandstone outcrop like monoclines with NW-SE and N-S directions, mainly characterized by coarse, massive, yellowish quartz-arenites (thick-beds up to 9 m; thin-beds of 30-80 cm) with decimetric interlayers of clayey marls (turbiditic deposits). Total thickness up to 300 m.
- *SERRA PALAZZO FORMATION* (UPPER BURDIGALIAN-SERRAVALLIAN; GALLICCHIO AND MAIORANO, 1999). It is composed of yellow stratified sandstones, grey siltites, and greyish silty clays with interlayered greyish calcarenites (turbiditic deposits). Whitish

calc-siltites and calcarenites (thin beds 4-8 cm) with wave-ripple laminations and interlayers of calcareous marls (pelagic and turbiditic deposits).

- *FAETO FLYSCH* (UPPER BURDIGALLIAN-SERRAVALLIAN). The flysch is constituted by gray, whitish marly clays and silts with intercalations of calcarenites, marly limestone, and sandstones: thin beds 5-30 cm (turbiditic deposits). Total thickness 300-400 m.
- *MARLY CLAY COMPLEX* (CRETACIC-LOWER MIOCENE). This complex shows an intense tectonic deformation and is separated from the previous formations by a tectonic contact. It is composed of red, green, and grey chaotic and strongly deformed clays and marly clays, with olistolites up to 300 m, made up of quartz-arenites and arkoses.

Miocene Units unconformably laying on the Meso-Cenozoic bedrock

- *CERRETA-BOSCO DI PIETRA PALOMBA SANDSTONE*. It lays unconformably on the Meso-Cenozoic bedrock, showing heterogeneous features, inferred to the presence of lateral changes of different lithological terms. The Unit is mainly composed by massive coarse yellow sandstones (thick-beds 7-8 m) alternated with massive conglomerates (thick-beds 4-5 m) eteropic with yellowish sandstones (thick-beds (10-50 cm) with *Bouma sequences Ta-b, Tb-c,* and *Ta-c,* alternated with thin grey clays and marly clays, laterally correlated with intercalation of sandstones with *Bouma sequences Ta-c* and *Tb-c* (turbiditic deposits).

4.2.3 Plio-Pleistocene pre-volcanic units

The Plio-Pleistocene pre-volcanic units constitute the more recent part of the sedimentary succession of the Ofanto river basin that was classified as a *piggy-back* basin by Hippolite et al. (1994b). It consists of deposits inferred to the uplift of the southern Apennine during the Upper Pliocene – Lower Pleistocene, when took place the separation of the Ofanto River Basin and the *Bradanic Foredeep*. The Plio-Pleistocene pre-volcanic units are included in the *Fiumara di Atella Supersynthem*, which was divided into two *Synthems*:

- *DIFESA SYNTHEM* (UPPER PLIOCENE; GIANNANDREA, 2003). It is composed of massive, pebble-supported, coarse-grained conglomerate, with trough cross-bedding and rare intercalations of sands, silts and clays with lamination (marine fan-delta). The Unit reaches its maximum thickness of 400 m close to the Ofanto River in *La Difesa* locality.
- *MONTE SIRICO SYNTHEM* (UPPER PLIOCENE – LOWER PLEISTOCEN). This Synthem represents the ending part of the Ofanto River Basin formation and reaches a maximum

thickness of 250 m. It is composed of sedimentary *facies* associated to an *endoreic* basin, constituted of massive, pebble-supported, coarse-grained conglomerate, characterized by both planar-bedding and cross-bedding, with intercalation of sand, silt and clay with thin lamination (deposits of floodplain and alluvial fan) and rare fossils (plant fragments and loose bones of continental mammals).

4.2.4 Units of Mount Vulture volcano

Mt. Vulture's volcanites and clastic and epiclastic deposits, as previously stated, were classified using Vulcan-Stratigraphic units (UVS) until a few decades ago (La Volpe and Principe, 1989). However, the UVS did not allow us to gather the volcanic deposits together with the clastic and epiclastic deposits of the associated sedimentary basins and prevented internal subdivisions of the volcanites themselves. Recently, as part of the CARG-CNR project (Sheet 451 "Melfi" and Sheet 452 "Rionero in Vulture"), Giannandrea et al. (2006) were able to update the stratigraphic division by introducing the *Unconformity Boundary Stratigraphic Units* (UBSU; Salvador, 1987, 1994) (Fig.18).

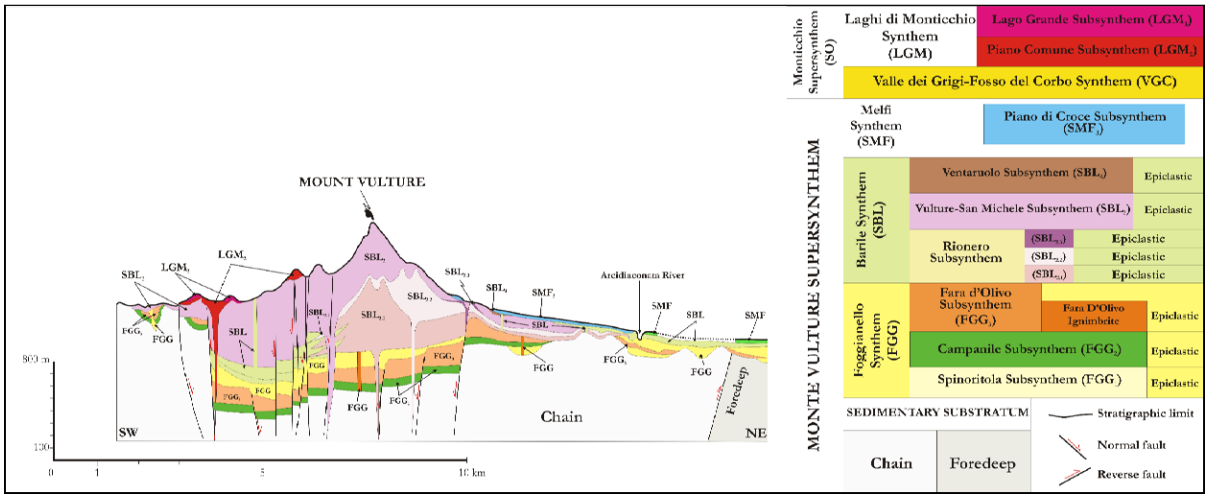

Figure 18 *– Scheme of the stratigraphy of Mt. Vulture volcano subdivided in two Supersynthem (from Giannandrea et al., 2006; modified).*

The new stratigraphic framework has allowed to elaborate a more detailed evolutionary history of the volcanic activity of Vulture and to connect the volcanic activity to the larger-scale geological variations that affected the external face of the southern Apennines (Giannandrea et al., 2006).

The whole volcanic units were grouped into the *Supersynthems* of Monte Vulture and Monticchio, which are traceable on a regional scale in all Quaternary sedimentary basins. The

two *Supersynthems* are divided in *Synthems* and *Subsynthems* which are relative to the volcanic activity from the Middle-Pleistocene to Upper-Pleistocene.

- **MONTE VULTURE *SUPERSYNTHEM*** (MIDDLE-PLEISTOCENE)

The Monte Vulture *Supersynthem* is the oldest and volumetrically important *Supersynthem* and forms the base of the volcano (Giannandrea et al., 2006). It crops out mainly in Toppo San Paolo area and includes the volcanic products that formed the volcanic building, including volcanites from different eruptive phases. The base of the *Supersynthem* is represented by either an erosive surface, which affected the whole quaternary sequence of the Bradanic Foredeep, or a paleosoil in the areas not affected by erosion. The *Supersynthem* is topped by paleosoil *M18* (La Volpe and Principe, 1989; 1991) (Fig.19), which seals the tectonic phase responsible for the dismemberment of the volcanic edifice and the collapse of its SW quarter. The Monte Vulture *Supersynthem* includes the Foggianello, Barile, and Melfi *Synthems*.

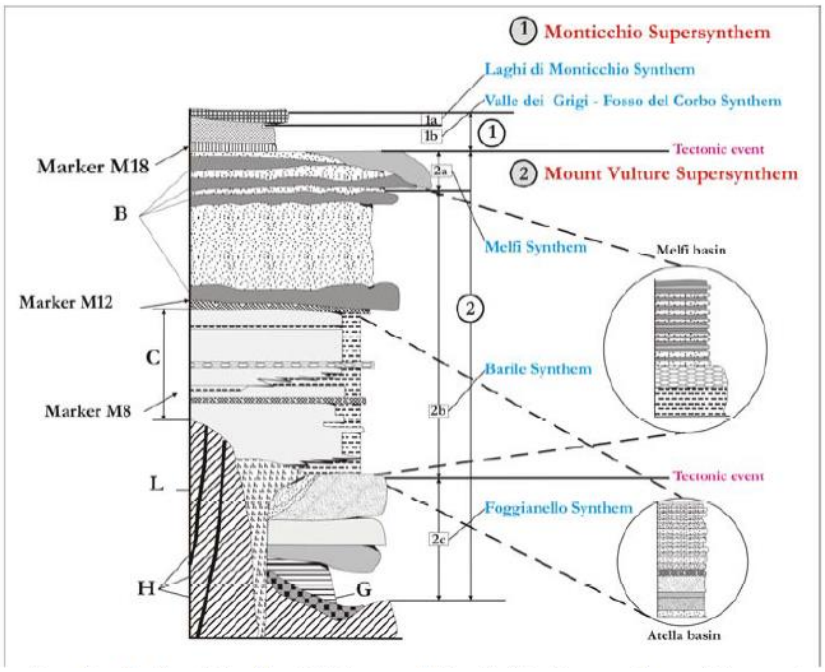

Figure 19 *– Stratigraphic sketch of the Mount Vulture and Monticchio Supersynthems (Giannandrea et al., 2006; modified). In figure are shown the different paleosoils (by La Volpe and Principe, 1989; 1991).*

- FOGGIANELLO SYNTHEM. It is the oldest *synthem* and presents trachytic veins among its products (Principe and Giannandrea, 2006). The trachytic veins are characterized by large k-feldspar and plagioclase phenocrysts (Hieke Merlin, 1967) and crop out East of Melfi. The genesis of these products, dated 730 ± 20 Ka (Brocchini et al., 1994), probably marks the beginning of Vulture's activity, followed by a short quiescent phase, evidenced by a massive epiclastic breccia. Ash deposits (fall and pyroclastic deposits)

and two ignimbrite units are present on the top of epiclastic breccia and are separated from each other and the underlying deposits by two paleosoils.

The *Foggianello synthem* crops out in Atella, along the *Fiumara dell'Arcidiaconata* and in the locality of Foggianello and Gaudianello (Giannandrea et al., 2006). It is divided into three *subsynthems*: *Spinoritola, Campanile,* and *Fara D'Olivo subsynthems*. The *Spinoritola subsynthem* is the basal unit. It is composed of the products of the first phases of volcanic activity, linked to the intrusion of veins along the fractures oriented in the N 30-40° direction. The subsynthem also includes the trachy-phonolitic dikes that cross-cut the sedimentary substrate (*Flysch di Faeto*, Giannandrea et al., 2004). The dikes crop out on the Spinoritola hill and probably their breakup formed the pebbles and blocks found in the conglomerates and breccia of subsynthem, outcropping downstream of the same hill. This first intrusive phase was followed by a pyroclastic phase (*Subsynthem of Campanile*), also associated with a lava activity, highlighted by the presence of lava stone in the pyroclastic deposits. The trachy-phonolitic ignimbritic units A and B of *Fara D'Olivo Subsynthem* are on the top of the *Subsynthem of Campanile* (Hieke Merlin, 1967; De Fino et al., 1982, 1986; Crisci et al., 1983). The ignimbrites are organized in metric banks of centimetric pumice in a massive medium ash matrix (pumice and ash pyroclastic flow; La Volpe & Principe, 1989) and subordinately with cross-stratification. Subsequently, a calderic depression formed due to the emptying and subsequent collapse of the magma chamber. In this depression, a lake basin was formed. Later, during a long period of quiescence, morphogenetic processes produced large volumes of epiclastic deposits (erosive phase *"Flaminia"* in Bonadonna et al., 1998).

- *BARILE SYNTHEM*. The deposits of Barile synthem lay on the erosional surface that affects the ignimbrites. These deposits consist of huge volumes of volcanites that formed the stratovolcano of Mt. Vulture. The Barile synthem crops out on the whole building of Mt. Vulture and is formed both by volcanites in primary facies and by epiclastic fluvio-lacustrine sediments of the Melfi, Atella, and Venosa basins (Giannandrea et al., 2006). This unit is represented by the phonolithic lava dome (De Fino et al., 1982) of *Toppo San Paolo* (646.3 ± 6.7 ka in Brocchini et al., 1994) at the bottom. Upward is present a thick alternation of decametric layers of lapilli, pumice and tephritic and foiditic scoria (De fino et al., 1982), which present at different stratigraphic heights numerous paleo-soils and erosional surface. In the upper part of the unit pyroclastic flow deposits are present. They are formed by massive ash that contains decametric lava blocks with

intercalations of lava flows. The lava flows have a scoriaceous and massive texture and a composition from foiditic to tephritic/basanitic (De Fino et al., 1982).

Fall deposits (decametric layers of grey-greenish lapilli, pisolitic ash) and pyroclastic flow (624 ± 35 ka in Brocchini et al., 1994) close the synthem. The volcanic products were emitted by several volcanic buildings divided into the *subsynthems of Toppo San Paolo, Rionero, Vulture-San Michele,* and *Ventaruolo* (Giannandrea et al., 2006).

The *Toppo San Paolo subsynthem* consists of a lava dome located on the north-eastern edge of Mt. Vulture. The lava dome has an age of 646.3 ± 6.7 ka (Brocchini et al., 1994) and a phonolitic composition (k-feldspar, leucite, haüyna, clinopyroxene, and garnet; De Fino et al., 1982). The pyroclastic deposits of the *Rionero subsynthem* lie on the lava dome, separated by epiclastic deposits and an erosive surface (Giannandrea et al., 2006).

The *Rionero subsynthem* is formed by both pyroclastic deposits (fall and surge deposits) and by epiclastic deposits of alluvial and lacustrine environments laterally correlated, outcropping on the edges of the central building (Giannandrea et al., 2006). Two different overlapping sequences (sequences A and B) are present in the volcanic products, probably deriving from several contemporary eruptive centers.

Sequence A, the *Masseria Boccaglie unit*, consist mainly of pyroclastic surge deposits and subordinately of fall deposits. Sequence B, the *Barile-Rionero unit*, is composed of a dense alternation of pyroclastic fall deposits and subordinately by pyroclastic surge deposits. These deposits, consisting of scoria and pumice lapilli and ash, are organized in layers of different thickness ranging from decimetre to meter (Giannandrea et al., 2006).

The *Vulture – San Michele subsynthem* constitutes the main volcanic building (Principe & Giannandrea, 2006). Its product consists of a juvenile ash matrix, in which blocks and lava bombs up to one meter in diameter and rare metric blocks of layered tuffs are scattered. These deposits are attributed to "*block and ash flow*" pyroclastic flows, to which thin lava flows (foidites, tephra-foidites, tephrites, and basanites) are intercalated (Hieke Merlin, 1967; De Fino et al., 1982; 1986). The age of lava flows ranges between 601 ± 7 and 629.6 ± 4.7 ka (Brocchini et al., 1994).

The Vulture – San Michele succession is cut by a series of dikes (tephrites and basanites, Giannandrea et al., 2006) along the *Grigi Valley*. The construction of volcanic cone died down with the *Vulture – San Michele subsynthem* and a phase of progressive destruction of the relief began.

The *Ventaruolo subsynthem* (624 ± 35 ka, Brocchini et al., 1994) is the final term of *Barile synthem*. It consists of ash with laminated and wave structures (surge) and multiple "block and ash flow type" pyroclastic flow units. Layers of gray-greenish fall lapilli and numerous layers of massive fall ash and subordinately with laminated and wave (surge) structures are intercalated with pyroclastic flows. Sands and pelites with volcanic elements in cm-size beds with planar lamination and through cross-bedding (lacustrine deposits) and massive layers of coarse-grained volcanic sands (lahar) are present at *Incoronata*, near Melfi (Giannandrea et al., 2006).

- *MELFI SYNTHEM.* Volcanic products and epiclastic deposits (*Gaudo* and *Solagne Arcidiaconta subsynthems*) are between the *Ventaruolo subsythem* and the next *Monticchio supersynthems*. They formed the *Melfi synthem*, which is characterized by two lava flows (*Castello di Melfi and Piano di Croce subsynthems*).

  The *Melfi synthem* is represented by the lava flow of *Melfi Hauynophyre* (Hieke Merlin, 1967; 557 ± 7 ka in Bonadonna et al., 1998), which was formed after a quiescent phase of about 40 ka (Schiattarella et al., 2005).

  The *Castello di Melfi subsynthem* consists of epiclastic deposits and lacustrine deposits of ash, silt, and clay in thinly laminated layers of a small lake. The thin lava flow of the hauynophyre is located above these thinly laminated layers (Giannandrea et al., 2006). The lava flow also presents a columnar fracture, probably caused by the deposition in the waters of the underlying lake (Giannandrea et al., 2006).

  The lava flow of *Piano di Croce subsynthems* is the most extensive that crops out on Mt. Vulture. It, like the hauynophyre, has a particular abundance of hauyna phenocrysts that give it a very particular chemism.

- **MONTICCHIO SUPERSYNTHEMS** (MIDDLE-UPPER PLEISTOCENE)

The volcanic deposits of *Monticchio supersynthems* were generated after a long period of inactivity of the Mt. Vulture volcano (Schiattarella et al., 2005). They are mainly linked to a hydromagmatic activity and are often associated with small monogenic eruptive centers. These monogenic centers are characterized by a limited dispersion of the deposits, by the presence of abundant volcanic clasts with ultrafemic composition and xenolith of mantle origin, and by a compositional and petrochemical affinity (Jones et al., 2000; Rosatelli et al., 2000; Downes et al., 2002). Very important are the carbonatitic and melilitic products (132 ± 12 ka in Brocchini et al., 1994) of the two Monticchio Maar (Principe & Stoppa,

1994; Stoppa & Principe, 1997) and two diametric eruptive centers that crop out along the *Arcidiaconata* valley (Principe & Giannandrea, 2006). 2

The *Monticchio supersynthem* is divided into *Valle dei Grigi – Fosso del Corbo* and *Laghi di Monticchio synthems*, which include volcanic products distributed on the slopes of Mt. Vulture and also outside it (Giannandrea et al., 2006). Terraced alluvial deposits outcropping in the valley of River *Ofanto* and *Fiumara di Atella* (Giannandrea, 2004), grouped respectively in the *Conza della Campania* and *Fosso Dello Stroppito synthems*, also belong to the *Monticchio supersynthem*.

- VALLE DEI GRIGI – FOSSO DEL CORBO SYNTHEM. It includes volcanic products emitted by three eruptive centres. Two of these are correlated with the products of *Masseria di Cuscito* and *Imbandina subsynthems* and are located along the north-western side of Mt. Vulture. The third eruptive center, instead, the *Casa Lopes subsynthem*, is positioned on the south-eastern side of Mt. Vulture (Giannandrea et al., 2006).

  The *Masseria di Cuscito subsynthem* consists of three depositional units. Deposits of fine-grained cross-laminated ashes and lapilli (pyroclastic surge) and impact sags and massive breccia rich in ultrafemic nodules form the first unit. The second unit, separated from the first unit by an erosive surface, consists of a breccia similar to that of the first layer and finally the third deposit is made of medium-fine laminated ash. All deposits come from a small tuff ring (Giannandrea et al., 2006).

  Volcanic products erupted from a small volcanic center on the northern slope of Mt. Vulture characterizes the *Imbandina subsynthem*. These products show abundant ultrafemic volcanic clasts and mantle xenoliths (Jones et al., 2000; Rosatelli et al., 2000; Downes et al., 2002) and crop out in the north-western portion of the volcanic building near the eruptive center of *Serra di Lupo*. The subsynthem includes an 8 m thick carbonatitic lava flow, intercalated between two massive deposits of proximal pyroclastic breccias, similar to those of *Masseria di Cuscito subsynthem*, and some thin layers of laminated ash (pyroclastic surge; Giannandrea et al., 2006).

  The *Case Lopes subsynthem* lays on the deposits of the stratigraphic marker M18 (La Volpe et al., 1984; La Volpe & Principe, 1989; 1991), the limit that separates the *Monte Vulture supersynthem* from the *Monticchio supersythem*. It includes three different volcanites sequences separated by erosive surfaces related to three different eruptive centers. The first sequence includes finely laminated fine ashes, to which a bank of basanitic black slag is superimposed (Hieke Merlin, 1967), age of 484 ± 8 ka (Brocchini

et al., 1994). Pyroclastic flow deposits composed of scoria banks, fine and coarse ash, with surge wave, impact structures, and abundant sedimentary lithics are above the first sequence. Stratified ash with wave structures (pyroclastic surge) closes the sedimentary succession (Giannandrea et al., 2006).

- *LAGHI DI MONTICCHIO SYNTHEM.* The volcanic deposits produced by five different eruptive centers constitute the synthem. They are grouped in the *Casa Rossa*, *Piano Comune*, *Lago Grande*, *Lago Piccolo*, and *Serra di Braida subsynthems*, related to a tectonic and magmatic system different from the one previously active (Giannandrea et al., 2006).

  The *Casa Rossa subsynthem* crops out along the Ofanto river beneath travertine deposits correlated with the *Caperroni subsynthem* (Giannandrea, 2004), the most recent terraced unit in the river valley. It includes both sedimentary and volcanic deposits. Laminated brown ash (pyroclastic surge) are at the center of the sedimentary succession whereas at the top is an explosive massive breccia bank. Layers of cross-laminated ashes are in the marginal area of the outcrop (pyroclastic surge). Tufysitic lapilli, similar to those of Lago Piccolo subsynthem, are scattered throughout the sedimentary succession (Giannandrea et al, 2006).

  Beds of cm-thick ashes, from fine-grained to coarse-grained, with both parallel lamination and cross lamination (pyroclastic surge), locally with pisolites or mm-size vesicles (vesiculated tuffs), form the *Piano Comune subsynthem*. Clayey silts with varved fine-grained sands and diatoms are locally present at the top of the sequence. Black strombolian lapilli fallout deposit from the *Fontana dei Faggi* center (Giannandrea et al., 2006).

  The volcanic products of *Lago Piccolo* and *Lago Grande subsythems*, which crop out around the two Maars occupied by the Monticchio lakes, are above the *Piano Comune subsynthem.* The two successions consist of cross-laminated ash layers (pyroclastic surge), locally hardened by precipitation of primary carbonate (Stoppa and Principe, 1997, and 1998), alternated with levels of lapilli and fall blocks (Giannandrea et al., 2006).

  The *Lago Piccolo subsynthem* is a sequence of alternating cm-thick ash and lapilli beds, both massive and cross-laminated (pyroclastic surge), with abundant sedimentary and ultrafemic (spinel lherzorlites) lithics. The magmatic fraction is made up of tuffisitic lapilli and ash. The lapilli, with a concentric structure, have mega crystals or ultrafemic

nodules originating in the mantle at the core. The concentric structure of lapilli suggests that magma has risen in a very short time (Stoppa & Wolley, 1997).

The *Lago Grande subsynthem* sequence has an average finer-grained size. It consists of beds of dm-thick ash and lapilli, both massive (fall deposits) and with cross-lamination (pyroclastic surge) and subordinate massive ash deposits with sparse lithics (ash flows). The magmatic fraction is made up of cm- to m-size bombs causing impact sags and ash (Stoppa & Principe, 1997 and 1998; Giannandrea et al., 2006). The age of the tuffisitic lapilli is 132 ± 12 ka (Brocchini et al., 1994).

The outermost subsynthem, the *Serra di Braida subsynthem*, consists of a sequence of ash and lapilli deposits with cross-laminations (pyroclastic surge) alternating with massive deposits with mm-size vesicles (vesiculated tuffs) and abundant sedimentary lithics (sandstones). The magmatic fraction is formed by tuffisitic lapilli with nuclei of pyroxene and olivine crystal aggregates (Giannandrea et al., 2006).

4.2.5 Post-volcanic units (Upper Pleistocene)

The post-volcanic units belong to the *Monticchio Suprsynthem*. They consist of units of Mount Vulture volcano and related sedimentary basins that are grouped into different synthems. These synthems represent the units of the Fiumara di Atella and Fosso Dello Stroppito catchments, and units of Ofanto catchment.

- THE UNITS OF THE FIUMARA DI ATELLA AND FOSSO DELLO STROPPITO CATCHMENTS.

They are characterized by three order terraced alluvial deposits, which provide the uplift of the Vulture area determining alternate periods of sedimentation and erosion too. The units are represented by the *Fosso Dello Stroppito synthem*, which in its turn includes the *Spaccatornesi*, *Ponte Giulio*, and *Piano di Garda subsynthems*. The lower limit of the synthem is a thick, red paleosoil.

- PIANO DI CARDA SUBSYNTHEM (MIDDLE PLEISTOCENE). It consists of bedded carbonate deposits of high porosity with wavy structures, locally with plant fragments (travertine) (Giannandrea et al., 2006).
- PIANO DI GIULIO SUBSYNTHEM (MIDDLE PLEISTOCENE). The subsynthem includes matrix-supported massive conglomerate with trough cross-bedding (alluvial deposits)

and bedded carbonate deposits with sparse pebbles (travertine) (Giannandrea et al., 2006).

- SPACCATORNESI SUBSYNTHEM (MIDDLE-UPPER PLEISTOCENE). It is formed by clast-supported massive conglomerate with dark red sandy matrix (alluvial deposits) and bedded carbonate deposits with sparse pebbles (Giannandrea et al., 2006).

➢ THE UNITS OF OFANTO CATCHMENT.

The units include the *Conza della Campania synthem*, which comprises the alluvial terraces of the Ofanto river, consistent with the present river framework.

- CAPERRONI SUBSYNTHEM (MIDDLE-UPPER PLEISTOCENE). It consists of red pebble- and mud-supported conglomerates, locally covered by thinly laminated clays and silts (alluvial deposits), bedded carbonate deposits of high porosity with wavy and radial structures and, locally, with plant fragments (travertine) and whitish laminated sands (eluvial-colluvial deposits) (Giannandrea et al., 2006).

➢ PLIO-QUATERNARY UNITS (UPPER PLEISTOCENE-PRESENT).

The units of the Upper-Pleistocene-Holocene consist of chaotic heterogeneous-heterometric deposits with variable lithofacies from clays to big blocks with clayey-sandy matrix (landslide deposits). More recent units (Holocene-present) are represented by deposits of morphological low formed by fine-grained sediments and laminated clays and silts of lacustrine origin. The Plio-Quaternary units consist of fully deposits Ubiquitary Units and Ubiquitary Units under depositions.

CHAPTER 5

HYDROGEOLOGY OF THE MOUNT VULTURE VOLCANIC AQUIFER SYSTEM

5.1 Hydrogeology of the Mount Vulture aquifer

The Mt. Vulture basin, an area of about 180 km, is one of the most important aquifer system of southern Italy and has extremely complex hydrogeological features (Celico and Summa, 2004; Spilotro et al., 2005; Paternoster et al., 2008; Parisi et al., 2011a). The volcano hosts two volcanic *maar* lakes formed about 130 ka ago inside the caldera (Laurenzi *et al*., 1993), called *Laghi di Monticchio*, designed as Site of Community Importance (S.C.I. - Council Directive 92/43/EEC).

The surface drainage network constitutes the natural delimitation of the water catchments. The Ofanto river stream drains the western side of the Mt. Vulture volcano. The river course, due to the progressive uplift of the volcano, underwent displacements in N and NW directions. The *Fiumara di Atella* river, flowing in the *Ofanto* river with E-W direction, drains the south side of the volcano. Finally, the *Fiumara Arcidiaconata* river drains the North and East sides of the volcanic edifice.

The magmatic, pyroclastic and sedimentary sequences and their successive arrangements and tectonic-volcanogenic deformations influence the permeability and anisotropy features of the aquifer. NW-SE, NNW-SSE and E-W normal faults (Beneduce and Giano, 1996; Schiattarella et al., 2005) affect the Mount Vulture volcanic edifice originating a concentric radial pattern jointed to the volcanic activities. The concentric radial pattern controls the evolution of area drainage system, who is predominantly oriented in NW-SE and E-W directions (Ciccacci et al., 1999). In this context, notable importance has *the Grigi Valley - Fosso del Corbo* fault, which crosses the volcanic edifice in WNW-ESE direction (La Volpe and Principe, 1991), in the proximity of some important mineral water springs. This fault caused the downthrown, of about 100 meters, of the southern part of Mt. Vulture volcano, probably by calderic collapse (Boenzi *et al*. 1987), which accomplish an important draining role and widely affects the preferential groundwater flow path. The long-time of the volcano activity (Buettner *et al*., 2006) caused the deformed state of the stratigraphic units that permits to prefigure the groundwater flow

directions. The flow directions are related to the attitude of strata and the local geomorphological situation. The tectonic and structural discontinuities act as deep preferential groundwater flow and promote the mineralization processes of the water.

5.1.1 Hydraulic proprieties of the aquifer host rocks

Mount Vulture hydrogeological basin exhibits a wide range of chemical, mineralogical, structural and hydraulic proprieties, owing mostly to variations in rock type and the way the rock was ejected and deposited.

The volcanic aquifer surface occupies an area of about 130 km^2 (13 km x 10 km). Furthermore, the aquifer reaches a maximum thickness of approximately 1500 meters at the center.

Mainly pyroclastic and subordinated lava flow layers constitute the aquifer core, with different permeable units that locally give rise to distinct overlaid interconnected aquifers (Parisi et al., 2011a). The permeability of volcanic rocks is variable. It is due mainly to their mode of emplacement, the tectonic history, and on weathering processes that often modify the permeability features. The volcanic rocks vary widely in origin, chemical composition and texture, as well as in their capability to transmit water. Pleistocene volcanic rocks host the most productive aquifers in the Mt. Vulture area. The vacuolar and fractured lava flows have a hydraulic conductivity of about $k \sim 10^{-1}$ cm s^{-1}, whereas in the tuff and the incoherent pyroclastic deposits, permeable only for porosity, is less and equal to $k \sim 10^{-3}$ cm s^{-1}. The fluviolacustrine and gravel deposits of the *Fiumara di Atella Supersynthem*, outcropping manly in the S-SW and S-SE sectors, have a value of about $k \sim 10^{-2}$ cm s^{-1} (Parisi et al., 2011a). These different lithological units locally give rise to an overlaid interconnected water bodies, since low permeability discontinuity layers are present (Spilotro *et al*., 2006). The permeability, anisotropy, and structural features of the aquifer are the main factors that control groundwater flow pathways. The piling up of volcanoclastic products outside the central area probably produce a high-medium permeability at large scale. Toward the south-southeast, the volcanic aquifer thickness decreases considerably inducing an important groundwater discharge. In this area, the *Fiumara di Atella Supersynthem* deposits constitute a local extension of the volcanic aquifer whit a relatively low groundwater circulation. Therefore, primarily the properties of the rock matrix and secondarily the existing fracture network control the flow direction and rates (Parisi et al., 2011a; Fig. 20).

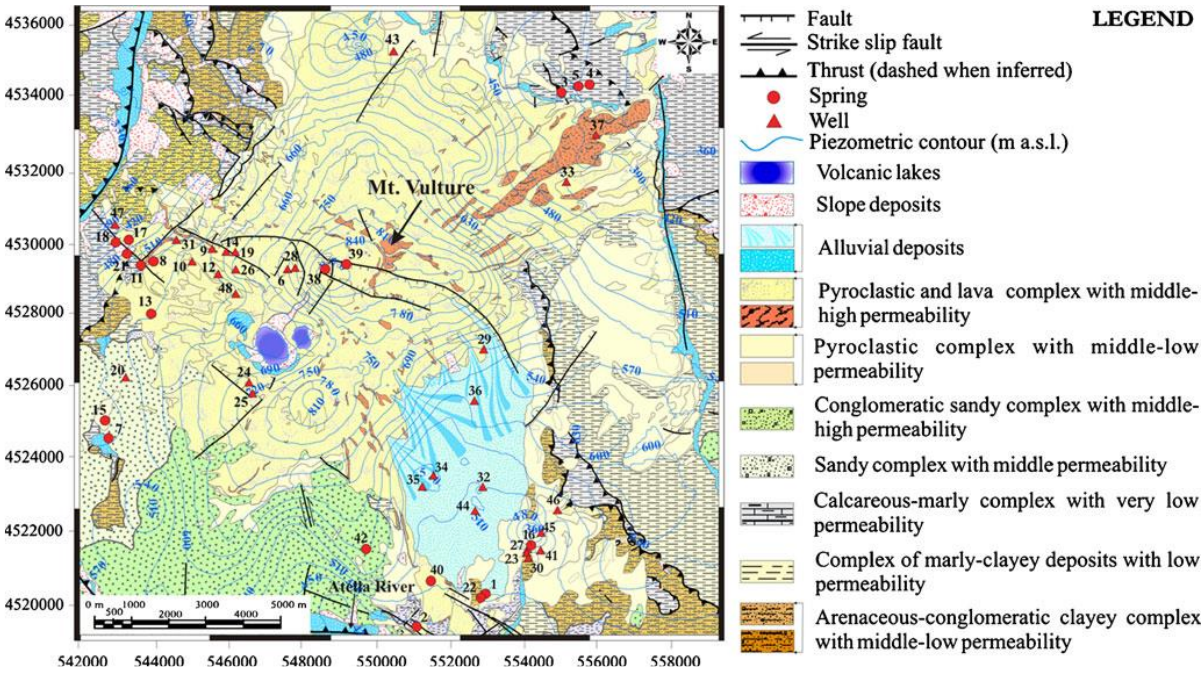

Figure 20 *- Hydrogeological map of the Mt. Vulture basin showing the main hydrogeological complexes (by Parisi et al. 2011a). The contour interval for the piezometric surface is 30 m. The map and the location data are provided in UTM Zone 33 coordinates, using the European Datum of 1950. Geology base map by Giannandrea et al. (2004).*

The permeability values of the aquifer host rocks vary from the highest to the lowest altitudes of the Mt. Vulture basin. The hydrogeological complexes have permeability ranging from middle-high to low. Volcanic products and secondary conglomeratic-sandy complex represent the main hydrogeological complexes. The volcanic products, with high-medium permeability values composed mainly by pyroclastic deposits and subordinate lava flows, are the principally aquifer host rocks of the hydrogeological basin. They consist of mainly pyroclastic deposits and, to a lesser extent, by lava flows. Instead, the conglomeratic-sandy complex, from Plio-Pleistocene pre-volcanic to the fluvio-lacustrine Post-volcanic units, has medium permeability values. The marly-clayey deposits complex, the calcareous-marly complex, and the arenaceous-conglomeratic-clayey complex, representing the bedrock sedimentary Units (from the Meso-Cenozoic Units to the Miocene Units unconformably laying on the Meso-Cenozoic bedrock), correspond to the sedimentary rocks much less permeable than the overlying volcanoclastic products (Parsi et al., 2011a).

5.1.2 Groundwater flow pathways

Recently, Celico and Summa (2004) and Spilotro et al. (2006) proposed two conceptual hydrogeological model for the Mt. Vulture aquifer. Celico and Summa (2004), determined two independent hydrogeological basins: the first one located in the north-east sector (Melfi-Barile

area) and the second one located in the south-southeast sector (Monticchio-Atella area), respectively. Two faults delimited the *Monticchio-Atella basin*, namely by the *Grigi Valley – Fosso del Corbo fault* to the north and the *Southern fault* to the south. Instead, a radial axes drainage characterizes the *Melfi-Barile hydrogeological basin*. The alternation of permeable rocks, locally determines the existence of more inter-communicating basal layers.

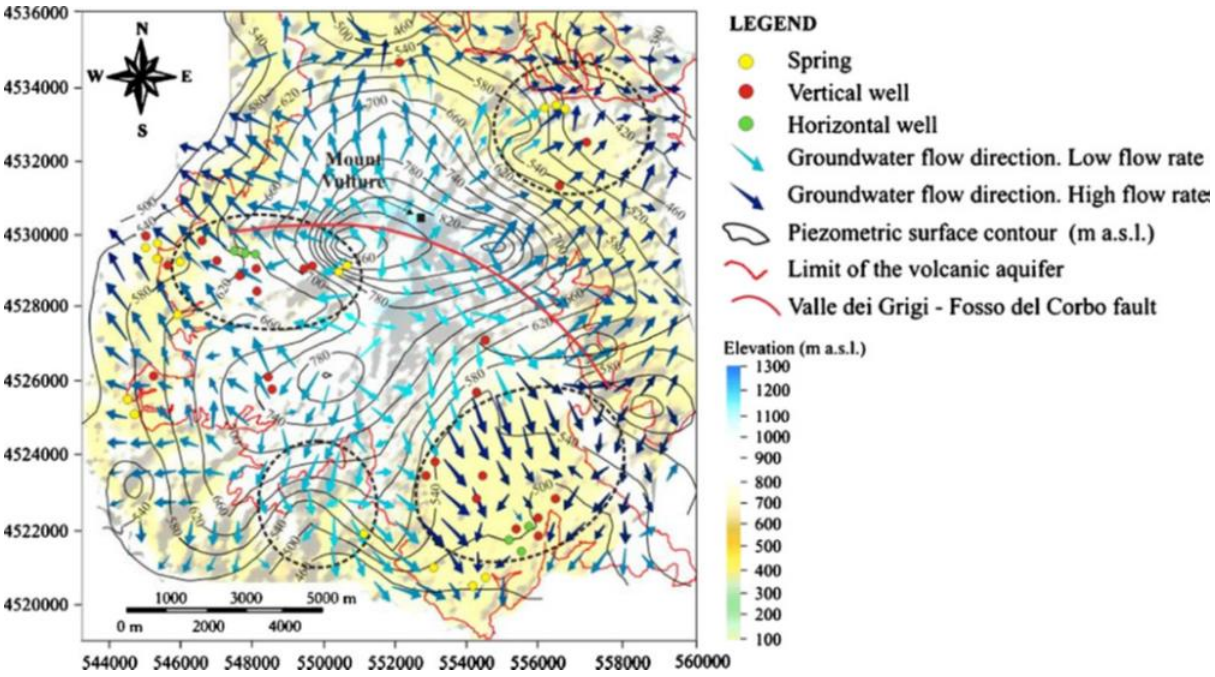

Figure 21 *- Water-table map shows the irregularities of the piezometric surface. The circles drawn with black dotted lines encompass the irregularities of the constant head contour lines. The Grigi Valley–Fosso del Corbo Fault is shown as a red line. The map and the location data are provided in UTM Zone 33 coordinates, using the European Datum of 1950. The contour interval used for the piezometric surface is 40 m. The arrows show the groundwater flowpaths (by Parisi et al., 2011a).*

Later Spilotro *et al*. (2005; 2006) proposed a new conceptual hydrogeological model for the Mt. Vulture volcanic aquifer system. The surface drainage network constitutes the natural delimitation of the water catchments, where the pseudo-tectonic structure of *Grigi Valley – Fosso del Corbo Fault* is the only drainage axis widely affecting the preferential groundwater flow path. The magmatic and pyroclastic sequences and their successive arrangements and tectonic-volcanogenic deformations condition the permeability and anisotropy features of the volcanic aquifer, causing locally shallower groundwater flows. Furthermore, the spring regime shows a slightly seasonal variations flow, with higher values in spring and lower values in autumn. In this context, a possible mixing between shallow groundwater with a short residence time and deeper groundwater with the longest residence time does not exclude (Spilotro et al., 2005).

Recently, Parisi et al. (2011a) showed that groundwater flow within the volcanic aquifer circulates from the highest to the lowest altitudes according to radial streamlines. Moreover, the radial distribution of the volcanoclastic products may favour the groundwater flow from the highest altitudes towards the marginal areas, according to the model suggested by Spilotro et al. (2006). Parisi et al. (2011a) suggested the presence of three main sectors within the Mt. Vulture hydrogeological system. The main recharge zone located in the W-NW sector of the volcano edifice close to the drainage axis (*Grigi Valley – Fosso del Corbo Fault*) and two main discharge zones located in the S-SE and N-NE sectors (Fig.21). The groundwater, with an isotopic signature close to that of rainwater, moves along radial flow paths toward the lowest elevations in the S–SE and N–NE sectors but with differences in length and depth. So the geological, geomorphologic, and hydrogeological features of the Mt. Vulture area influence the general trend of horizontal groundwater flow, from the recharge areas towards the outflows sector.

CHAPTER 6

REEs signature of the Mount Vulture's aquifer rocks

6.1 REEs signature of the aquifer rocks

The REEs distribution of the aquifer rock(s) impacts on the REEs' signature of the related groundwater (e.g. Duvert et al., 2015). Moreover, in the recharge zone, the REEs' pattern of groundwater is mostly inherited from the solid matrix (Willis and Johannesson, 2011). However, properties and processes such as the overall chemistry of the solution, pH and Eh environmental conditions, and sorption and complexation phenomena can drastically modify the groundwater REEs' patterns.

In the Mt. Vulture basin, as previously discussed, the aquifer rocks are Quaternary volcanics. The older volcanic products are lavas and pyroclastics, ranging in composition from basanites and foidites to phonolites (Beccaluva et al., 2002). More recent eruptions produced carbonatitic-melilititic rocks (D'Orazio et al., 2008) that may include ultramafic xenoliths and megacrysts of clinopyroxene, amphibole, olivine, and phlogopite.

***Table 2** - Mt. Vulture rocks average REEs abundances and fractionation indexes; $Eu^* = Eu(PAAS)/\sqrt{Sm(PAAS) * Gd(PAAS)}$, $Ce^* = Ce(PAAS)/\sqrt{La(PAAS) * Pr(PAAS)}$. Data from Beccaluva et al. (2002) and D'Orazio et al. (2008)*

PAAS NORMALIZED	La	Ce	Pr	Nd	Sm	Eu	Gd	Tb	Dy	Ho	Er	Tm	Yb	Lu	La/Yb	Eu*	Ce*
Clynopyroxenite	3,59	3,52	-	4,87	5,07	5,85	4,42	-	2,56	-	1,27	-	0,72	0,67	4,96	1,24	0,88
Basanite	4,63	3,80	-	4,01	3,89	4,60	3,34	-	2,17	-	1,22	-	0,96	0,87	4,84	1,28	0,86
Foidite	5,51	4,78	-	4,73	4,61	5,26	3,99	-	2,62	-	1,54	-	1,20	1,09	4,60	1,23	0,91
Tephrite	5,82	4,43	-	4,23	3,86	4,43	3,29	-	2,19	-	1,33	-	1,05	1,03	5,51	1,24	0,84
Melilite	5,57	5,31	-	5,82	6,27	7,06	5,66	-	3,69	-	2,02	-	1,54	1,38	3,62	1,18	0,94
Hauynofiro	8,28	6,13	-	5,45	4,92	5,82	4,15	-	2,49	-	1,50	-	1,24	1,24	6,66	1,29	0,83
Phonolite	7,37	5,03	-	3,47	2,54	2,81	2,07	-	1,17	-	0,78	-	0,70	0,65	10,50	1,23	0,83

In recent studies, Beccaluva et al. (2002) and D'Orazio et al. (2008) determined the REE abundances of different volcanic rocks of Mt. Vulture basin. These data were used to determine the average concentration values of each type of rock, reported as post-Archean average shale (PAAS) normalized values in Table 2. The available data show that, overall, volcanics share very similar REEs' (PAAS) normalised patterns. Moreover, the patterns show a significant light REE (LREE)-heavy REE (HREE) fractionation, ranging from the $(La/Yb)_{PAAS} = 3.62$ value of average Melilite to the $(La/Yb)_{PAAS} = 10.50$ of average phonolite (Fig.22 and Table 2). In contrast, the Ce and Eu anomalies are very homogeneous, fluctuating in the 1.18-1.29 and 0.83-0.94 range, respectively.

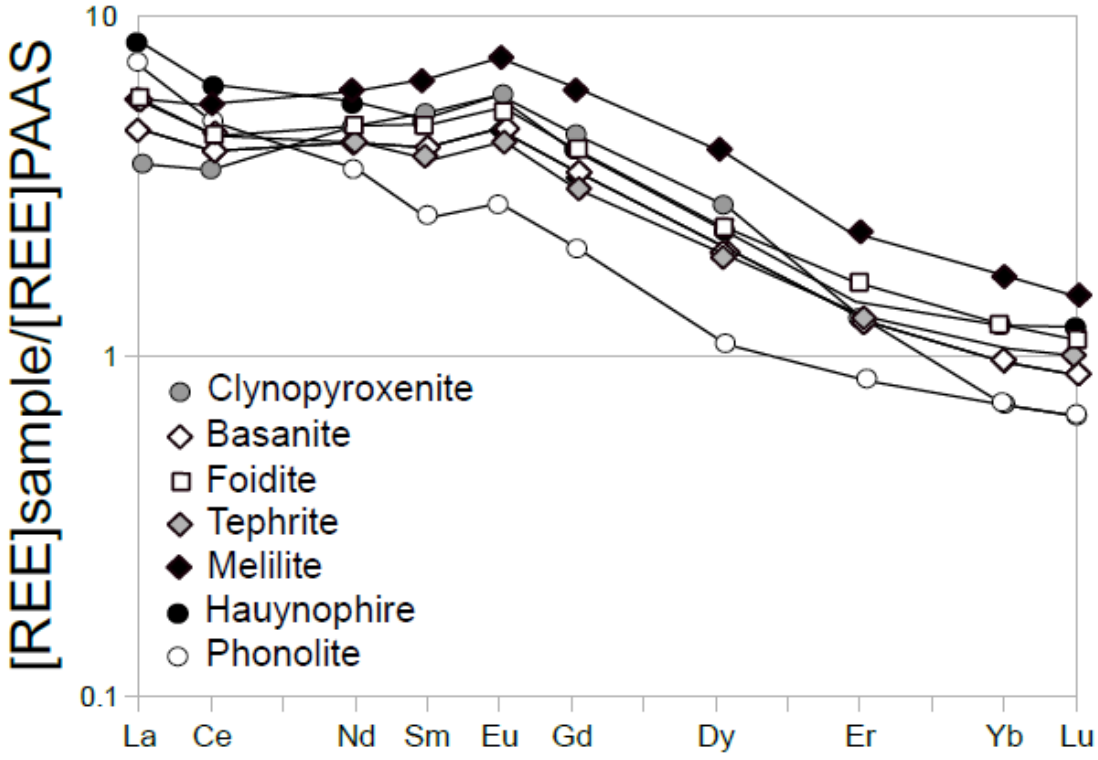

Figure 22 *– Mt. Vulture rocks REEs patterns (PAAS normalized).*

CHAPTER 7

SAMPLING AND ANALYTICAL PROCEDURES

7.1 Sampling and analytical procedures

Before the sampling survey, was performed a census of springs and drilled wells, in order to define a suitable number of sampling sites representative of the Mt. Vulture hydromineral basin. Sampling sites are located roughly in the N-NW, SE, and NE sectors of the study area, mainly within the volcanic products. Fig.23 shows the site locations.

The research project reports analytical data for 37 water samples among drilled wells used for irrigation and drinking water supply and some springs (Fig.23 and 24).

The water samples were collected (Table 3) during a field trip in the dry season (July – August 2018) to record the highest concentrations of dissolved elements (REE and major constituents).

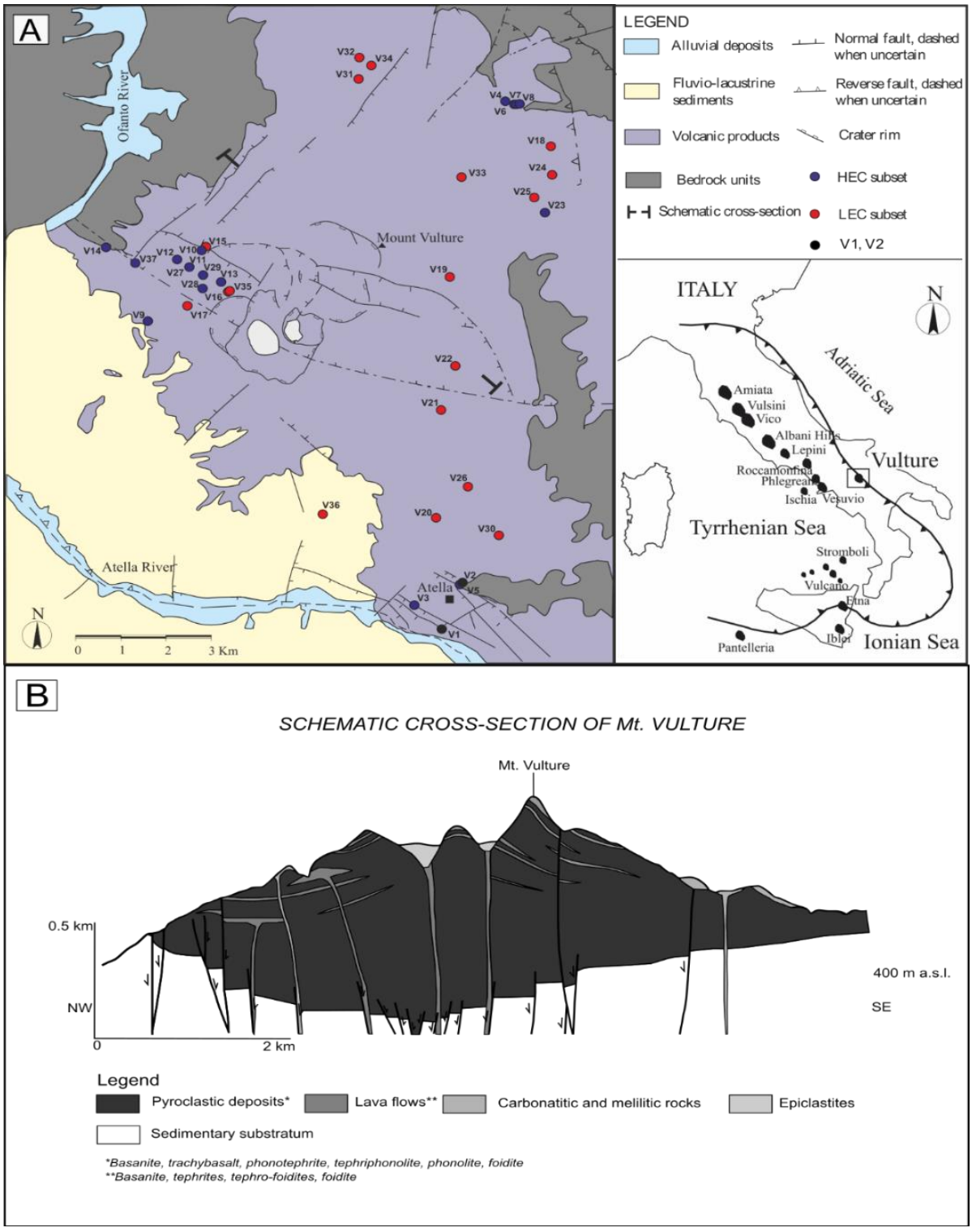

Figure 23 *- A) Geological sketch map of Mt Vulture (modified from Giannandrea et al., 2004). The localization of sampling site (red, blue and black circle) and code of water sample are shown; B) Schematic cross-section of Mt Vulture (modified from Giannandrea et al., 2004).*

Table 3 -*Location of water samples.*

Sample	Location	Latitude	Longitude	Altitude
		WGS84		meters
V1	Atella	4524392	554433	391
V2	Atella	4525617	555266	473
V3	Atella	4525307	553893	442
V4	Rapolla	4536801	556565	360
V5	Atella	4525587	555239	471
V6	Rapolla	4536741	556710	351
V7	Rapolla	4536736	556721	352
V8	Rapolla	4536740	556770	342
V9	Monticchio Sgarroni	4531630	548297	571
V10	Gaudianello	4533377	549547	560
V11	Gaudianello	4533378	549543	560
V12	Gaudianello	4532964	549053	642
V13	Gaudianello	4532487	549968	730
V14	Gaudianello	4533614	547355	406
V15	Gaudianello	4533433	549598	562
V16	Gaudianello	4532345	550225	773
V17	Gaudianello	4531969	549179	639
V18	Rapolla	4536022	557372	391
V19	Mt. Vulture	4532677	555026	907
V20	Atella	4527196	554894	540
V21	Rionero	4529754	554830	631
V22	Rionero	4530931	555333	678
V23	Barile	4534637.4	557118	515
V24	Rapolla	4535383	557365	468
V25	Rapolla	4535004	556953	510
V26	Rionero	4527945	555837	535
V27	Gaudianello	4532746	549319	647
V28	Gaudianello	4532331	549677	683
V29	Gaudianello	4532541	549669	684
V30	Atella	4526867	556228	494
V31	Melfi	4537214	552681	603
V32	Melfi	4537540	552697	581
V33	Rapolla	4535472	555317	586
V34	Melfi	4537417	552836	585
V35	Gaudianello	4532345	550225	773
V36	Atella	4527139	551611	540
V37	Monticchio Bagni	4532890	548125	548

7.1.1 Groundwater sampling

Before collecting the sample, we purged the wells by pumping for at least 30 min, and until the pH, specific conductance, and water temperature stabilized to ensure the groundwaters sampled represented water from the aquifer and not from the boreholes.

Figure 24 *– Spring of bubbling water near the Atella river.*

We stored all water samples for chemical analysis in high-density polyethylene (HDPE) bottles with watertight caps, after rinsing each bottle at least twice with sampled water, and after filtration through a 0.20 μm Millipore filter for cations and REEs analysis. All the HDPE sample bottles used to collect samples for the determinations of REEs were previously acid-washed in the laboratory. Samples for cations and REEs analyses were preserved by acidifying to pH of ~2 with Suprapure HNO_3 (67%). All collected samples were stored at 4 °C until analysis. Moreover, we made a record of every sample collected, and a unique sample number and date identified every bottle, marked on each bottle using a waterproof pen. Other sufficient information like unique sample identification number, the date, exact location, and the water temperature were recorded in a sample book in the field at the sampling site, at the time of sample collection to provide the possibility of sample identification at a later date. For fixing

the sampling points, we used the Global Positioning Systems (GPS), as they supply accurate sampling position data.

7.1.2 In situ analysis

The physico-chemical parameters (temperature, pH, Eh, conductivity, and dissolved oxygen) were measured in situ with high-resolution multiparametric probes (Orion 5 star; Fig.25), after appropriate calibrations in the laboratory before each sampling campaign. The total alkalinity and dissolved SiO_2 were also determined in situ by titration with HCl (0.1 mol/l) using a mixed (methilred-bromocresol green) indicator and a portable spectrophotometer by the heteropoly blue method (Boltz and Mellon, 1947), respectively.

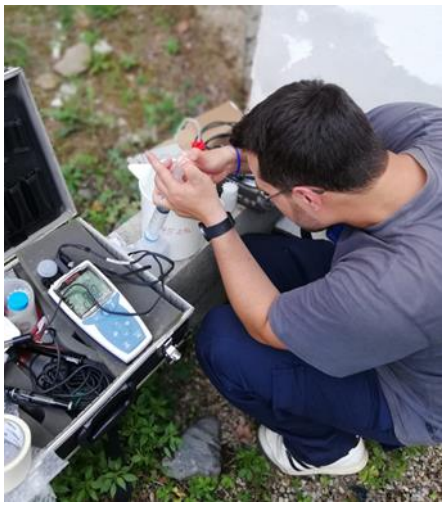

Figure 25 *– in situ filtration and measurement of physico-chemical parameters of a water sample.*

7.1.2.1 pH

The pH is a numerical scale used to specify the acidity or basicity of an aqueous solution. The pH scale is logarithmic and inversely indicates the concentrations of hydrogen ions in the solution (a lower pH indicates a higher concentration of hydrogen ions). It is linked to the formula used to calculate pH approximates the negative of the base-ten logarithmic of the molar concentrations of hydrogen ions in the solution. More precisely, pH is the negative of the base-ten logarithm of the activity of the hydrogen ion. Knowing the pH value in natural waters is very important, since many chemical and biological processes occur only for certain pH values.

The pH of the water was determined using the potentiometric method. The method involves measuring the difference in potential between the measuring electrode and a reference electrode with a known potential with the aid of a pH meter.

The probe is generally a glass electrode consisting of a spherical glass membrane, permeable to H^+ ions. Inside, it contains the reference electrode in contact with a solution of hydrochloric acid buffered at a known pH using a saline bridge. In the water sample, between the two interfaces of the glass membrane is a difference in potential. It is a function of the difference between the concentration of the hydrogen ion in the internal solution, buffered at a known pH, and the external one (Guilizzoni et al., 1998). Therefore, the difference in potential between the measuring electrode and the reference electrode with the known potential gives the pH value.

Before use, we calibrated the probe. We performed the calibration by building a two-point calibration curve using two standard buffers at pH 4 and 7.

7.1.2.2 Electric conductivity

Conductivity is a measure of the passage of alternating current. Natural waters show ionic conductivity because positively and negatively charged ions are dissolved in them, which act as carriers of electric charges. Therefore, conductivity gives an idea of the total concentration of ions dissolved in the water.

Electrical conductivity increases with the concentration of electrolytes, as well as with the temperature; since temperature influences conductivity values, we generally report the specific electrical conductivity at 25 ° C in μS / cm.

Very pure water, the one with lower ionic content, has a very low electrical conductivity, whereas groundwater has usually values between 100 and 1000 μS/cm.

We used a probe that works as a quadrupole immersion cell with an integrated temperature sensor for the measurement of electrical conductivity. This electrode reduces the electrode polarization effect, which is a frequent problem with dipolar electrodes. Four platinum rings prevent the passage of current through the measuring circuit. The electrical current is applied only between the outermost pair of the rings, allowing the internal pair to measure the voltage of the solution without polarization phenomena. We set the instrument on the reference temperature of 25 ° C and the percentage correction factor per degree centigrade of 2.30.

We set these parameters, together with the cell constant value verified with the calibration, when we created the working method. The conductivity meter returns conductivity values already corrected for the cell constant and referred to the temperature of 25 ° C. Experimentally, before proceeding with the determinations on the water samples, we determined the cell constant of the electrode. We used a standard Crison solution of KCl at a concentration of 0.0100 ± 0.0005 M with a specific conductivity of 1413 μS / cm for the verification of the cell constant. We set the cell value obtained on the conductivity meter in the cell constant function, to automatically correct all the measurements made on the samples.

7.1.2.3 Eh and Dissolved oxygen

The redox conditions of groundwater strongly affect the mobility and persistence of many contaminants in groundwater. Redox conditions determine whether some chemical constituents, like arsenic and manganese, are released from the aquifer rocks and sediments into the groundwater.

Redox processes require one chemical species that donates electrons and another chemical species that accepts those electrons. As a chemical species donates electrons, it is "oxidized," and as the other species accepts electrons, it is "reduced."

If dissolved oxygen is present in the water, it is the preferred electron acceptor, and the water is oxic. The atmosphere is the source of the dissolved oxygen in water, so the redox conditions in an aquifer near where recharge occurs usually are oxic. If no dissolved oxygen is present, the water is anoxic. However, there are other chemical species (nitrate, manganese, iron, sulfate, and carbon dioxide, in that order) that can accept electrons in oxygen's place. Redox processes typically are enabled by bacteria, which use the energy produced by the reactions.

The redox conditions of the groundwater can be a powerful indicator of contaminants that might be present at elevated concentrations. For example, concentrations of arsenic and manganese are more likely to be present at levels that exceed human-health benchmarks in anoxic groundwater, and concentrations of uranium, selenium, and nitrate are more likely to exceed their threshold groundwater.

Groundwater age is often related to redox conditions. In general, young, recently recharged groundwater is likely to be oxic, and older groundwater (groundwater that recharged hundreds, thousands, or even millions of years ago) is more likely to be anoxic. In most aquifers, older groundwater is more likely to be anoxic than younger groundwater because there has been more time for chemical reactions that consume dissolved oxygen to occur. However, redox conditions can vary a lot across short distances because of small-scale variability in aquifers like the irregular distribution of organic-rich layers, or the presence of reduced minerals along fractures, for example.

ORP measurement

ORP stands for oxidation-reduction potential, which is a measure, in millivolts, of the tendency of a chemical substance to oxidize or reduce another chemical substance. The principle behind

the ORP measurement is the use of an inert metal electrode (platinum, sometimes gold), which, due to its low resistance, will give up electrons to an oxidant or accept electrons from a reductant. The ORP electrode will continue to accept or give up electrons until it develops a potential, due to the build-up charge, which is equal to the ORP of the solution. The typical accuracy of an ORP measurement is ±5 mV. Sometimes the exchange of electrons between the ORP electrode and certain chemical substances is hampered by a low rate of electron exchange (exchange current density). In these cases, ORP may respond more strongly to a second redox couple in the solution (like dissolved oxygen). It leads to measurement errors.

We used a 5-star Orion probe for the measurement of the ORP values. Before proceeding with the determinations on the water samples, we calibrated the sensor with an Orion™ ORP Standards for Redox/ORP Electrodes.

RDO® Optical Dissolved Oxygen Technique

The amount of oxygen that dissolves in the water depends on many factors: whether there is adequate time and adequate mixing to fully saturate the water, the water temperature, the air pressure, the salt content of the water, and whether there are substances in the water which consume the oxygen. Since the oxygen content is important for many biological and chemical processes, measurement of the amount of oxygen actually dissolved in a water sample is of great importance.

We used the RDO® Optical Dissolved Oxygen Technique for the measurements of dissolved oxygen in the water samples. In particular, we used an RDO optical probe equipped with an optical cap. An air calibration was performed in water satured air to calibrate the probe. In particular, a sponge was moistened in the calibration sleeve with distilled water. The sponge was then inserted into the sleeve without touching the water-saturated sponge. Finally, we proceeded with the calibration.

7.1.2.4 Alkalinity

We determined the total alkalinity of the samples by acid-base titration, using previously standardized hydrochloric acid. We performed titration in two stages; in the first step, we consider the reaction:

$$CO_3^{2-}{}_{(aq)} + H^+{}_{(aq)} \rightarrow HCO_3^-{}_{(aq)}$$

Therefore, we titrated the solution containing both salts using phenolphthalein as an indicator. We determined only the carbonate at the shading point (pH~8) since the bicarbonate initially present had not yet reacted. We calculated the moles of carbonate from the volume of HCl used for the titration and from its concentration, taking into account that the ratio between carbonate and hydrochloric acid is 1:1.

Afterwards we added the methilred to the solution as an indicator. The bicarbonate present in the solution reacted with HCl according to the reaction:

$$HCO_3^-{}_{(aq)} + H^+{}_{(aq)} \rightarrow H_2CO_{3(aq)}$$

with the formation of carbonic acid. The latter decomposed into water and carbon dioxide according to the reaction:

$$H_2CO_{3(aq)} \rightarrow H_2O_{(l)} + CO_{2(g)}$$

The gaseous carbon dioxide moved away from the solution, and therefore, the reaction became irreversible. Finally, we determined the number of bicarbonate moles from the volume of HCl used for the titration and its concentration. The ratio between bicarbonate and hydrochloric acid is 1: 1.

7.1.2.5 Dissolved Silica

The dissolved silica was determined in situ by the heteropoly blue method (Boltz and Mellon, 1947) with a portable spectrophotometer (Fig.26).

Spectrophotometry is defined as a technique which involves provisions for continuously varying wavelength of the central band and therefore, measuring the absorption of radiation with wavelength by the sample. It is a convenient and direct technique that does not affect changes in the composition and properties of the experimental solutions. The applicability of the spectrophotometry to the determination of traces of metals, non-metals, and organic compounds is one of the main reasons for the broad utilization of photometric methods of analysis.

In spectrophotometric analysis, the intensity of radiation, transmitted by an absorbing medium placed between the light source and the detector, is measured as a function of wavelength. The graph between the intensity of radiation transmitted or absorbed, and the wavelength is called the absorption spectrum and is characteristic of the absorbing component and provides the basis for qualitative analysis.

The intensity of radiation absorbed or transmitted is also a measure of concentration, and this forms the basis for the quantitative analysis. The upper limit of spectrophotometric methods is, in general, the determination of constituents which are present in quantities of less than 1 or 2 percent.

For the measurements of dissolved silica, we used a portable multi-parameter photometer pHoto Flex following the heteropoly blue method (Boltz and Mellon, 1947). In particular, we added Silica HR Molybdate and Silica HR Acid RGT to obtain heteropoly blue. Boltz and Mellon (1947) showed that in acidic solution, soluble silica condenses with molybdate ions to give molybdisilicic acid, which upon reduction, under suitable conditions, forms a heteropoly blue. Moreover, we added Silica HR Citric Acid to avoid interference with possible phosphate and dissolved arsenic. The blue colour produced was proportional to the concentration of dissolved silica.

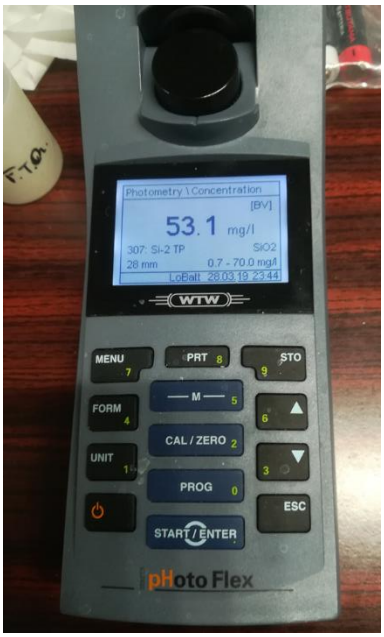

Figure 26 *– Dissolved silica determination with portable photometer pHoto Flex.*

7.1.2.6 Temperature

The water temperature has a marked influence on some organoleptic and physical characteristics. A low temperature makes flavours and smells less evident and makes the water more pleasant. An increase in temperature causes, for example, a faster formation of organ - halogenated compounds in water disinfected with chlorine and its derivatives, an increase in the growth of microorganisms, or an increase in electrical conductivity.

We can measure the water temperature with a mercury or electric thermometer. In the case of easily accessible waters, it can be carried out indifferently with mercury thermometer or with electronics probes. Instead, for checking difficult to reach waters, such as those contained in tanks or wells without pump equipment, it is advisable to use an electric probe equipped with a cable of adequate length or a reversing thermometer.

We measured the temperature of the water samples through a mercury thermometer with a sensitivity of 0.1 ° C. We immersed the bulb of the thermometer in the water until the thermal equilibrium was reached, recording the height of the mercury column for each sample.

7.1.3 Laboratory analysis

The water samples were analysed in the laboratory to determine the concentration of the major elements (anions and cations) and REEs.

7.1.3.1 Major dissolved ions

The concentrations of the major dissolved ions (anions and cations) in the water samples of the Mt. Vulture basin were determined with the ion chromatography technique. This technique allows us to separate and define the ionic components in a solution, exploiting the different reaction characteristics of the analytes.

The separation of the different ionic components in solution is possible due to their different interaction with the mobile and stationary phases.

The input system, the separator column, the detection system, and the data processing system with a recorder constitute an ion chromatograph (Fig. 27).

The analysis technique consists of an ion exchange that takes place between the mobile phase containing the sample and the stationary phase present inside the separator column.

The analysis begins with the introduction of the sample through the mobile phase, which is generally a buffer solution that can contain small quantities of organic solvents.

An injector injects the sample into the system. The sample loading is carried out at atmospheric pressure. After switching the injection valve, the sample is transported to the separator by the mobile phase. Typical injection volumes are between 10 µL and 100 µL.

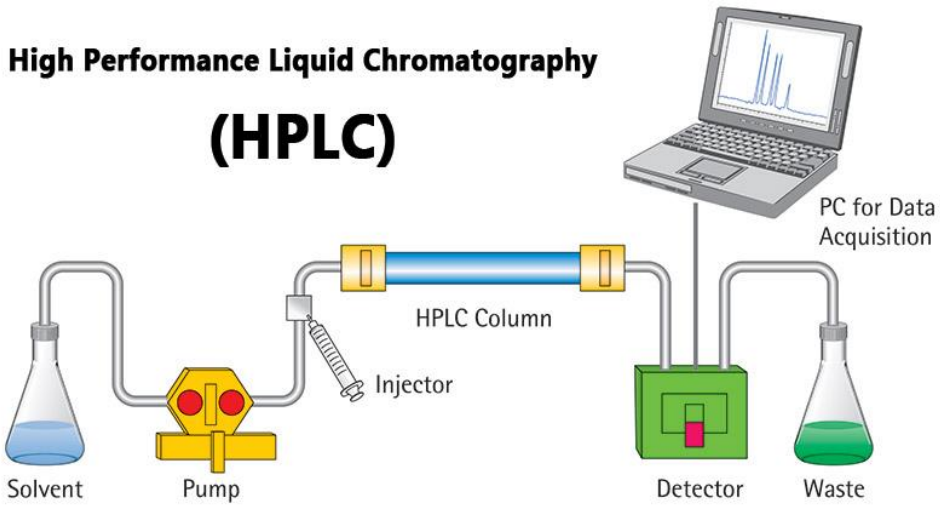

Figure 27 *– Components of a High Performance Liquid Chromatography. Image from www.microbenotes.com.*

Within the column, the migration and separation of the different ionic components takes place based on the distribution of each between the two phases (mobile and stationary). The choice of a suitable stationary phase and chromatographic conditions determine the quality of the analysis. The column tubes consist of an inert material such as epoxy resins. In general, separation is achieved at room temperature.

The stationary phase, located inside the column, is generally made up of polymeric resins, and has the function of retaining the solvent. Functional groups with electric charges are bound on the molecular skeleton of these polymeric resins, which can reversibly exchange the introduced solution. During the separation, the ion behaviour depends on the balance established between it and the active ionized groups of the resin.

A detector is at the exit of the separator column that allows the determination of the various substances; it consists of a conductimetric cell which allows to obtain the retention times, different for each ion.

The chromatograph gives as output a graph called "*chromatogram*" consisting of the instrument signal as a function of time. The chromatogram provides both quantitative and qualitative information. Therefore, each peak in the graph identifies a particular ion. The retention time is the amount of time a compound spends to cross the column and corresponds to the top of each peak in the chromatogram. The higher affinity of a substance for the stationary phase results in a longer retention time. The residence time in the column depends on pH, ion size and charge and is usually quoted in units of seconds or minutes. This information is qualitative.

Instead, the area subtended by the curve provides quantitative information since it is proportional to the concentration of the separate ion. We determine the concentration by comparing the peak area with the analyte calibration curve, constructed with a series of reference solutions at different known concentrations. The precision of the instrument is calculated by analysing the same sample several times and computing the relative standard deviation for each species. Moreover, we determine the accuracy of the method by analysing a reference sample with a known composition and comparing the analytical data with the values shown in the sample certificate.

Major ions determinations were carried out at the University of Calabria on unacidified (F^-, Cl^-, NO_3^-, and SO_4^{2-}) and acidified (Sr^+, Na^+, K^+, Ca^{2+}, and Mg^{2+}) water samples separate aliquots using high-performance liquid chromatography (HPLC, Dionex DX-120; Fig.28).

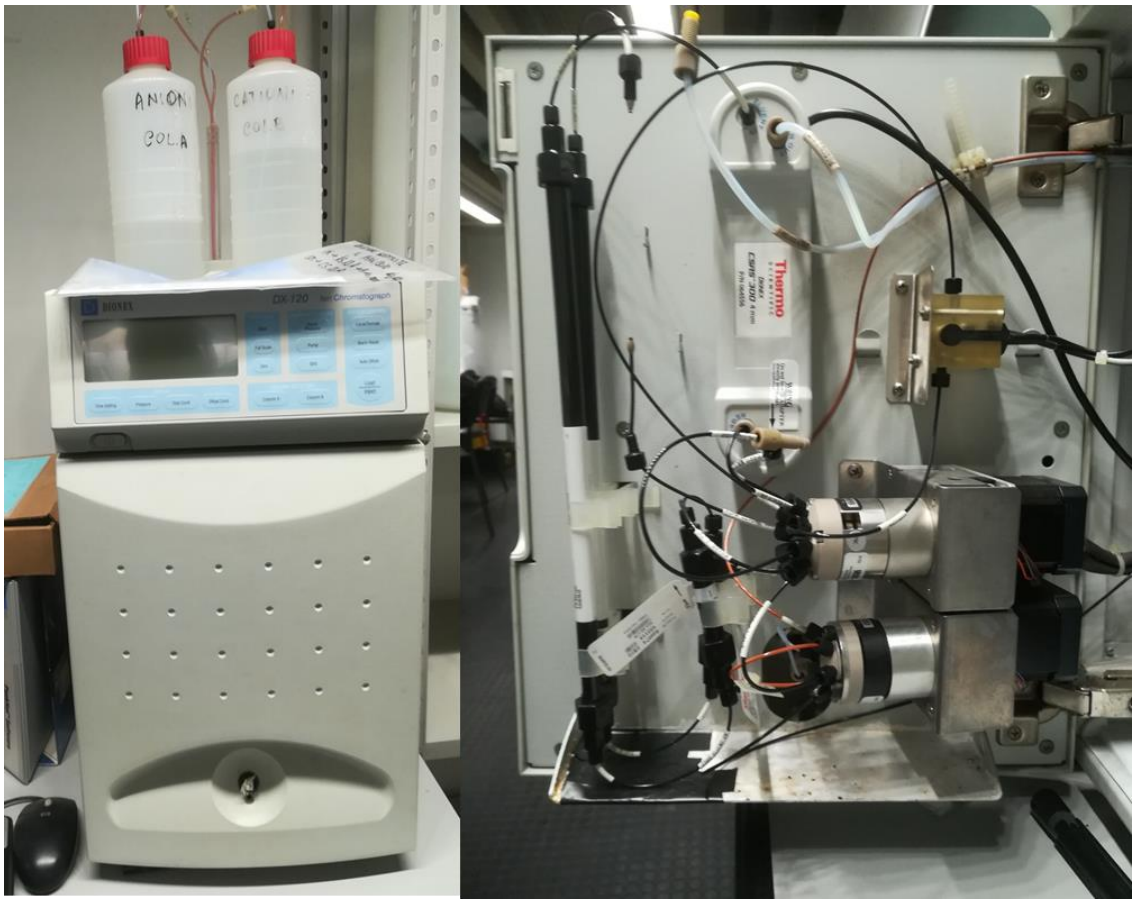

Figure 28 *- HPLC, Dionex DX-120.*

The electroneutrality was estimated to check on the completeness and accuracy of the analysis:

$$\text{Electroneutrality } (e) = [\text{CAT-AN}]/[\text{CAT+AN}] \times 100(\%),$$

where CAT and AN represent the sum of the measured cations and anions, respectively. Values above ± 5% indicate an analytical error in the measurements (Matthess, 1982). This threshold was never exceeded in the analyses performed in this study.

7.1.3.2 Rare earth elements

The REEs' concentrations were determined by inductively coupled plasma-mass spectrometer (ICP-MS) at the National Institute of Advanced Industrial Science and Technology (AIST, Tsukuba, Japan).

Rare earth elements analyses are widely used in geology, environmental science and archaeology. Over the past decade inductively coupled plasma-mass spectrometry has become an important source of rare earth data on geological material.

This technique consists of the combined use of an ionizing plasma torch ICP (Inductively Coupled Plasma) and an MS mass spectrometer (Mass Spectrometry), which has the function of separating and detecting the ions produced. It is an analytical technique based on the separation and individual analysis of ion masses (atomic or molecular) and relative abundances in the gas phase.

In mass spectrometry, discrimination of ionic species takes place according to the mass/charge ratio (m/z). That implies the presence of an ionization source, capable of converting the components of the sample into ions, and a mass analyser, necessary to separate the ions according to their m/z ratio. As a final result, a mass spectrum is obtained, which represents the intensity of the ion as a function of the m/z ratio.

Generally, in an ICP-MS analysis, the sample is introduced atomized by the central tube of the torch through an argon flow. The aerosol of the sample arriving in the plasma collides with free electrons, Ar atoms, and Ar + ions and is atomized and ionized. The analyte is then transformed from liquid aerosol into solid particles and finally into a gas. When it reaches the analytical area of the plasma at an approximate temperature of 6000 - 7000 ° K, it will be in the form of excited atoms and ions representing the elemental composition of the sample. Therefore, atoms lose an electron becoming ions with a single positive charge. The plasma is then aspirated and transported to the detector, which defines the various elements according to the mass.

However, the technique is also characterized by some drawbacks; the occurrence of spectral interferences being the most important one (Tan and Horlick, 1986; Dams et al., 1995; Balcaen et al., 2015). Several approaches for coping with spectral overlap have been suggested, such as (matrix-matched) blank subtraction, mathematical correction, cold plasma conditions (Sakata and Kawabata, 1994), trace/matrix separation, alternative methods for sample introduction, or aerosol desolvation (Minnich and Houk, 1998). Although the application of one of these procedures, or a combination thereof, can lead to accurate results for a wide range of analyte elements and sample types, more straightforward and universal approaches have been developed over the last 20 years. They include the high-resolution sector-field (SF) ICP-MS instruments (Jakubowski et al., 2011) and quadrupole (Q)-based instruments equipped with a collision/reaction cell (CRC) (Feldmann et al., 1999; Tanner and Baranov, 1999; Yamada et al., 2002).

Very recently (2012), it was put on the market the ICP-tandem mass spectrometer (MS/MS) (Fernandez et al., 2012; Balcaen et al., 2013), often also referred to as triple quadrupole ICP-

MS (or ICP-QQQ) (Fig.29). The main difference with the traditional ICP-CRC-QMS systems is the introduction of an additional quadrupole (Q1) in front of the CRC, which can be operated as a mass filter, thereby only allowing ions with one m/z-ratio to enter the cell. This leads to a better control over the reactions taking place in the cell and more insight into the reaction mechanisms and the origin of the reaction product ions observed (Balcaen et al., 2015).

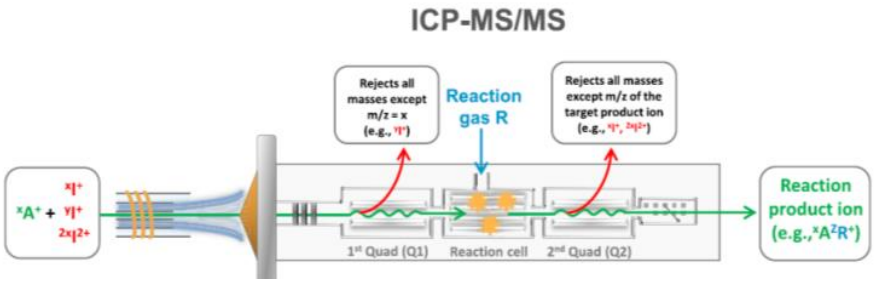

Figure 29 *- Schematic representation of the operating principle of the tandem mass spectrometer system, functioning in MS/MS mode, leading to an interference-free determination of $^{x}A^{+}$ (at the mass of a reaction product ion). A stands for analyte element, I for interference; from Balcaen et al., 2015.*

For the measurement of REEs concentrations, we used an Agilent 8800 Triple Quad (Fig. 30). The instrument can be used in different modes of operation, depending on the nature of the analyte, the matrix elements found in the samples, and the requirements of the analysis in terms of, among other, detection limits and sensitivity (Balcaen et al., 2015).

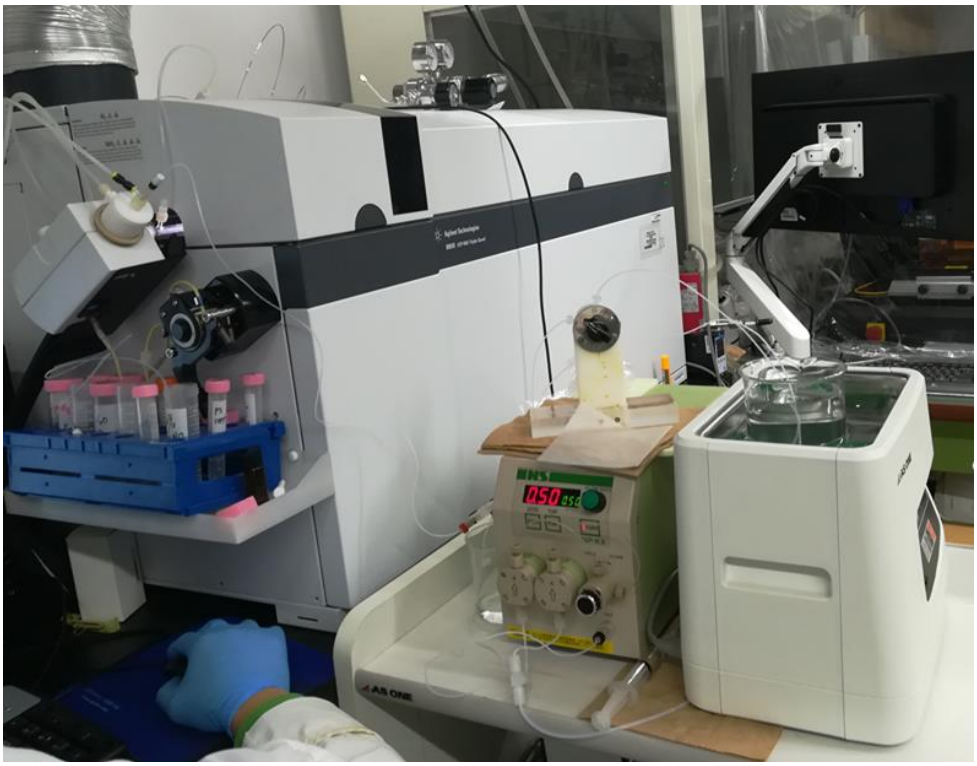

Figure 30 *- Agilent 8800 Triple Quad with on-line elution/on-line measurement system and ultrasonic bath.*

For the determination of those elements that are hindered by spectral overlap, the collision/reaction cell can be pressurized with a (reactive or non-reactive) gas. Instead, Q1 can be used as an ion guide or bandpass ("single quad" mode - comparable to a typical ICP-CRC-MS system) or as a mass filter ("MS/MS" mode). While the addition of a non-reactive gas (e.g., He) in the cell, in combination with kinetic energy discrimination, can lead to a strong reduction of many polyatomic interferences. It is widely accepted that the reaction mode is often more efficient than the collision mode, especially for some key elements (e.g., S, P, Se) and when aiming at ng L^{-1} - level analysis (Tanner and Baranov, 1999). Moreover, with a non-reactive gas, only polyatomic ions can be banned from the quadrupole mass spectrometer, while the use of reactive gases also allows for a reduction of isobaric overlap (Balcaen et al., 2015).

With a reactive gas, spectral overlap can be reduced in two different ways (Fig. 31). Reactions can be induced to:

- Convert the interfering species into a new species that does not longer interfere with the determination of the analyte ion at its natural isotopic mass (on-mass mode), or

- Convert the analyte ion into a reaction product ion, which can be determined free from interference at another mass-to-charge ratio than that of the original analyte ion (mass-shift mode).

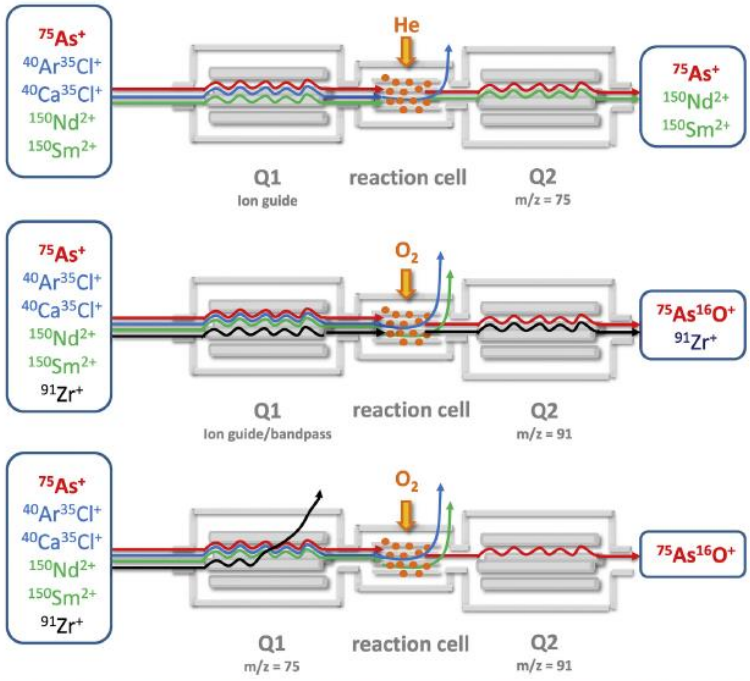

Figure 31 *- Example of the added value of the double mass selection mode (MS/MS) for the determination of As in complex matrices. With Q1 used as an ion guide only, spectral interferences are remaining, while operation in MS/MS-mode allows for an interference-free determination of As when using O2 as a reaction gas; from Balcaen et al., 2015.*

To avoid isobaric interference between LREE and HREE, we used the mass-shifted mode and in particular the oxygen reaction mode. The oxygen reaction mode induces the formation of an oxide ion at a new mass of *mx + 16*, where mx is the mass of the analyte; therefore, the mass of the analyte ion shifted to a new mass away from the original interference, so the new mass is obtained by adding an oxygen atom.

Before proceeding with the analyses, we performed a pre-concentration process on the samples that showed low REE content. These samples were defined through a preliminary analysis in which the roughly concentrations of each sample were determined.

We used the co-precipitation method proposed by Zhu et al. (2010) to pre-concentrate the REEs in the water samples prior to the measurements. First, appropriate quantities of $Fe(NO_3)_3$ and NH_4OH_4 solutions were consecutively added into the water samples to obtain $Fe(OH)_3$ precipitates. Then, the $Fe(OH)_3$ precipitates, used for enriching the REEs, were collected in a syringe filter aided by suction. The syringe filters were connected, one by one, to an on-line elution/on-line measurement system through which the $Fe(OH)_3$ precipitate was eluted by 2 mol/L HNO_3 solution and introduced in the ICP-MS instrument for the determination of the REEs concentrations. During the elution, an ultrasonic bath was applied to obtain a smooth elution profile of REEs from the syringe filter (Fig.32).

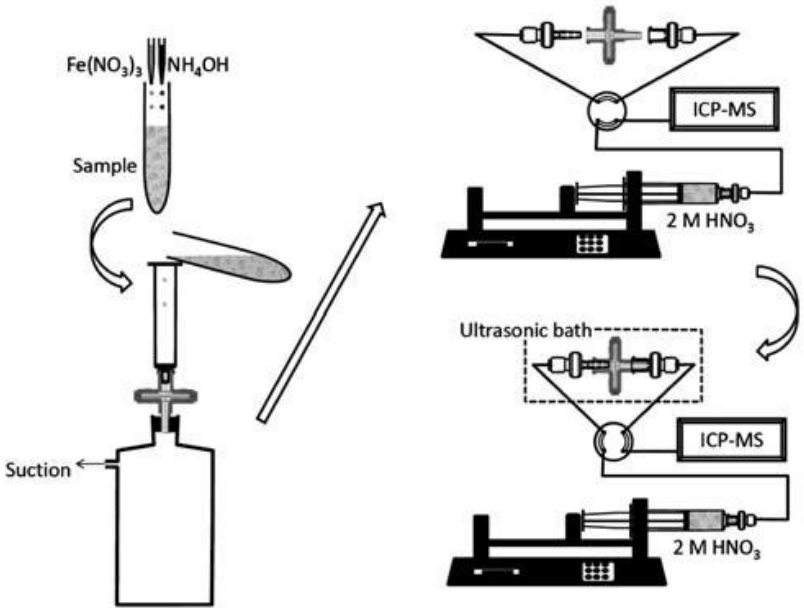

Figure 32 *– Schematic structure of the coprecipitation system, from Zhu et al., 2010.*

The detection limits were <0.098 pg/l for all REEs. The analytical relative standard deviation (RSD) precision was 12% for La; 14% for Ce; 10% for Pr, Sm, and Nd; 7% for Gd, Tb, and Dy; 18% or higher for Lu, Er, Ho, and Yb; and 28% or higher for Tm and Eu.

CHAPTER 8

DATA PROCESSING

8.1 Data processing

The data obtained on the water samples from the chemical analyses (concentrations of the major dissolved elements and rare earths) and the in situ determinations (T, pH, EC, DO, and alkalinity) were processed through the dedicated Geochemist's Workbench software for thermodynamic calculations and the Past3 software for cluster analyses.

8.1.1 Geochemist's workbench

The Geochemist's Workbench (GWB) is an integrated set of interactive software tools for solving a range of problems in aqueous chemistry. The graphical user interface simplifies the use of the geochemical code.

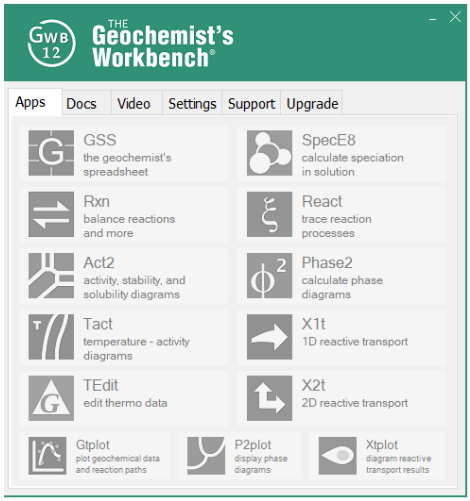

Figure 33 *– GWB graphic interface.*

The GWB is an integrated geochemical modelling package used for balancing chemical reactions, calculating stability diagrams and the equilibrium states of natural waters, tracing reaction processes, modelling reactive transport, plotting the results of these calculations, and storing the related data.

GWB reads datasets of thermodynamic equilibrium constants (most commonly compiled from 0 to 300 °C along the steam saturation curve) with which it can calculate chemical equilibria. Thermodynamic datasets from other popular programs like PHREEQC (Parkhurst, 1995; Parkhurst and Appelo, 1999), WATEQ4F (Ball and Nordstrom, 1991), and Visual MINTEQ have been formatted for the GWB, enabling comparison and validation of the different codes (Gustafsson, 2010). The GWB can couple chemical reactions with hydrologic transport to produce simulations known as reactive transport models. GWB can calculate flow fields dynamically, or import flow fields as numeric data or calculate directly from the USGS hydrologic flow code MODFLOW (Bethke and Yeakel, 2014).

For the treatment of the data of this study, I used the GWB Student Edition, which consists of 7 programs (Fig. 33):

- **GSS** stores analyte and sample data in a spreadsheet specially developed to work with the GWB set of software tools.
- **Rxn** automatically balances chemical reactions, calculates equilibrium constants and equations, and solves for the temperatures at which reactions are in equilibrium.
- **Act2** calculates and plots stability diagrams on activity and fugacity axes.
- **Tact** calculates and plots temperature-activity and temperature-fugacity diagrams and projects the traces of reaction paths.
- **SpecE8** calculates species distributions in aqueous solutions and computes mineral saturation and gas fugacities. SpecE8 can account for the sorption of species onto mineral surfaces according to a variety of methods, including surface complexation and ion exchange.
- **Gtplot** graphs SpecE8 results and GSS datasets, including on xy plots, ternary, Piper, Durov, and Stiff diagrams.
- **TEdit** displays, modifies, and creates the thermodynamic and surface reaction datasets used by the various GWB applications.

8.1.1.1 Data store (GSS)

The water samples data were stored in a spreadsheet on the GSS program. Once the data was loaded, the sheet was loaded into the gtplot program for the construction of binary diagrams, in the SpecE8 program for the calculation of the aqueous speciation, and in Act2 program for the construction of the activity plot. Furthermore, with the GSS program, it was possible to calculate the saturation of minerals and the activities of the aqueous species used for the construction of the activity plots.

8.1.1.2 Act2 (Activity plot)

The Act2 program was used for the construction of the activity plots. These plots show the stability fields of minerals in equilibrium with the aqueous solution and the predominance of aqueous species in chemical systems, using activity, fugacity, activity or fugacity ratio, pH, or Eh as variables of the axes.

The program refers to a thermodynamic database to compute the different plots. Each thermodynamic database contains the following information:

- The activity model used to calculate the activity coefficients (for example the Debye - Huckel model);
- The list of elements with their molar weight;
- The list of basic species (for example $As(OH)_4^-$) with information about the ionic charge, the ionic size, the molar weight and the number of elements that formed the species;
- The list of aqueous species with information about the ionic charge, the ionic size, the molar weight and the elements that form the aqueous species;
- The list of minerals whose formula, molar volume, molar weight and species in a reaction are reported;
- The list of gaseous species with their molar weight;
- The list of gaseous species and oxides with their molar weight.

The first step was to define the most suitable thermodynamic database for the geochemical context of Mt. Vulture basin. We chose the thermo.dat database (Bethke, 1992). Finally, through an iteration process with the thermodynamic database, the program calculated and graphically returned the activity plot. It was possible to insert the representative marker point of each sample in the activity plot by loading the spreadsheet previously saved in the GSS program.

8.1.1.3 SpecE8 (aqueous speciation and saturation index)

SpecE8 is a program designed to compute the distribution of species in aqueous solutions, the mineral saturation, and the fugacity of gases. In this study, SpecE8 was used to determine aqueous REE species in water samples and saturation index.

It was necessary to provide the program with input data to calculate the distribution of the REEs' species in the water samples. The measured physicochemical parameters (T, pH, Eh, electric conductivity, and dissolved oxygen) and concentrations of major elements and REEs were used as input parameters for the calculations.

Thermodynamic calculations were performed using the database “thermos.com.v8.r6+.dat” (Bethke, 1992). The equilibrium constants for aqueous REE species in the groundwater system used for the speciation and saturation calculations are listed in Table 4.

Table 4 *- Formation constants (log units) for aqueous REE species.*

	$LnCl^{++}$	$Ln(CO_3)_2^-$	$LnCO_3^+$	LnF^{++}	$LnOH^{++}$	$LnSO_4^+$
La	-0.31	9.36	3.21	-3.85	8.64	-3.61
Ce	-0.31	8.9	2.93	-4.22	8.42	-
Pr	-0.31	8.58	2.77	-4.22	8.27	-
Nd	-0.31	8.49	2.62	-4.37	8.13	-3.6
Sm	-0.31	8.13	2.48	-4.37	7.99	-3.63
Eu	-0.31	8.03	2.4	-4.44	7.91	-3.64
Gd	-0.31	8.18	2.48	-4.59	7.91	-
Tb	-0.23	7.56	2.4	-4.66	7.83	-3.59
Dy	-0.23	7.46	2.33	-4.66	7.83	-3.57
Ho	-0.23	7.66	2.26	-4.73	7.76	-3.54
Er	-0.31	7.54	2.18	-4.73	7.76	-3.51
Tm	-0.23	7.39	2.11	-4.81	7.69	-3.48
Yb	-0.16	7.36	2.04	-4.81	7.61	-3.46
Lu	0.06	7.29	2.04	-4.81	7.61	-3.44
Ref.	[b]	[a]	[a]	[b]	[c]	[d]

a) Luo and Byrne (2004); b) Migdisov et al. (2009); c) Haas et al. (2005); d) Schijf & Byrne (2004).

The software performed the thermodynamic calculation through a series of iterations of a specific algorithm with the chosen thermodynamic database. The iteration process continues until optimal convergence with the input data is achieved.

The program returns as output a .txt file in which are reported:

- The general characteristics of the water sample like hydrofacies, TDS, alkalinity, water activity;
- The distribution of aqueous species;
- The mineral saturation states;
- The gas fugacity.

8.1.2 Past3

Past3 is free software for scientific data analysis. It has functions for data manipulation, plotting, univariate and multivariate statistics, ecological analysis, time series and spatial analysis, morphometrics, and stratigraphy. This program was originally designed as a follow-up to PALSTAT, a software package for paleontological data analysis written by P.D. Ryan, D.A.T. Harper and J.S. Whalley (Ryan et al. 1995). Through continuous development for more than twenty years, PAST has grown into a comprehensive statistics package used not only by paleontologists, but in many fields of life science, earth science, engineering, and economics.

We used Past3 software for a cluster analysis and for the univariate statistical analysis of water samples.

The hierarchical clustering routine produces a 'dendrogram' showing how data points (rows) can be clustered.

Three different algorithms are available:

• Unweighted pair-group average (UPGMA). Clusters are joined based on the average distance between all members of the two groups.

• Single linkage (nearest neighbour). Clusters are joined based on the smallest distance between the two groups.

• Ward's method. Clusters are joined such that the increase in within-group variance is minimized.

For Ward's method, a Euclidean distance measure is inherent to the algorithm. For UPGMA and single linkage, the distance matrix can be computed using 13 different measures.

In this study, we used the algorithm paired groups (UPMGA) and similarity index Gower to identify separate groundwater subsets.

The univariate analysis computes a number of basic descriptive statistics for one or more samples. In this study the mean, the median, the standard deviation, the Pearson correlation coefficient (r):

- $Mean\ (x) = \frac{\sum Xi}{n}$
- The median of the sample. For *n* odd, the given value such that there are equally many values above and below. For *n* even, the average of the two central values.
- $Standard\ deviation\ (s) = \sqrt{\frac{1}{n-1}\sum(Xi - X)^2}$
- Pearson's r is the most commonly used parametric correlation coefficient. It is given by:

$$r = \frac{\sum_i (Xi - X)(Yi - Y)}{\sqrt{\sum_i (Xi - X)^2}\ \sqrt{(Yi - Y)^2}}$$

CHAPTER 9

RESULTS

9.1 Groundwater physico-chemical features and major solutes

Groundwater geochemistry deals with defining the processes that control the chemical composition of the groundwater produced by the different aquifer systems. However, the heterogeneity of many aquifer systems makes it complicated to define the processes that control the groundwater geochemistry. This heterogeneity is due to the different geological conditions of the formation of the different rocks that compose the aquifers.

Table 5 *- physical parameters and subset of water samples. EC = electrical conductivity; T = temperature; DO = dissolved oxygen; − = no value; TDS = total dissolved solid; HEC = high electrical conductivity; LEC = low electrical conductivity.*

Sample	Flow	T	pH	EC	Eh	DO	TDS	Subset
	l/sec	°C		µs/cm 25°C	mV	µm/kg	mg/L	
V1	-	21.4	6.8	13030	320	2.80	14072	-
V2	0.01	20.1	6.9	19250	276	1.99	20790	-
V3	0.16	16.5	6.4	5680	302	1.45	6134	HEC
V4	0.33	17.1	6.3	2920	473	3.97	3154	HEC
V5	0.04	18.9	5.8	880	529	2.42	950	HEC
V6	-	19.5	6.7	7700	373	5.77	8316	HEC
V7	-	19.9	6.7	6160	388	5.36	6653	HEC
V8	-	17.3	6.4	3590	505	4.24	3877	HEC
V9	0.09	17.1	5.9	1467	405	1.15	1584	HEC
V10	0.80	19.5	6.0	1313	390	0.70	1418	HEC
V11	1.00	19.3	5.6	806	495	1.23	870	HEC
V12	1.00	19	5.9	1079	522	2.86	1165	HEC
V13	5.00	16.5	5.6	601	454	3.03	649	HEC
V14	3.00	15.8	6.2	2486	374	3.20	2685	HEC
V15	1.26	16.3	5.9	457	505	5.40	494	LEC
V16	4.00	16.7	5.7	421	528	5.30	455	LEC
V17	3.48	16.3	6.1	592	527	4.24	639	LEC
V18	0.69	15.2	6.5	353	550	8.69	381	LEC
V19	0.06	15.2	6.7	260	474	6.60	281	LEC
V20	46.00	15.8	7.0	321	420	9.09	347	LEC
V21	55.00	14.4	6.1	287	507	8.23	310	LEC
V22	78.00	13.5	5.8	269	512	7.62	291	LEC
V23	8.00	18.8	6.8	395	471	3.75	427	HEC
V24	33.00	17.3	6.6	510	520	8.06	551	LEC
V25	44.00	14.8	6.6	331	503	7.43	357	LEC
V26	8.00	16.2	6.5	428	522	7.84	462	LEC
V27	5.00	21.7	5.9	1840	244	0.74	1987	HEC
V28	1.50	19	5.8	1240	459	1.26	1339	HEC
V29	2.50	21.8	5.9	1503	472	0.55	1623	HEC
V30	39.00	14.9	6.2	403	456	8.52	435	LEC
V31	6.00	13.2	7.2	224	606	8.55	242	LEC
V32	10.00	15.9	7.0	283	599	9.20	306	LEC
V33	6.00	14.7	7.0	302	819	8.32	326	LEC
V34	8.00	15.7	7.1	315	709	8.19	340	LEC
V35	4	16.7	5.7	421	528	5.30	455	LEC
V36	0.1	14.3	7.2	700	526	5.50	756	LEC
V37	0.43	19.3	6.1	2750	307	0.48	2970	HEC

The Mt. Vulture groundwater shows large fluctuations in the physico–chemical parameters, according to the complex geological context of the studied area. The physico parameters are shown in Table 5 and Fig. 34.

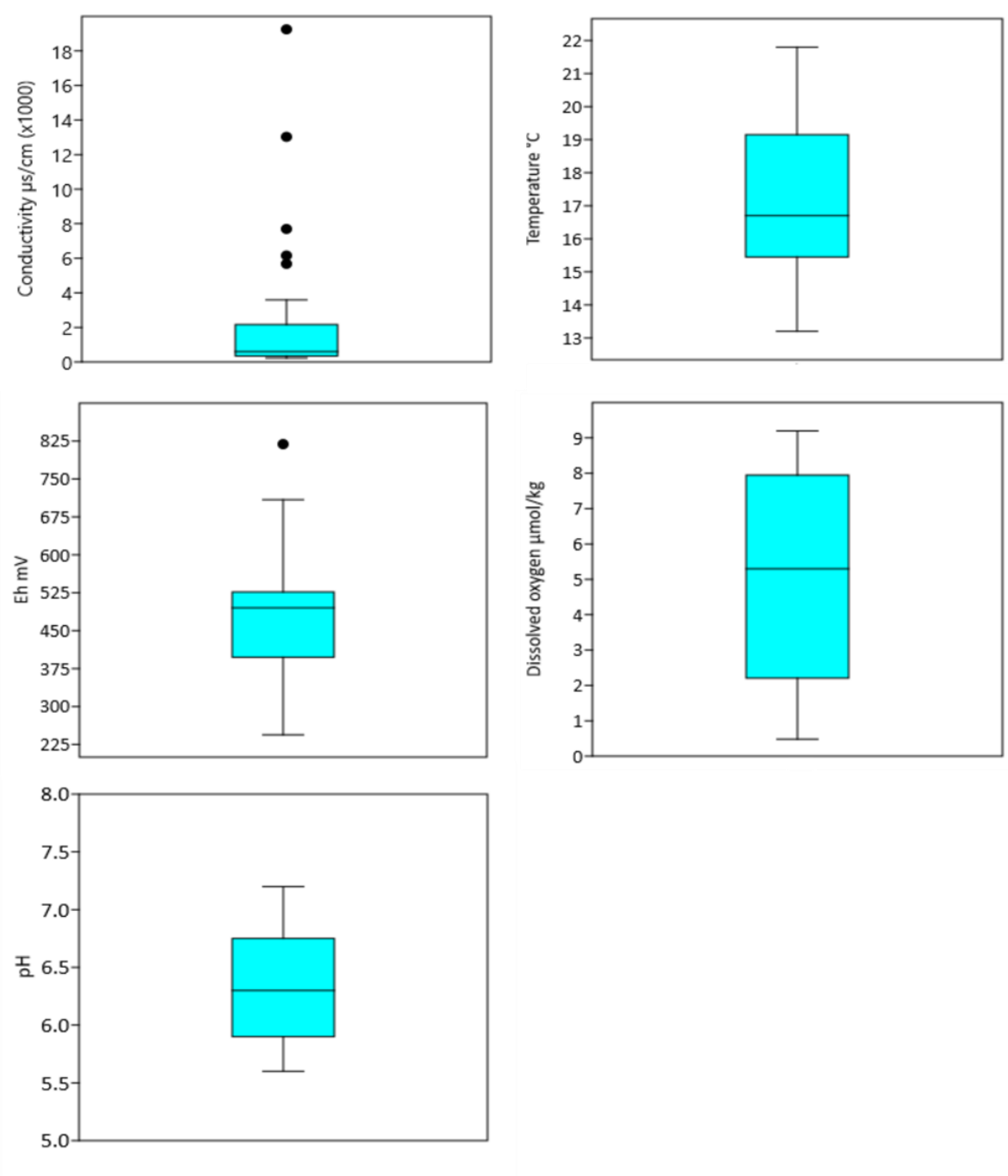

Figure 34 *- Box and wisker plots of physico-chemical parameters of groundwater samples.*

The temperature ranges from a minimum of 13.2 °C to a maximum of 21.8 °C. The water samples can be classified as cold water and slightly thermal waters, when the temperature values showed values higher (21.8 °C) than the mean measured values (17.2 °C). The term "slightly thermal water" was introduced by Nathenson *et al*., (2003) for springs that do not meet the numerical criterion of Reed (1983) but have a temperature higher than non-thermal springs and usually have also dissolved constituents normally found in thermal waters.

The pH and Eh parameters also show heterogeneity in the measured values. pH ranges from slightly acidic to neutral (pH 5.6 – 7.2), whereas Eh range between 244 mV to 819 mV. However, conductivity and dissolved oxygen show the main fluctuations in the waters of the Vulture basin, ranging respectively between 19,250 – 224 µs/cm and 9.2 – 0.5 µmol/kg.

The mean Total Dissolved Solid (hereafter TDS) values of collected waters were estimated using the regression line equation computed by Parisi (2009) for the Mt. Vulture hydro-mineral basin

TDS = 1.08 x EC

where EC is the electrical conductivity.

The TDS values range from 242 mg L^{-1} to 20,790 mg L^{-1}. According to the Freezy and Cherry classification (1979), most of the groundwaters are freshwaters (59.5%) whereas the 35.1% of the samples are classified as brackish water type. Only two water samples (sample V1 and V2) are classified as saline water type, with very high TDS values (14,072 mg L^{-1} and 20,790 mg L^{-1}, respectively) (Table 6).

Table 6 *– classification of water samples according to the TDS values (Freeze and Cherry, 1979).*

TDS (mg L^{-1})	Classification	Sample ID	Nr. of samples	%
< 1000	Fresh water type	V5, V11, V13, V15, V16, V17, V18, V19, V20, V21, V22, V23, V24, V25, V26, V30, V31, V32, V33, V34, V35, V36	22	59.5
1000 - 10000	Brakish water type	V3, V4, V6, V7, V8, V9, V10, V12, V14, V27, V28, V29, V37	13	35.1
10000-100000	Saline water type	V1, V2	2	5.4
> 100000	Brine water type			0.0

Due to the high variability of physico-chemical parameters, a cluster analysis was performed on the water samples using the software PAST3, implemented with the algorithm paired groups (UPMGA) and similarity index Gower to identify separate groundwater subsets. The

dendrogram obtained from the analyses highlight the existence of two main subsets (Fig. 35): a high EC (HEC, average EC = 2,495 µs/cm) subset with lower pH (average = 6.12), Eh (average = 421 mV), and DO (average = 2.48 µmol/kg), and higher T (average = 18.7 °C) values; and a low EC (LEC, average EC = 382 µs/cm) characterised by higher pH (average = 6.50), Eh (average = 543 mV), and DO (average = 7.31 µmol/kg), and lower T values (average = 15.4 °C) (Table 5 and 7, and Fig. 36).

Table 7 *- Physico-chemical parameters, chemical composition, ΣREE and fractionations indexes of HEC and LEC subsets. EC = electrical conductivity, DO = dissolved oxygen, HEC = high electrical conductivity subset; LEC = low electrical conductivity.*

Subset		T	pH	EC(25°C)	Eh	DO	Sr^{2+}	Na^{+}	K^{+}	Mg^{2+}	Ca^{2+}	Cl^{-}	NO_3^{-}	SO_4^{2-}	F^{-}	HCO_3^{-}	SiO_2
		°C		µs/cm	mV	µm/kg	mg/l	mg/l	mg/l	mg/l	mg/l	mg/l	mg/l	mg/l	mg/l	mg/l	mg/l
HEC	Average	18.6	6.1	2494.7	421.4	2.5	0.6	410.7	59.0	37.0	126.3	106.3	11.5	397.8	0.8	1176.6	90.2
	Median	19.0	6.0	1503.0	454.0	2.4	0.5	162.6	49.0	28.5	112.2	35.7	10.4	169.5	0.7	1079.7	97.8
	St.dev.	1.7	0.4	2136.3	82.9	1.7	0.4	500.4	39.2	25.9	58.4	140.7	10.7	528.4	0.6	731.7	15.2
LEC	Average	15.4	6.5	382.1	545.1	7.3	0.2	31.7	17.7	8.0	30.1	16.2	11.3	15.1	0.5	198.5	71.5
	Median	15.5	6.6	342.0	524.0	8.0	0.2	30.4	16.1	6.2	24.0	14.4	7.7	12.4	0.4	158.6	69.7
	St.dev.	1.1	0.5	124.2	92.5	1.5	0.1	8.3	6.8	5.6	16.4	5.2	9.0	8.6	0.3	92.0	22.0

Samples V1 and V2 do not fall into either group based on the anomalous conductivity values measured (13,030 and 19,250 µS/cm, respectively), although the T, pH, Eh and DO values fall within the range of values measured for the HEC subset (Table 5).

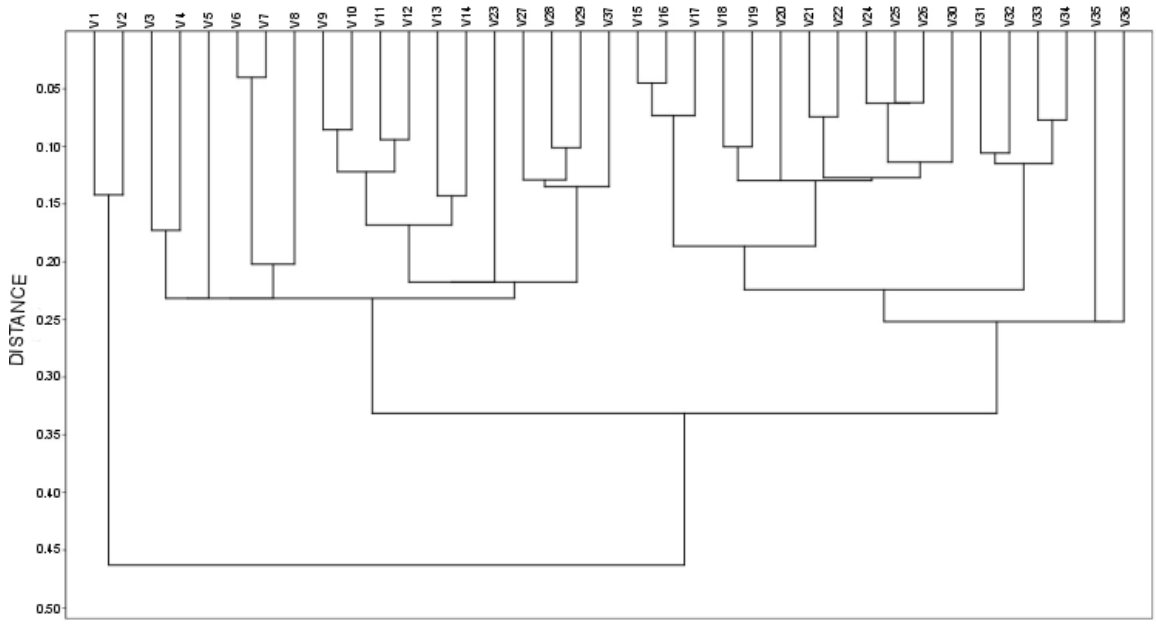

Figure 35 *- Dendrogram resulting from cluster analysis performed with the software PAST3 implemented with the algorithm paired groups (UPMGA), similarity index GOWER.*

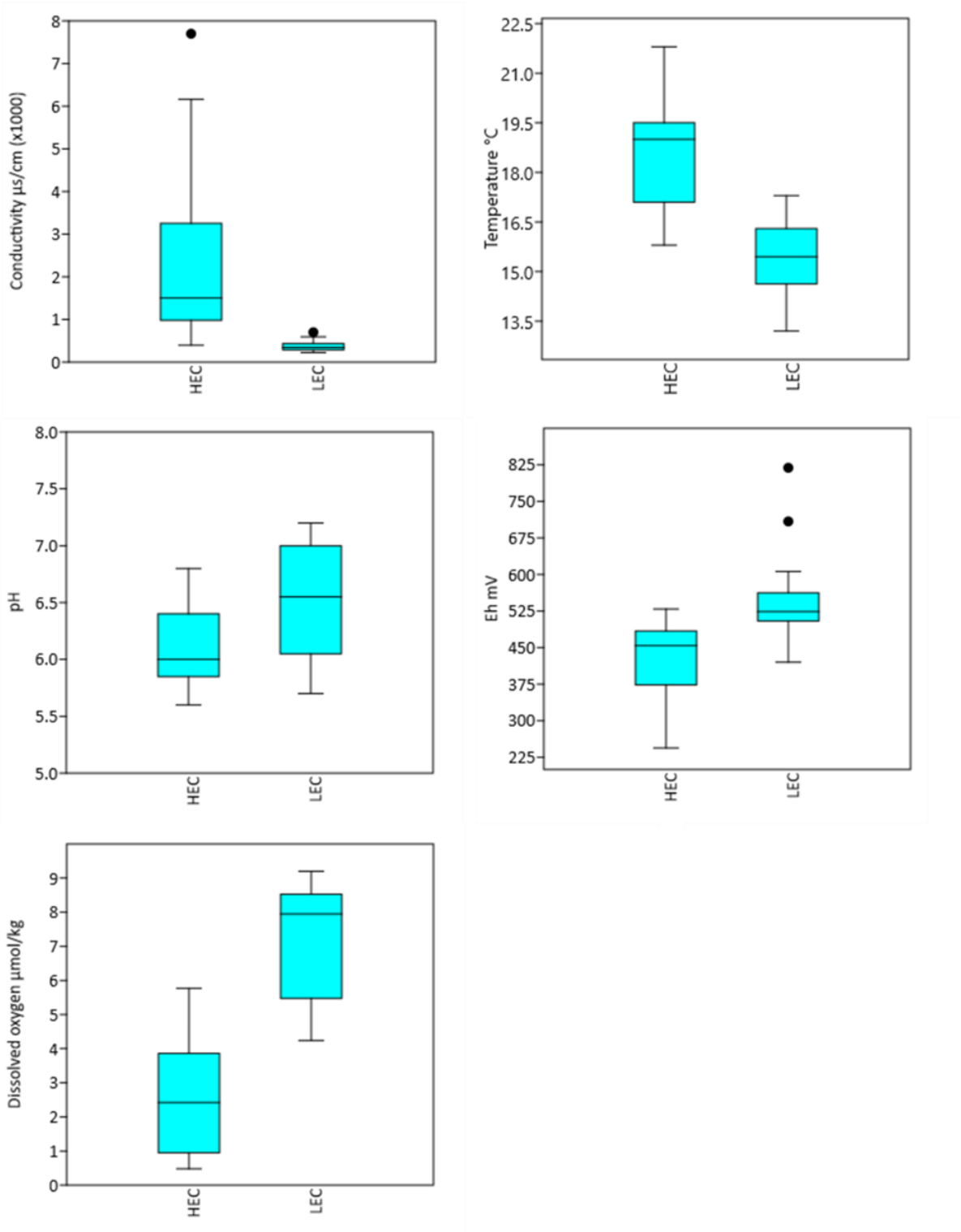

Figure 36 *- Box and wisker plots of physico-chemical parameters of HEC and LEC subsets. HEC = high electrical conductivity, LEC = low electrical conductivity.*

Table 8 *- Chemical composition of water sample. D.L. = detection limit, bdl = below detection limit, HEC = high electrical conductivity, LEC = low electrical conductivity.*

SAMPLE	Sr^{2+}	Na^{+}	K^{+}	Mg^{2+}	Ca^{2+}	Cl^{-}	NO_3^{-}	SO_4^{2-}	F^{-}	HCO_3^{-}	SiO_2	Error	Subset
	mg/l	mg/l	mg/l	mg/l	mg/l	mg/l	mg/l	mg/l	mg/l	mg/l	mg/l	%	
D.L.	0.1	0.1	0.1	0.1	0.1	0.2	0.1	0.5	0.1	0.1	0.7		
V01	bdl	2952.6	287.9	67.8	74.1	804.4	25.2	3496.9	bdl	3940.6	16.3	-4.95	-
V02	bdl	4819.6	751.4	105.8	30.4	950.2	18.5	5058.8	bdl	6197.6	21.8	1.11	-
V03	bdl	1132.8	175.0	65.5	130.4	231.5	bdl	987.9	1.3	2769.4	63.8	-4.92	HEC
V04	bdl	545.7	49.0	10.4	112.2	151.4	18.2	561.6	1.2	1067.5	81.6	-3.56	HEC
V05	bdl	92.5	23.1	12.5	77.3	21.2	10.4	70.5	1.0	402.6	89.8	3.38	HEC
V06	bdl	1633.8	106.7	19.8	167.4	480.8	13.8	1771.4	bdl	2366.8	83.4	-3.20	HEC
V07	bdl	1338.9	94.5	19.7	95.5	388.4	8.9	1394.2	2.1	2068.0	80.0	-4.94	HEC
V08	bdl	719.3	56.0	17.6	87.7	196.3	37.8	752.5	1.3	1079.7	70.6	-1.26	HEC
V09	bdl	121.5	34.6	40.8	127.1	27.8	bdl	132.4	bdl	847.9	103.8	-4.71	HEC
V10	0.6	163.5	48.1	62.7	186.5	29.8	bdl	169.5	0.3	1213.9	100.8	-3.08	HEC
V11	bdl	77.3	28.2	23.3	85.3	20.2	4.4	44.5	0.8	536.8	103.2	-0.71	HEC
V12	0.2	91.2	29.5	28.5	99.8	31.5	18.4	49.6	0.5	622.2	97.8	-1.56	HEC
V13	0.4	50.6	34.7	13.5	51.7	14.3	0.9	11.5	0.0	384.3	103.2	-1.21	HEC
V14	0.4	368.5	88.7	40.1	205.8	53.0	21.1	250.4	bdl	1592.1	63.3	-1.94	HEC
V15	0.3	41.3	24.2	10.0	39.2	18.8	bdl	16.6	0.4	286.7	96.2	-3.62	LEC
V16	0.4	42.6	31.7	11.8	39.8	26.0	7.3	11.9	0.4	292.8	103.8	-2.46	LEC
V17	bdl	39.9	24.3	22.0	55.0	25.2	3.3	38.7	0.9	359.9	87.4	-4.20	LEC
V18	0.3	31.3	15.0	6.3	23.4	15.8	15.2	35.4	0.4	134.2	69.0	-3.02	LEC
V19	0.3	25.2	7.6	4.8	18.7	10.9	2.2	11.2	0.5	133.8	57.4	-3.17	LEC
V20	0.1	24.7	15.2	6.1	18.5	10.5	31.5	12.7	1.5	122.0	70.0	-4.21	LEC
V21	0.1	27.8	20.0	4.2	16.3	11.4	14.3	8.6	0.2	140.3	86.8	-2.69	LEC
V22	0.2	24.6	17.7	4.4	18.3	15.5	13.4	8.2	0.3	122.0	85.4	-0.62	LEC
V23	bdl	33.7	15.8	7.0	27.0	22.0	12.1	16.8	0.2	176.9	76.4	-3.53	HEC
V24	0.0	43.5	18.1	2.9	30.7	14.3	4.5	18.5	0.7	207.4	80.6	-4.85	LEC
V25	0.1	29.5	13.1	5.4	22.3	14.2	7.7	15.4	0.2	158.6	69.1	-4.16	LEC
V26	0.2	31.3	14.4	10.2	33.9	22.0	31.3	13.7	0.4	170.8	69.4	0.42	LEC
V27	0.7	162.6	51.6	70.0	177.0	35.7	1.0	184.8	0.3	1213.9	105.0	-3.70	HEC
V28	bdl	77.9	42.7	38.4	102.3	27.0	0.7	29.4	0.2	756.4	103.6	-3.94	HEC
V29	1.3	120.9	61.5	64.1	162.2	37.3	1.1	103.5	0.7	1104.1	107.8	-2.70	HEC
V30	0.1	32.6	19.1	8.1	28.4	12.7	20.4	11.9	0.5	176.9	83.4	1.75	LEC
V31	0.2	18.9	15.4	2.6	12.2	12.0	6.3	6.8	0.2	97.6	43.2	-3.43	LEC
V32	0.1	21.1	13.5	6.3	24.6	13.8	9.8	9.6	0.2	152.5	54.4	-4.04	LEC
V33	0.4	27.2	16.8	4.3	18.5	12.6	1.8	14.1	0.5	146.4	57.5	-3.44	LEC
V34	0.1	23.7	14.3	5.9	22.8	14.4	6.0	9.3	0.3	158.6	53.1	-4.61	LEC
V35	0.4	42.7	31.6	11.7	39.9	26.1	7.3	12.0	0.4	292.3	103.0	-2.47	LEC
V36	0.1	41.9	6.6	19.2	79.6	15.6	9.3	17.5	0.3	420.9	18.0	-2.12	LEC
V37	bdl	251.9	62.7	95.7	251.3	38.9	bdl	232.0	bdl	1799.5	98.6	-3.55	HEC

The waters belonging to the two groups, classified through the piper diagram, also show differences in chemical composition (Table 8). The LEC waters have a bicarbonate alkaline-earth and alkaline composition, whereas the HEC waters have both a bicarbonate alkaline-earth and sulphate-bicarbonate alkaline compositions. Finally, samples V1 and V2 have a bicarbonate-sulphate-alkaline composition (Fig.37).

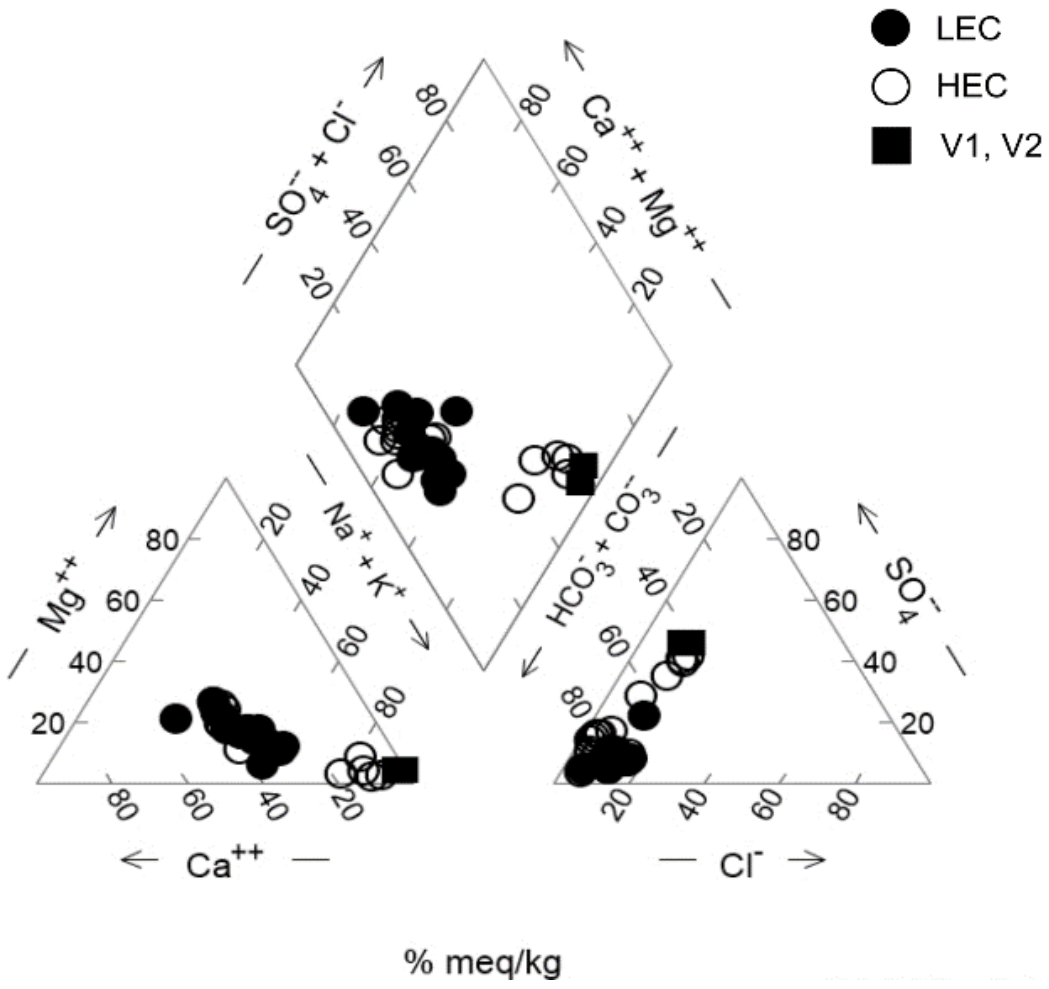

Figure 37 *- Piper diagram. HEC = High electrical conductivity, LEC = Low electrical conductivity*

Generally, the bicarbonate represents the major dissolved anion and shows a good correlation with the TDS (R^2 = 0.95), which shows positive correlation also with Na^+ (R^2=0.99), K^+ (R^2=0.89), Cl^- (R^2=0.96), and SO_4^{2-} (R^2=0.98) (Fig.38).

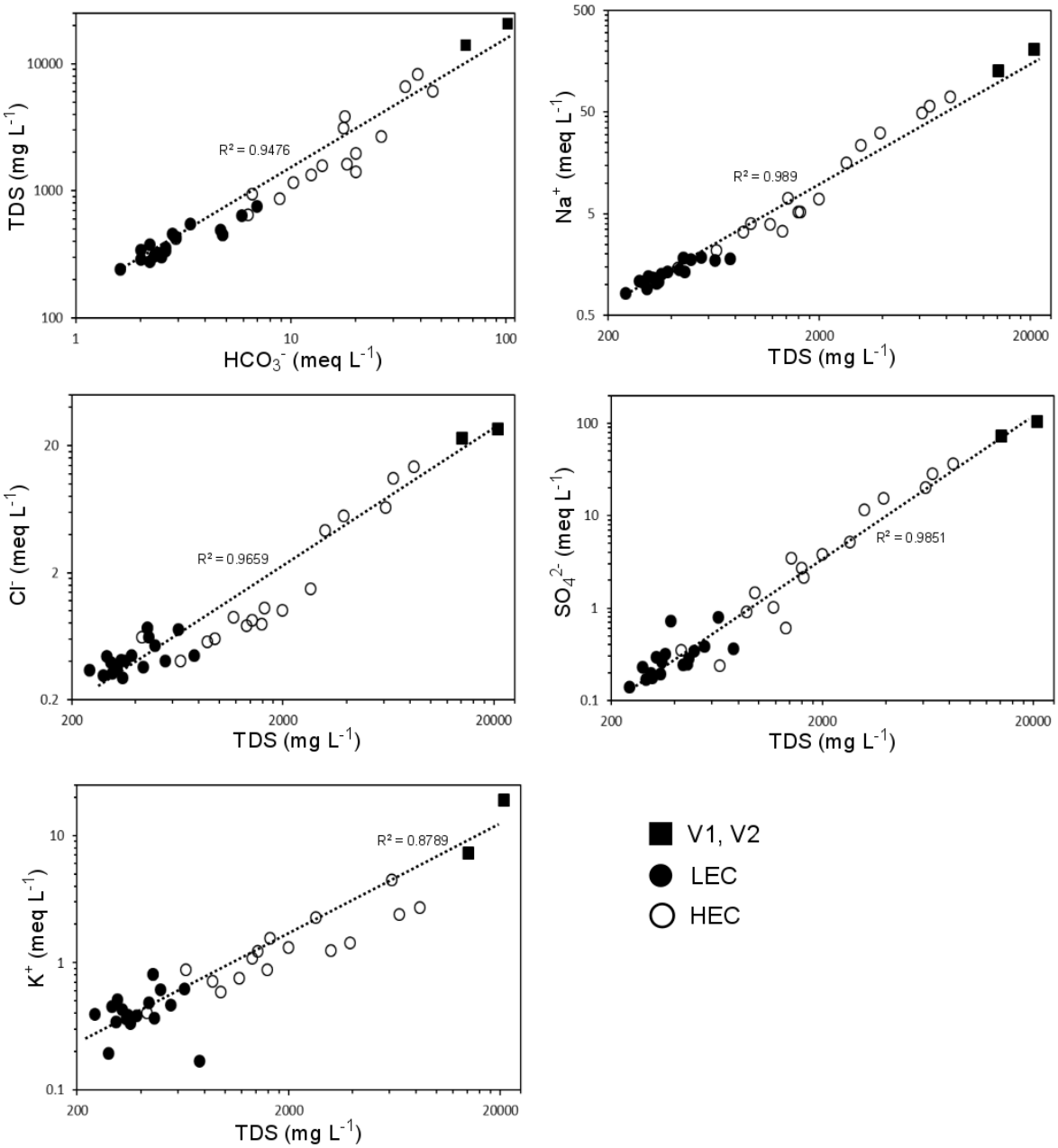

Figure 38 *- Plot correlation between HCO_3^- vs. TDS; Na^+ vs. TDS; K^+ vs. TDS; Cl^- vs. TDS and SO_4^{2-} vs. TDS. LEC = low electrical conductivity, HEC = high electrical conductivity*

Moreover, in the HEC subset, the Na^+ and HCO_3^- are significantly higher (Na^+ average = 410.7 mg/l, HCO_3^- average = 1176.6 mg/l) than in the LEC subset (Na^+ average = 31.7 mg/l, HCO_3^- average = 198.6 mg/l) (Fig.39 and Table 7 and 8). That suggests that the HEC and LEC waters correspond roughly to the waters from the discharge zone and recharge zone, respectively.

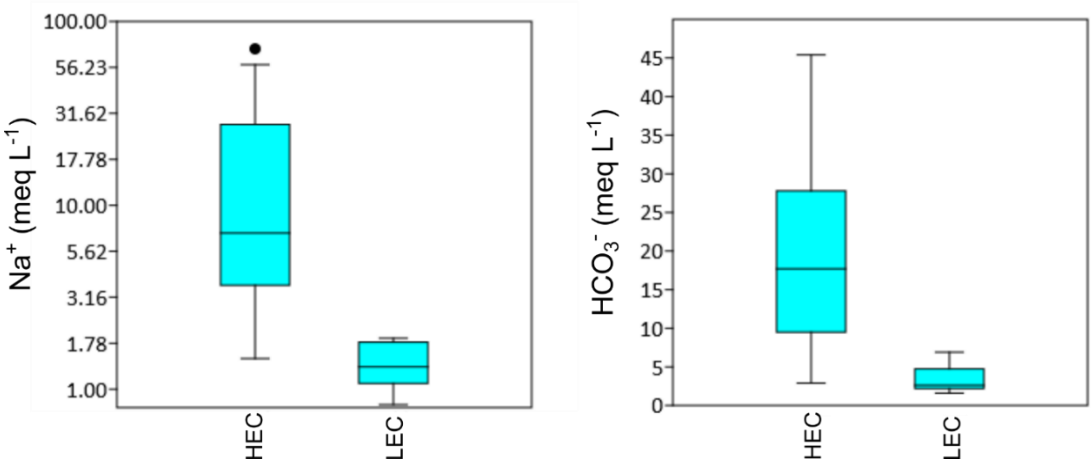

Figure 39 *- Box and wisker plots of Na^+ and HCO_3^- detected in HEC and LEC subsets. HEC = high electrical conductivity, LEC = low electrical conductivity, + = average.*

More generally, the observed differences between the two subsets are consistent with the conceptual hydrogeological model of Parisi et al. (2011a) because they are related to the aquifer radial symmetry and indicate lower solute contents in the recharge zone; furthermore, W-NW and S-SE flow directions are clearly recognised (Fig.40). The two flow paths are characterised by an increase in EC and Na^+ and HCO_3^- content and a decrease in Eh and DO contents along the flow directions (Fig.41).

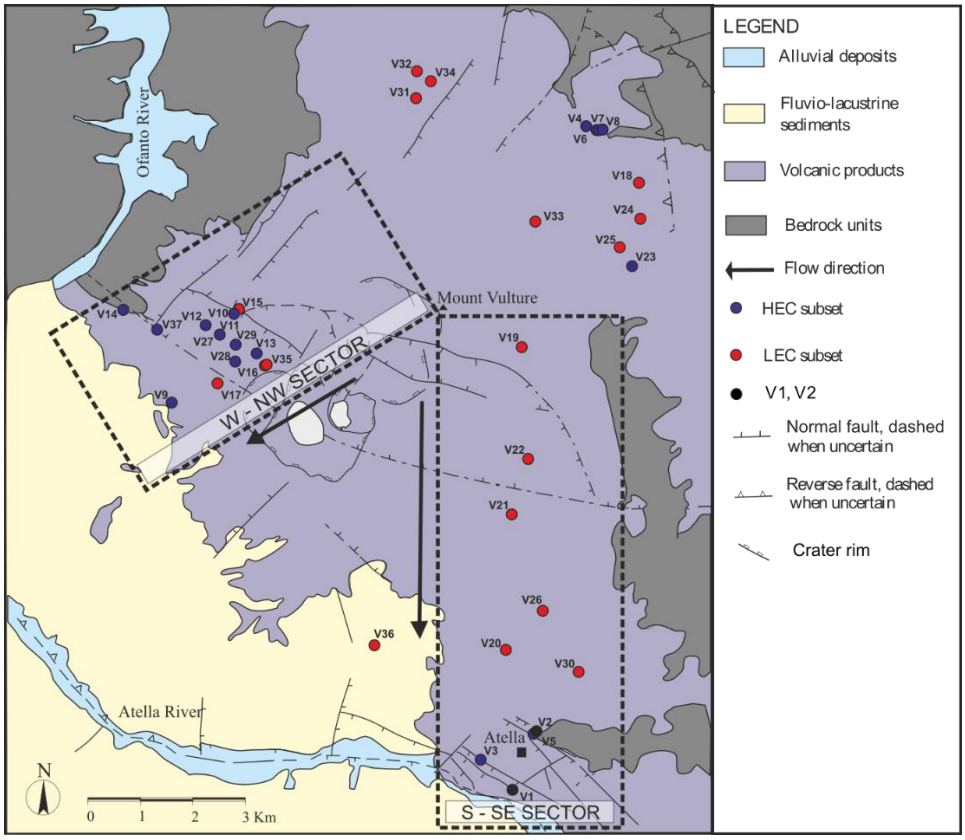

Figure 40 *- Geological sketch map of Mt. Vulture (modified from Giannandrea et al., 2004). The localization of sampling site (red, blue and black circle), flow direction and code of water sample are shown.*

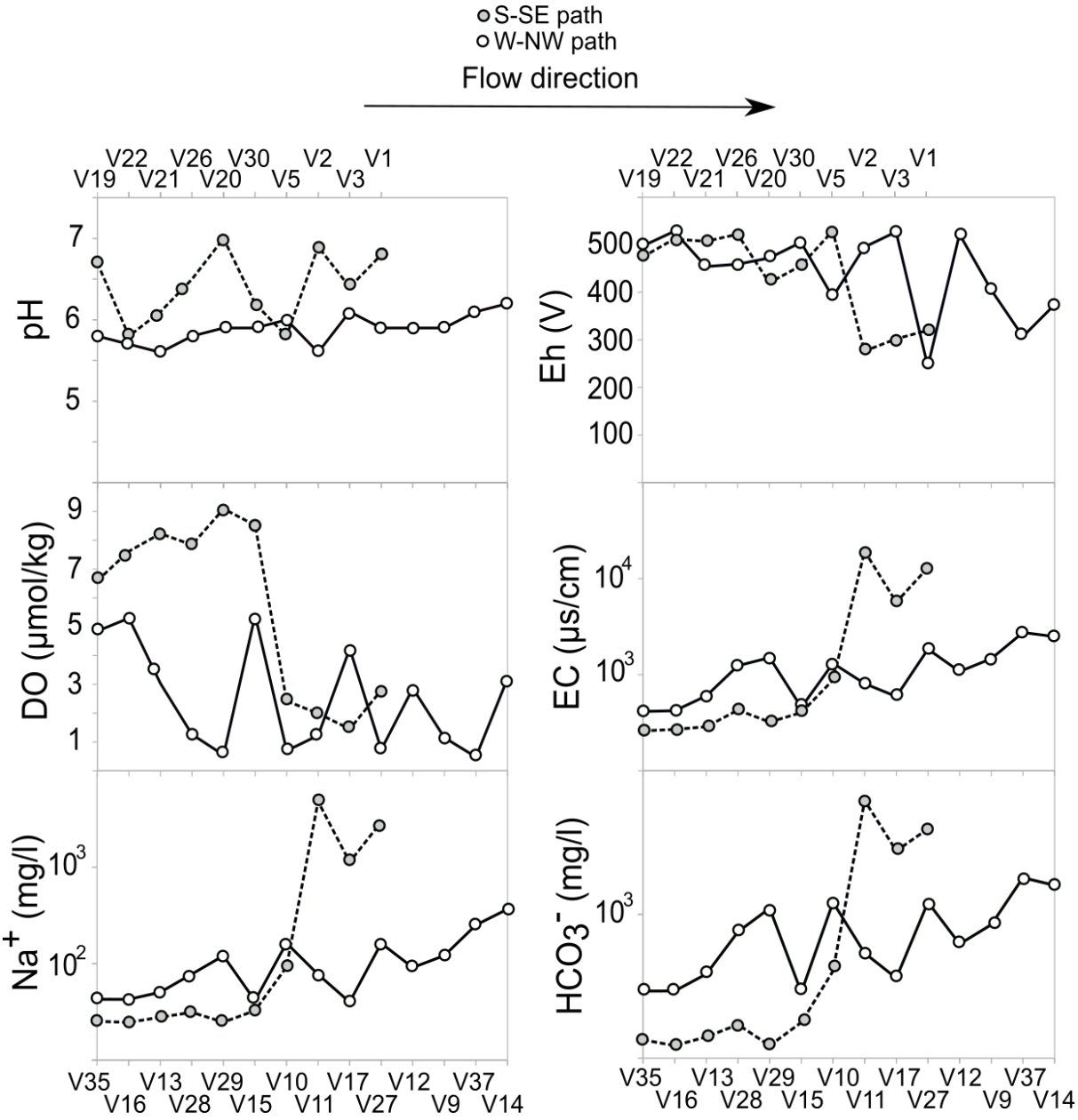

Figure 41 *- Variation of physico-chemical values, of Na^+ and HCO_3^- along the S-SE and W-NW paths.*

9.2 REEs' distribution and fractionation indexes in groundwater

Measured concentrations of REE in Mt. Vulture's groundwater are summarized in Fig. 42. Moreover, the REEs' concentrations and related log-transformed fractionation indexes normalised with respect to an average shale standard (Post Archean Australian Shales, PAAS, Taylor and McLennan, 1985), including ratios of LREE to HREE ($(La/Yb)_{PAAS}$), Ce anomaly (Ce^*_{PAAS}), and the Eu anomaly (Eu^*_{PAAS}), for the two separate groundwater subsets are presented in Table 9 and Table 10. The PAAS normalised patterns are shown in Fig. 44.

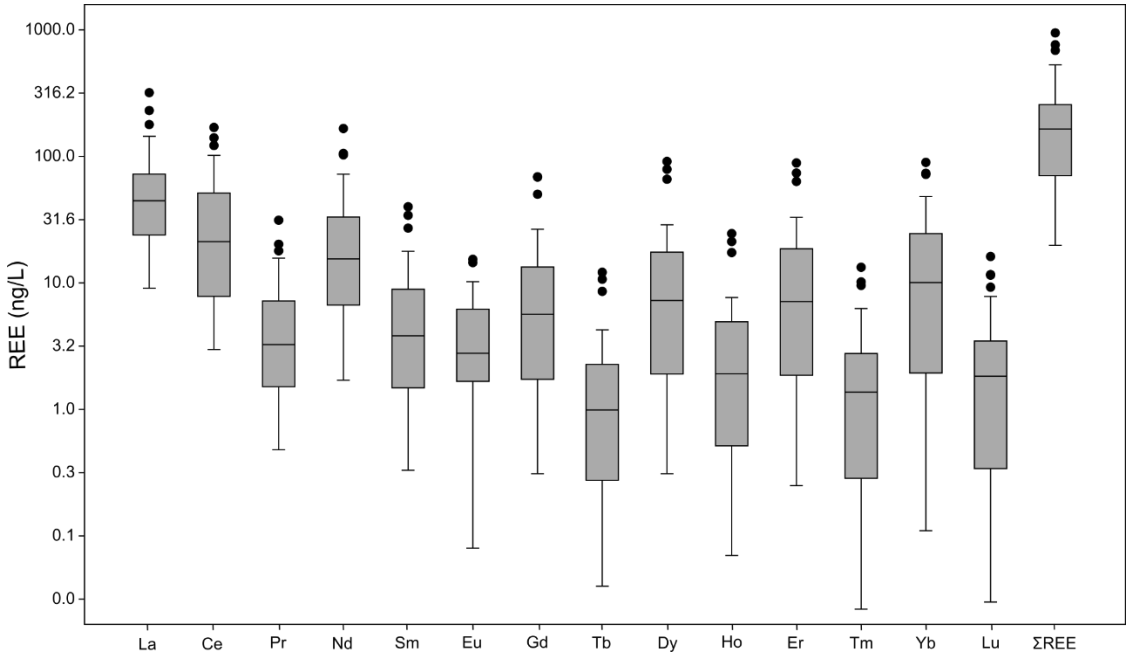

***Figure 42**– REE concentration distribution in groundwater samples.*

The concentration of total dissolved REEs (ΣREEs) in water samples fluctuates over several orders of magnitude whereas individual elements fluctuate with atomic number (i.e., the observed "zigzag pattern") (Fig.42). This fluctuation of abundance is attributable to the Oddo−Harkins rule, which asserts that, other than hydrogen, elements with even atomic numbers are more abundant than adjacent elements having odd atomic numbers (Harkins, 1917). This fluctuation gives rise to the common practice of normalizing REE data to a reference standard, for example an average shale or chondritic meteorite, that also exhibits the Oddo−Harkins effect (McLennan, 1994).

Table 9 *- REEs concentrations and fractionation indexes of water samples. HEC = high electrical conductivity subset, LEC = low electrical conductivity, LOD = limit of detection, LOQ = limit of quantification. logEu*Paas = log(Eu (Paas)/√Sm(Paas) × Gd (Paas)), logCe*Paas = log(Ce (Paas)/ √La (Paas) × Pr (Paas))* .

Sample	La	Ce	Pr	Nd	Sm	Eu	Gd	Tb	Dy	Ho	Er	Tm	Yb	Lu	ΣREE	$log(La/Yb)_{Paas}$	$logCe^*_{Paas}$	$logEu^*_{Paas}$	Subset
	ng/l	ng/l	ng/l	ng/l	ng/l	ng/l	ng/l	ng/l	ng/l	ng/l	ng/l	ng/l	ng/l	ng/l	ng/l				
LOD	**0.038**	**0.083**	**0.009**	**0.034**	**0.014**	**0.017**	**0.014**	**0.006**	**0.010**	**0.003**	**0.009**	**0.002**	**0.104**	**0.001**					
LOQ	**1.209**	**2.199**	**0.238**	**1.245**	**0.328**	**0.190**	**0.499**	**0.329**	**0.377**	**0.076**	**0.176**	**0.024**	**2.195**	**0.025**					
V1	319.00	101.96	9.45	34.60	8.33	2.48	8.50	1.68	11.03	3.16	11.27	2.03	13.79	2.55	529.82	0.15	-0.37	0.14	-
V2	52.38	4.19	0.50	1.85	0.90	0.08	0.31	0.04	0.32	0.07	0.25	0.02	0.11	0.03	61.03	1.35	-0.73	-0.14	-
V3	80.52	23.34	2.45	8.51	1.64	0.37	1.65	0.27	1.84	0.49	2.15	0.38	2.80	0.58	127.00	0.20	-0.42	0.03	HEC
V4	30.40	26.74	3.68	15.76	3.82	1.79	5.65	0.99	6.86	1.74	6.93	1.05	8.79	1.39	115.60	-0.60	-0.23	0.26	HEC
V5	144.13	92.77	15.70	59.12	12.03	3.77	14.75	2.23	14.26	3.30	11.43	1.68	10.68	1.93	387.77	-0.07	-0.35	0.12	HEC
V6	230.48	57.92	6.34	24.80	6.56	4.88	10.65	2.31	21.43	6.64	32.97	6.27	73.58	9.25	494.09	-0.55	-0.46	0.44	HEC
V7	40.22	77.26	4.87	19.41	4.56	0.80	7.09	1.68	15.79	5.22	28.00	5.15	48.15	7.81	266.00	-1.23	0.10	-0.18	HEC
V8	29.03	11.31	1.15	4.37	1.15	0.91	1.87	0.38	3.61	1.19	5.38	0.99	8.54	1.65	71.51	-0.70	-0.34	0.47	HEC
V9	44.91	24.78	2.88	12.66	3.37	1.11	6.32	1.16	10.59	3.47	13.98	2.31	18.52	3.16	188.05	-0.79	-0.30	0.06	HEC
V10	178.53	169.34	31.30	166.11	40.00	14.47	68.62	10.69	79.12	21.23	73.88	10.18	72.08	11.51	947.06	-0.75	-0.28	0.11	HEC
V11	71.52	80.89	14.91	72.37	17.77	6.96	26.58	4.25	28.80	7.66	26.19	3.93	26.51	4.49	392.85	-0.74	-0.24	0.18	HEC
V12	30.28	33.25	5.58	29.45	8.19	4.10	16.09	2.69	20.88	5.84	21.02	3.23	24.67	3.53	208.79	-1.01	-0.23	0.23	HEC
V13	38.09	44.64	8.04	38.75	10.45	5.76	17.85	3.02	21.57	5.98	21.39	3.31	24.17	4.16	247.18	-0.98	-0.23	0.30	HEC
V14	54.63	18.90	5.57	24.44	5.63	1.85	8.89	1.55	13.33	3.36	13.42	2.11	16.34	2.35	172.38	-0.58	-0.60	0.09	HEC
V15	56.14	10.46	2.89	15.46	3.81	2.57	5.33	0.85	6.13	1.60	6.00	0.91	6.61	1.17	119.93	0.20	0.78	-0.04	LEC
V16	15.94	19.98	4.88	30.00	9.34	7.14	15.63	2.58	17.82	4.55	16.23	2.31	15.43	2.75	164.59	0.66	1.21	0.36	LEC
V17	15.26	9.34	1.60	8.23	3.11	3.39	4.22	0.88	6.28	1.92	8.18	1.69	27.00	3.41	94.50	0.28	0.91	0.23	LEC
V18	100.21	8.55	1.98	7.87	1.79	2.96	1.95	0.28	1.97	0.56	1.89	0.25	1.91	0.31	132.46	-0.25	0.28	-0.61	LEC
V19	115.37	32.33	15.43	63.40	11.76	3.02	11.95	1.65	11.18	2.87	10.93	1.55	10.07	1.83	293.35	0.46	1.04	0.19	LEC
V20	10.23	3.95	0.91	3.63	0.79	2.10	0.71	0.10	0.69	0.15	0.50	0.07	0.59	0.09	24.51	-0.82	-0.30	-1.14	LEC
V21	60.25	33.56	10.63	45.28	8.48	2.28	8.89	1.26	7.26	1.85	6.11	0.95	7.95	1.21	195.96	0.27	0.79	-0.02	LEC
V22	44.60	22.24	5.98	26.33	8.16	7.09	8.93	1.41	7.79	1.91	7.12	1.37	36.18	1.41	180.52	0.28	0.85	0.14	LEC
V23	43.57	14.60	2.35	9.47	2.11	6.62	2.31	0.34	2.20	0.54	2.10	0.32	2.24	0.41	89.20	-0.27	0.32	-0.49	HEC
V24	44.64	6.25	1.42	5.50	1.17	1.19	1.11	0.17	1.12	0.28	0.92	0.15	0.98	0.18	65.07	0.44	-0.74	0.69	LEC
V25	73.41	12.94	3.25	13.75	3.87	3.72	4.22	0.82	4.60	1.19	3.72	0.67	3.76	0.74	130.66	0.05	-0.71	0.64	LEC
V26	64.62	4.87	1.23	5.13	1.47	1.54	1.81	0.35	2.02	0.54	1.83	0.32	1.97	0.37	88.06	0.30	-0.90	0.65	LEC
V27	88.65	140.30	20.21	102.84	27.11	10.21	50.20	8.57	66.01	17.37	63.35	9.55	72.89	11.64	688.90	-1.06	-0.12	0.11	HEC
V28	29.01	27.84	3.93	19.48	6.31	8.31	11.21	2.01	17.48	5.26	21.45	3.67	24.37	4.57	184.88	-1.14	-0.22	0.67	HEC
V29	62.95	121.91	17.92	105.49	34.19	15.35	68.98	12.13	91.18	24.54	88.77	13.29	89.66	16.16	762.52	-1.35	-0.08	0.17	HEC
V30	14.48	7.09	2.50	11.68	2.90	2.78	3.88	0.61	4.33	1.22	5.17	1.00	9.44	2.22	69.30	-1.13	-0.57	0.59	LEC
V31	22.83	18.87	2.75	9.08	1.49	2.36	1.21	0.16	0.91	0.15	0.51	0.06	0.59	0.05	61.02	0.74	-0.26	0.92	LEC
V32	11.06	4.51	0.80	3.06	0.69	2.32	0.64	0.08	0.71	0.17	0.69	0.08	0.77	0.10	25.68	0.10	-0.46	1.22	LEC
V33	9.67	3.25	0.48	1.70	0.33	2.97	0.31	0.04	0.31	0.07	0.28	0.02	0.38	0.04	19.83	0.46	-0.46	1.64	LEC
V34	9.07	2.97	0.58	2.15	0.55	2.70	0.47	0.09	0.54	0.14	0.51	0.07	0.49	0.07	20.43	0.14	-0.52	1.40	LEC
V35	13.67	21.18	4.86	31.64	10.02	6.88	15.39	2.66	17.53	4.63	15.94	2.27	16.19	2.61	165.48	-1.23	-0.22	0.42	LEC
V36	24.94	3.65	0.59	2.43	0.59	1.45	0.65	0.09	0.63	0.13	0.47	0.05	0.46	0.04	36.17	0.81	-0.66	1.05	LEC
V37	41.17	68.50	2.02	9.47	2.93	0.71	4.93	0.96	8.47	2.64	11.17	1.87	14.30	2.54	171.68	-0.74	0.24	-0.06	HEC

Each of the dissolved rare earths is present in higher concentrations in the HEC subset. Therefore, the ΣREE contents is higher in the HEC subset (average =322 ng/l) than in the LEC subset (average = 105 ng/l) (Table 10 and Fig. 43).

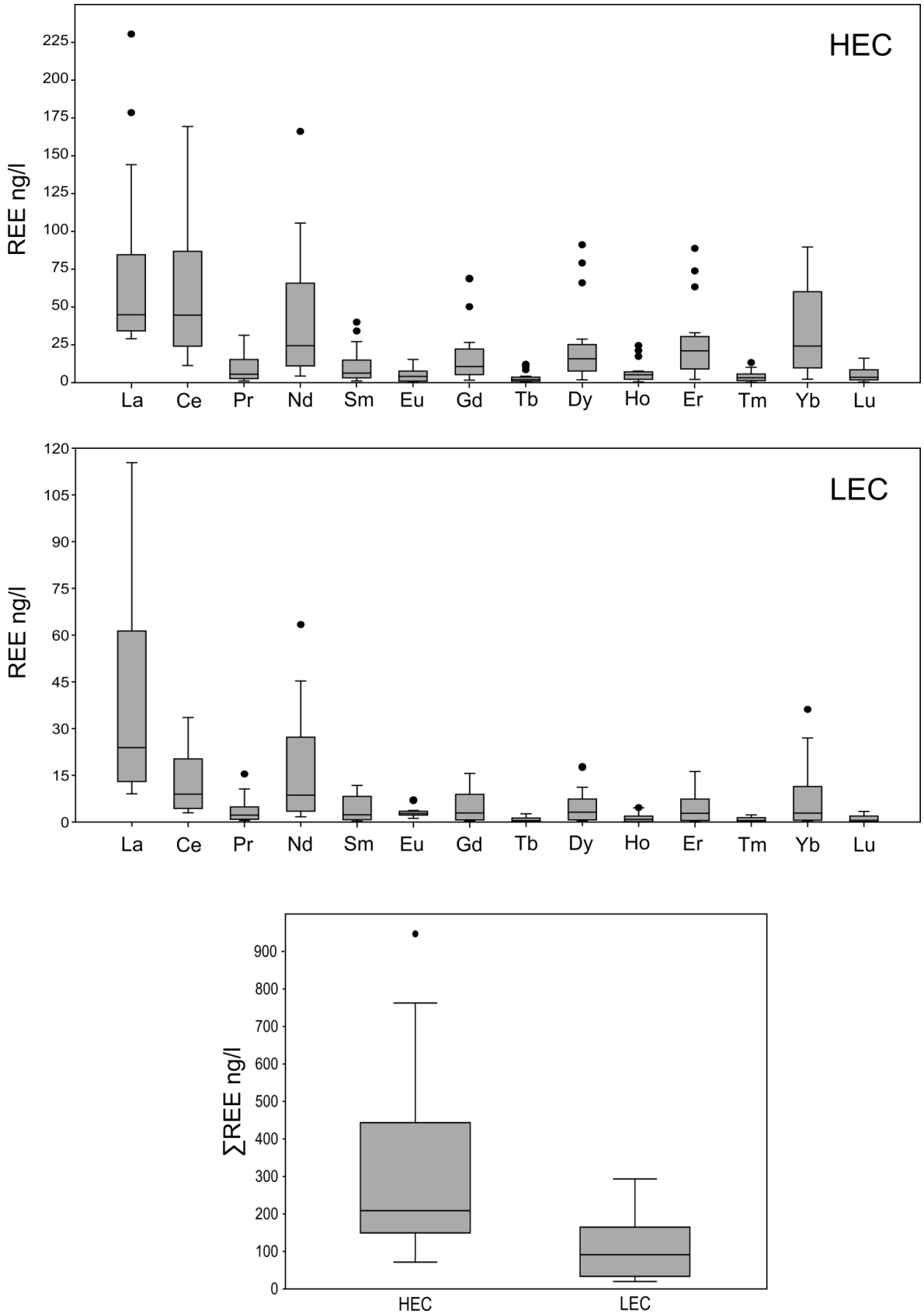

Figure 43 *– REE concentration distribution in HEC and LEC subsets. HEC = high electrical conductivity subset; LEC = low electrical conductivity.*

Table 10 *- ΣREE and fractionations indexes of HEC and LEC subsets. HEC = high electrical conductivity subset; LEC = low electrical conductivity, logEu*Paas = log(Eu (Paas)/√Sm(Paas) × Gd (Paas)), logCe*Paas = log(Ce (Paas)/ √La (Paas) × Pr (Paas)) .*

Subset		ΣREE ng/l	$log(La/Yb)_{PAAS}$	$logCe^*_{PAAS}$	$logEu^*_{PAAS}$
HEC	Average	322.2	-0.71	-0.25	0.24
	Median	208.8	-0.74	-0.24	0.17
	St.dev.	258.7	0.44	0.21	0.31
LEC	Average	104.9	-0.12	-0.56	0.75
	Median	91.3	0.07	-0.52	0.65
	St.dev.	74.9	0.69	0.20	0.42

The PAAS normalized pattern (Fig.44) shows an important fractionation between light REE (LREE) and heavy REE (HREE) (average $(La/Yb)_{PAAS}$ = -0.71) for the HEC subset. In addition, a moderate Ce^*_{PAAS} (average = -0.25) and Eu^*_{PAAS} (average = 0.24) anomalies are observed (Fig.45 and Table 10). Instead, the LEC subset shows a minor fractionation between LREE and HREE (average $(La/Yb)_{PAAS}$ = -0.12) and a less marked Ce anomaly (average Ce^*_{PAAS} = -0.56) than the HEC subset whereas the Eu anomaly is generally more important (average Eu^*_{PAAS} = 0.75) (Fig.45 and Table 10).

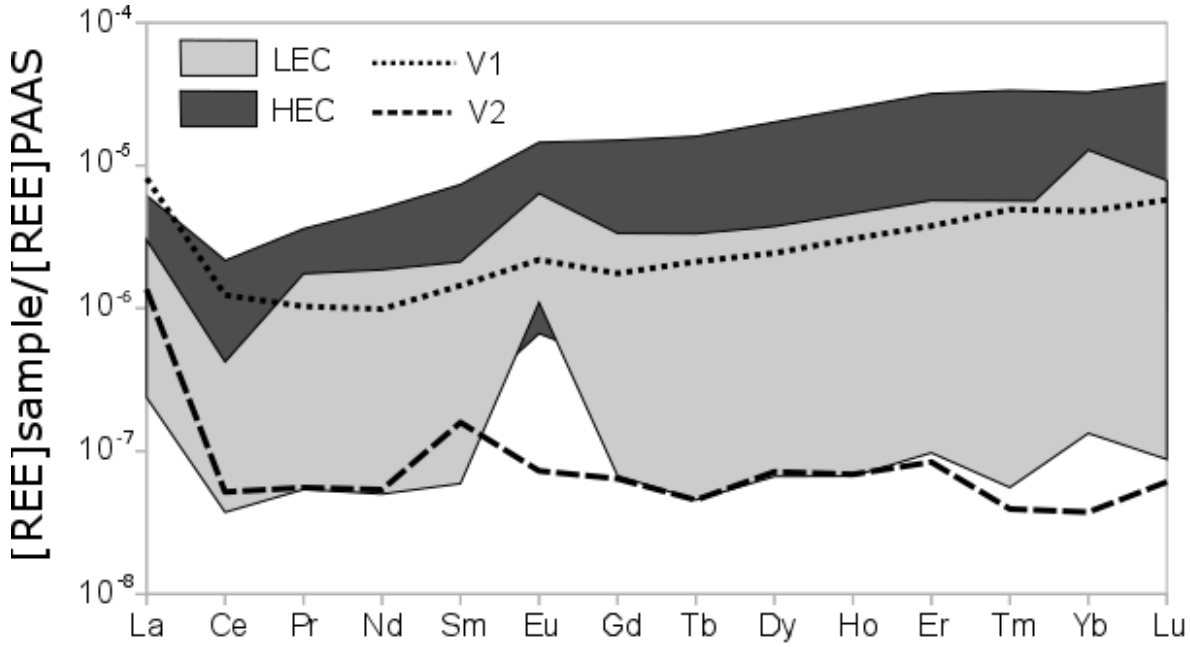

Figure 44*- REEs shale normalized pattern of V1, V2, LEC and HEC subsets. HEC = high electrical conductivity, LEC = low electrical conductivity.*

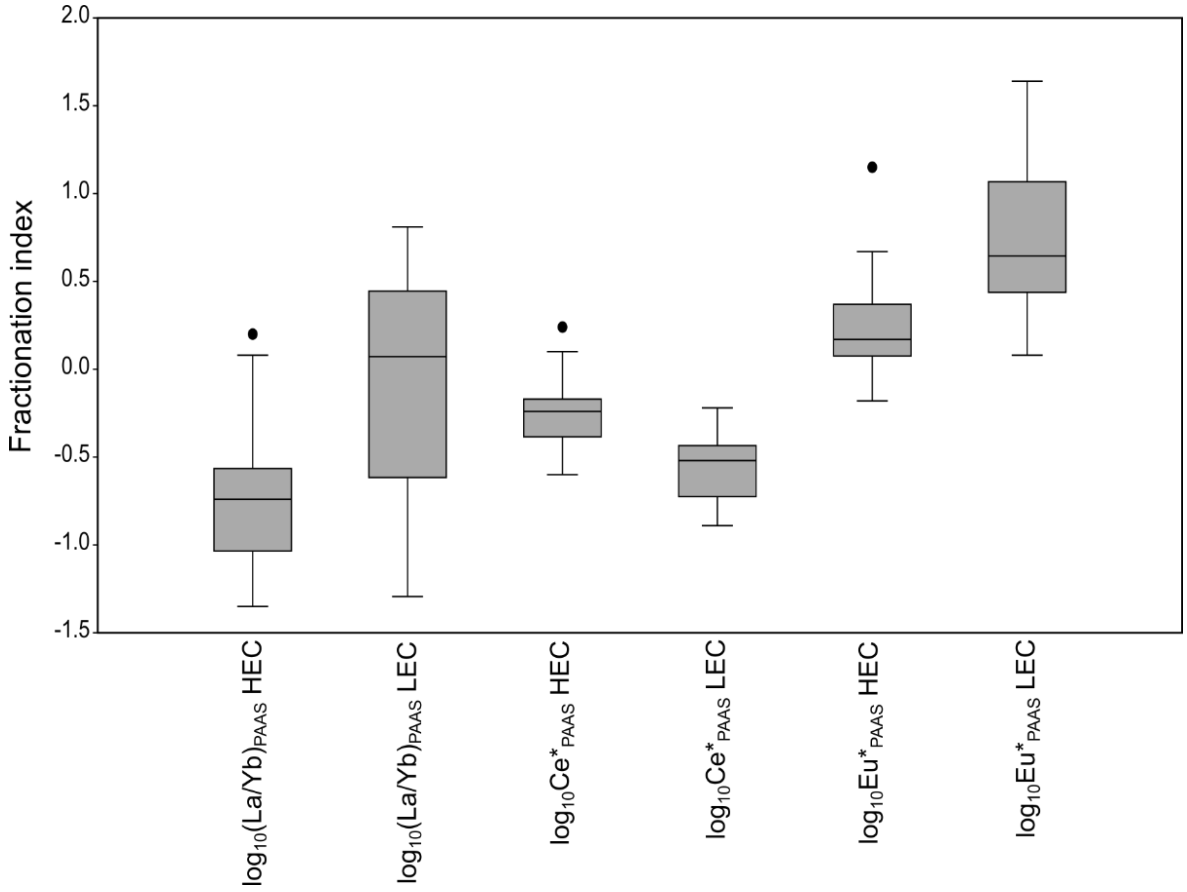

Figure 45 *- Box and wisker plots of fractionation indexes measured in HEC and LEC subsets. HEC = high electrical conductivity, LEC = low electrical conductivity.*

Cerium anomalies do not exhibit the expected negative trend with redox potential in water samples. The lack of a negative trend is probably because the mechanism is a function of both source composition and aqueous chemistry. A slight positive correlation is instead observed between Eu^*_{PAAS} and Eh; the positive trend is more evident in LEC subset (R^2=0.49) (Fig.46).

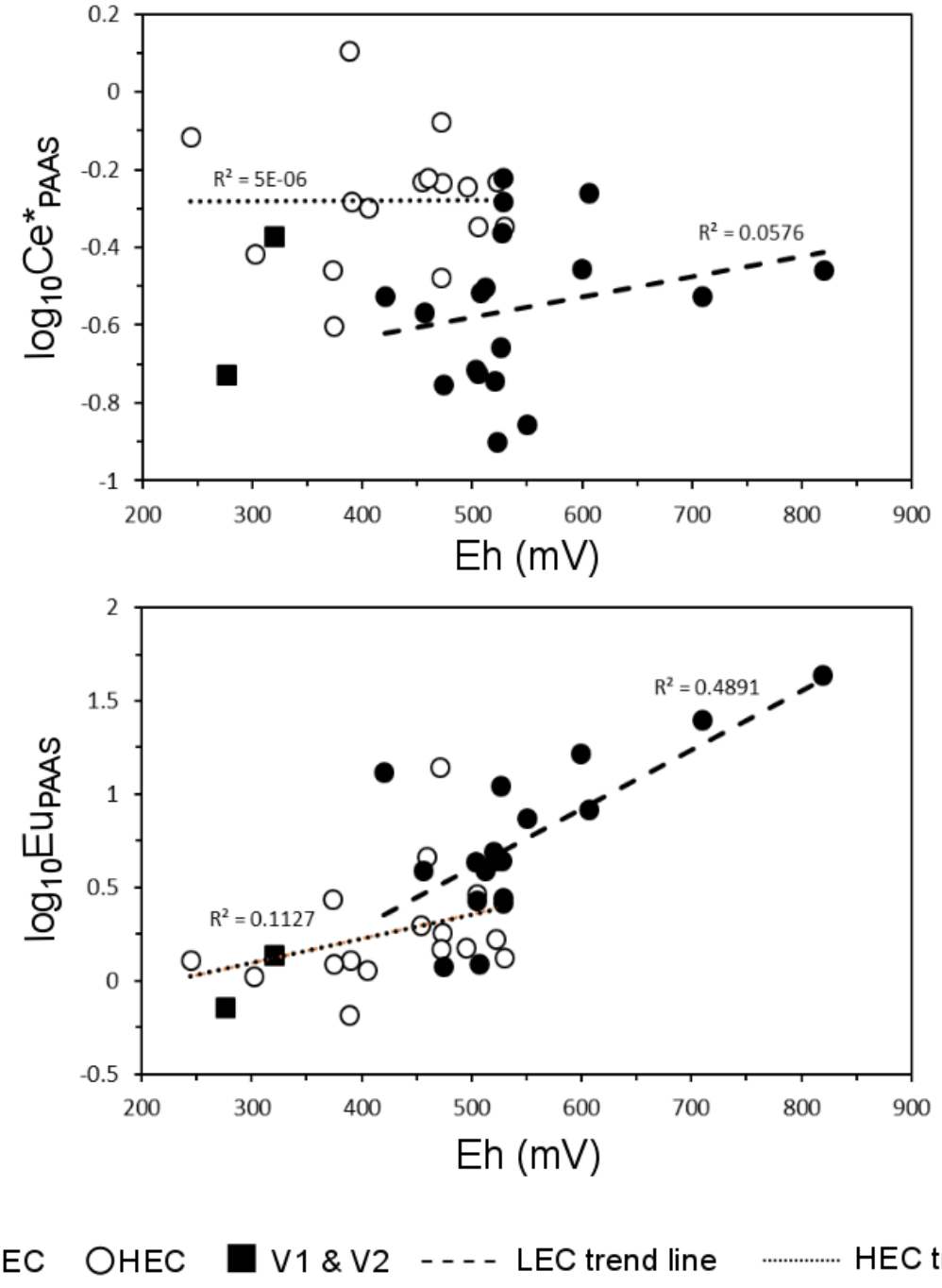

Figure 46 *-Groundwater Post-Archaean Average Shale (PAAS) Ce anomaly (Ce*) and Eu anomaly (Eu*) as a function of reported redox potential (Eh); HEC = high electrical conductivity, LEC = low electrical conductivity.*

The ΣREEs and log-transformed fractionation indexes show large fluctuations along the flow directions (see Fig. 40 and Fig.47), suggesting that local factors, such as lithological differences in the aquifer rocks, may affect the REEs' distribution. However, some rough trends can be identified, such as the $\log(La/Yb)_{PAAS}$ increase and the $\log(Eu^*_{PAAS})$ decrease toward the discharge zone in both flow paths (Fig. 47).

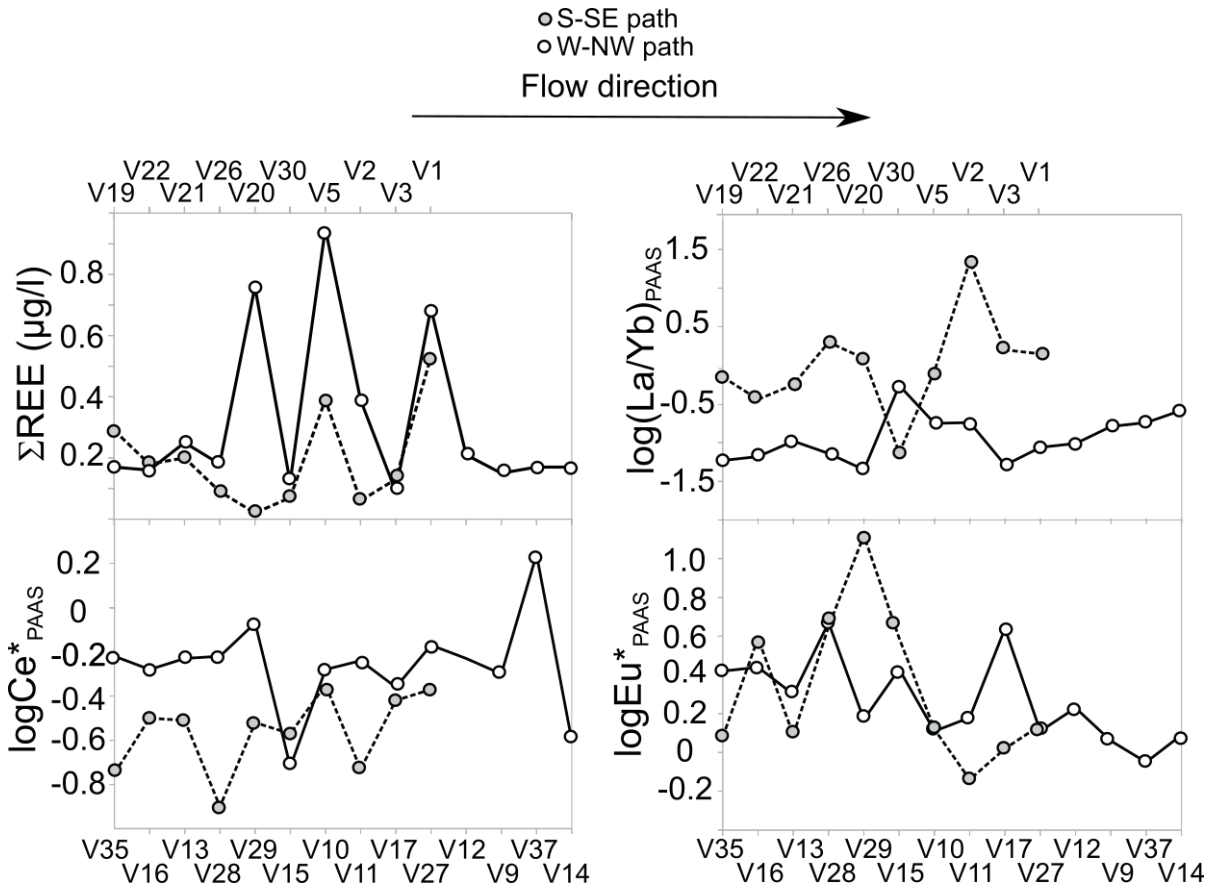

Figure 47 *- Variation of ∑REE concentrations and of REEs' fractionation indexes along the S-SE and W-NW paths.*

9.3 REEs' speciation

The results of the REE speciation are shown in Figs. 48 and 49. The model indicates that the REEs in the sulphate-bicarbonate alkaline groundwater samples (V1 and V2) are predominantly complexed with carbonate ions, including both carbonato complexes $LnCO_3^+$ and dicarbonato complexes $Ln(CO_3)_2^-$, where Ln indicates any of the 14 naturally occurring lanthanides. The importance of dicarbonato complex increases with increasing atomic number. For instance, the percentage of $Yb(CO_3)_2^-$ predicted to occur in solution is, for both the samples, well above 60% ($YbCO_3^+$ below 35%), whereas that of $La(CO_3)_2^-$ is well below 40% ($LaCO_3^+$ above 50%). The rest of the REEs in solutions are observed as $LnSO_4^+$ ($LaSO_4^+$ 9-18%, $YbSO_4^+ < 1\%$) and, at a very minor content, as Ln^{3+} ($Ln^{3+} < 3\%$).

In the LEC subset, the carbonato complexes are predicted to be largely prevailing in most of the water samples, increasing in percentage with increasing atomic number. The $LaCO_3^+$

species fluctuates in the range of 7-86% whereas $YbCO_3^+$ fluctuates in the range of 49-93%. In the V16, V22, and V35 samples, which are characterised by more acidic pH values (pH = 5.7-5.8), the LREE (La-Nd) are predicted to exist mostly as free metal ions Ln^{3+} (V16: La^{3+} = 72.8%; V22: La^{3+} = 77.6%; V35: La^{3+} = 69.5%). More generally, the importance of free metal ions in this subset, even excluding the samples V16, V22 and V35, is generally not negligible (La^{3+}: 3.3-64.4%; Yb^{3+}: 0.1-13.5%). The relevance of the dicarbonato complex, which increases with the atomic number, is associated to samples with a pH of ~7, such as V20 (pH = 7, $Yb(CO_3)_2^-$ = 8.5%), V31 (pH = 7.2, $Yb(CO_3)_2^-$ = 10.6%), V32 (pH = 7, $Yb(CO_3)_2^-$ = 10.7%), V33 (pH = 7, $Yb(CO_3)_2^-$ = 9.9%), V34 (pH = 7.1, $Yb(CO_3)_2^-$ = 14.0%), and V36 (pH = 7.2, $Yb(CO_3)_2^-$ =33.9%). The importance of the $LnSO_4^+$ species decreases with increasing atomic number ($LaSO_4^+$: 0.6-18.9%, $YbSO_4^+$: 0.1-3.5%). The LnF^{2+} species increase with increasing atomic number (LaF^{2+}: 0.1-6.9%, YbF^{2+}: 0.1-15.9%), whereas the amounts of $LnOH^{2+}$ and $LnCl^{2+}$ are always negligible.

In the HEC subset, the predicted general trends are very similar to those observed in the LEC subset. The carbonato complexes are largely prevailing in most of the samples, increasing in percentage with increasing atomic number. The $LaCO_3^+$ and $YbCO_3^+$ species fluctuate in the range of 8-76 and 44-90%, respectively. In the samples V11 and V13, which are characterised by the most acidic pH values within the subset (pH =5.6), the LREE are predicted to exist mostly as free metal ions Ln^{3+} (V11: La^{3+} = 57%, V13: La^{3+} = 79%).

The relevance of free metal ions in the HEC subset, even by excluding the samples V11 and V13, is not negligible (La^{3+} = 4-57%; Yb^{3+} = 0.4-15%). The dicarbonato complexes, which also in this case increase with the atomic number, appear to be relevant mostly in the samples having pH close to neutrality, such as V6 (pH = 6.7, $Yb(CO_3)_2^-$ = 43.4%), V7 (pH = 6.7, $Yb(CO_3)_2^-$ = 40.9%), and V23 (pH = 6.8, $Yb(CO_3)_2^-$ = 8.2%).

The importance of the $LnSO_4^+$ species decreases with increasing atomic number ($LaSO_4^+$ = 4.5-44.4%, $YbSO_4^+$ = 0.3-9.1%) whereas that of the LnF^{2+} species increases with increasing atomic number (LaF^{2+} = 0.5-8.0%, YbF^{2+} = 0.5-25.6%); both the $LnSO_4^+$ and the LnF^{2+} species can reach higher percentage values in this subset than in the LEC subset. Finally, the percentage of the $LnOH^{2+}$ and $LnCl^{2+}$ species are always negligible.

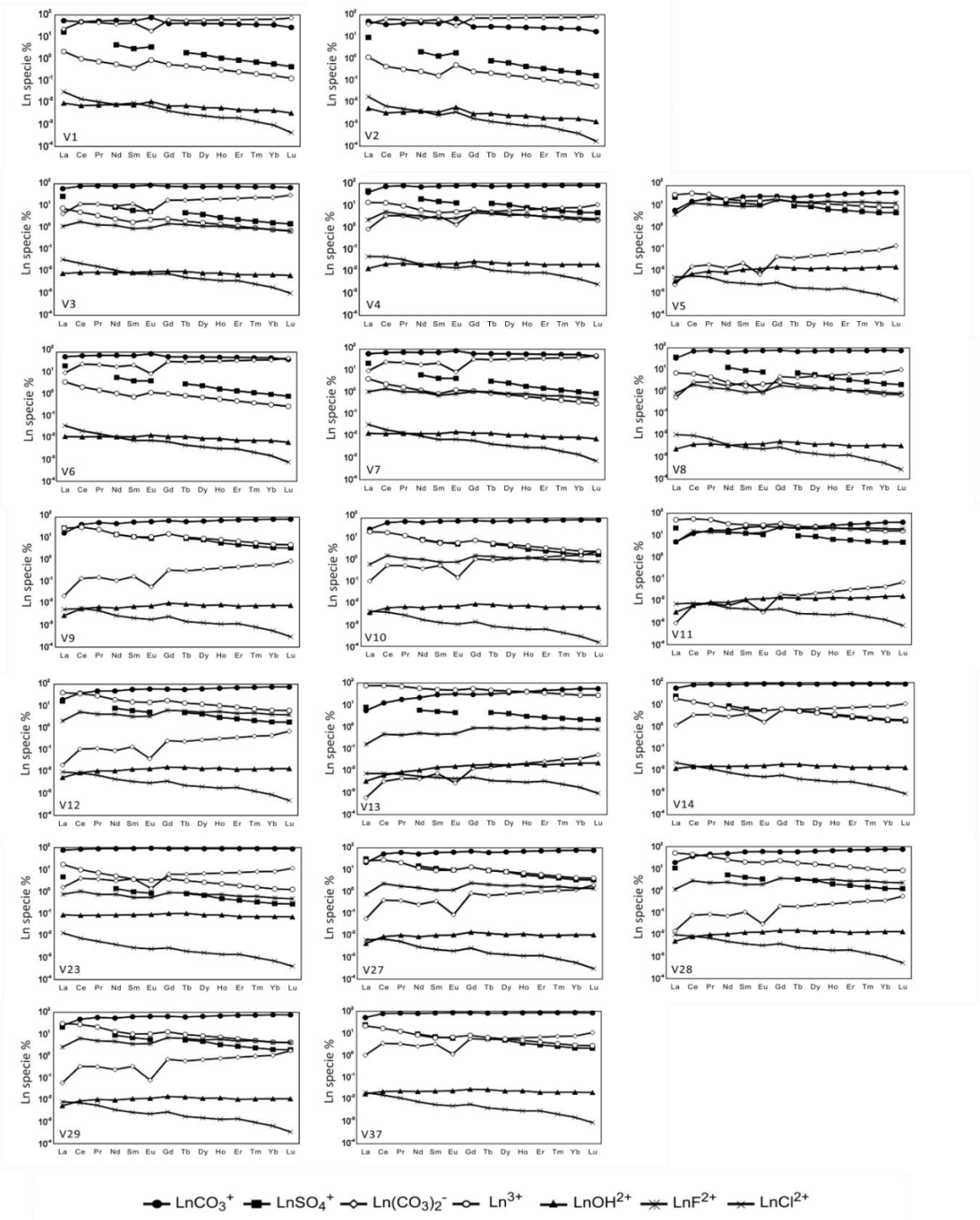

Figure 48 *- Distribution of REEs complexes dissolved in V1, V2 and HEC subset.*

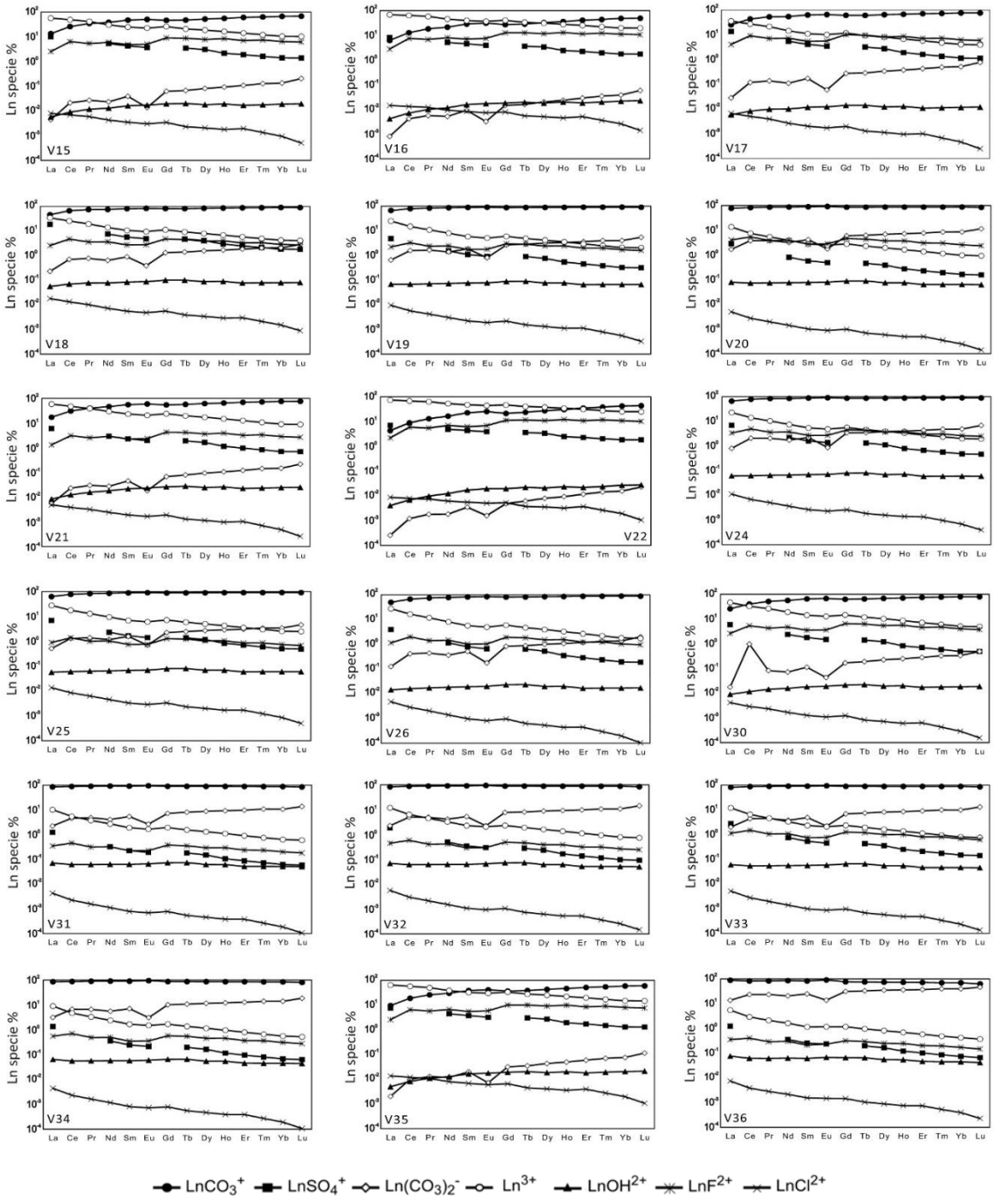

Figure 49 *- Distribution of REEs complexes dissolved in LEC subset.*

The distribution of the main Ln species ($LnCO_3^+$, $Ln(CO_3)_2^-$, Ln^{3+}, $LnSO_4^+$, LnF^{2+}) in both the S-SE and W-NW flow paths indicates that the $LnCO_3^+$ and Ln^{3+} are the prevailing species (Fig.50). In the S-SE path, the large fluctuations associated with the $LnCO_3^+$ and Ln^{3+} throughout the flow direction are related to pH variability. In the W-NW path, $LnCO_3^+$ tends to increase, and Ln^{3+} tends to decrease towards the discharge zone, and the pH tends to increase

constantly. Finally, in both the flow paths, an increase in predicted percentage of $LaSO_4^+$ species toward the discharge zone is observed.

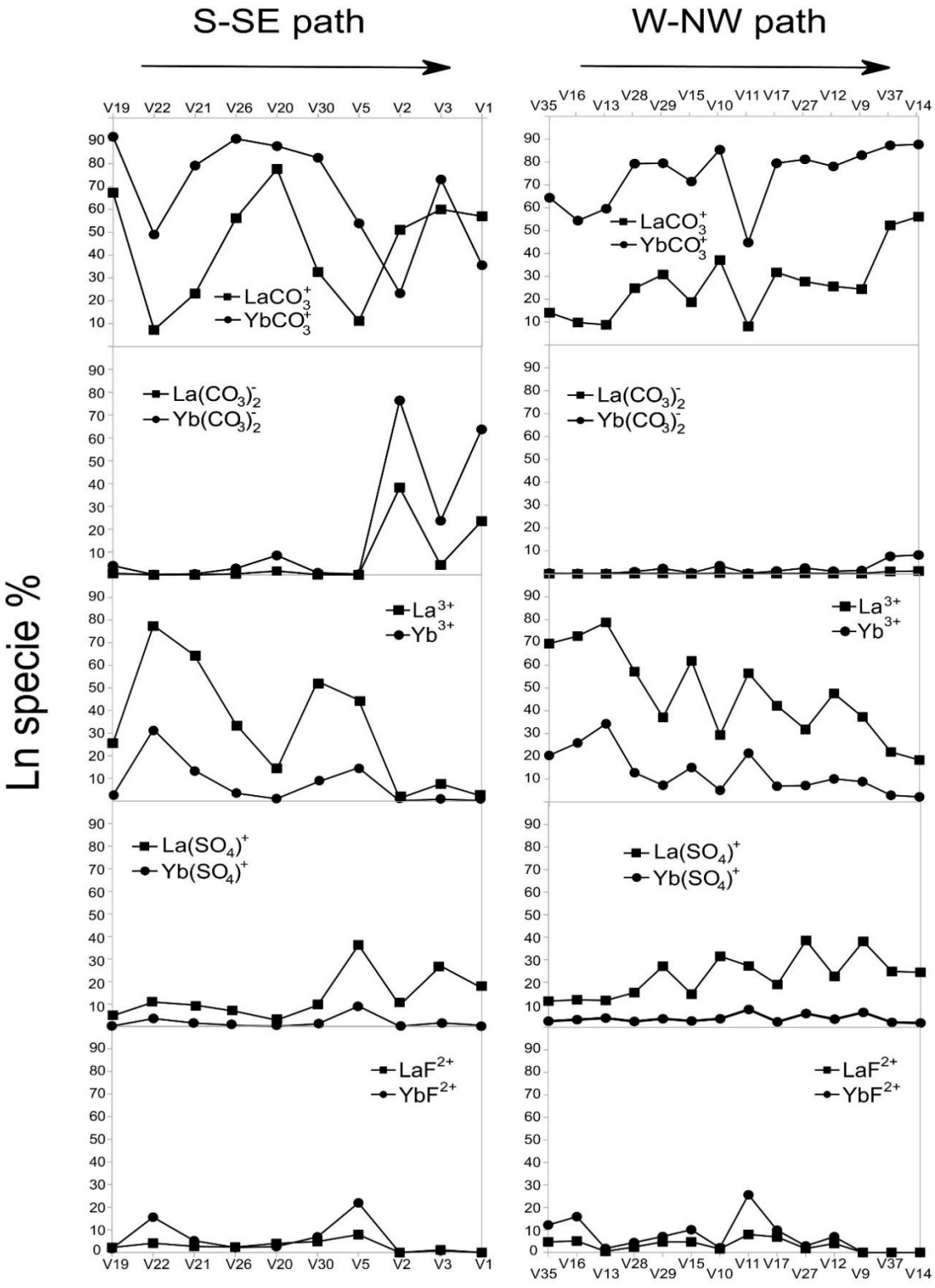

Figure 50 *- Variation of distribution of REEs complexes dissolved along the S-SE and N-NE.*

CHAPTER 10

DISCUSSION

10.1 Groundwater geochemistry and REEs' signature

In the previous chapter (Results -Groundwater physico-chemical features and major solutes) it has been shown that the groundwater in the discharge zone (HEC subset) have Na^+, Ca^{2+}, Cl^-, SO_4^{2-}, and HCO_3^- contents one order of magnitude higher than those in the recharge zone (LEC subset, Table 7). This pattern is clearly observed also along the N-NW and S-SE flow paths. Moving from the recharge zone to the discharge zone along the two flow paths, Na^+ and HCO_3^- shows very similar trends (Fig.41) suggesting that the water-volcanic rock interaction is the main factor in the groundwater chemistry. Moreover, the high SO_4^{2-} abundances associated to the sulphate-bicarbonate alkaline hydrofacies is generally linked to the leaching of feldsphatoids of the sodalite group (Paternoster et al., 2010) because the sulphur isotopic values of groundwater in the Mt. Vulture aquifer match those measured in the undersaturated alkaline volcanics (Marini et al., 1994). The availability of a significant amount of SO_4^{2-} is also at the origin of the $LnSO_4^+$ species importance in the HEC subset, especially as concerns the LREE.

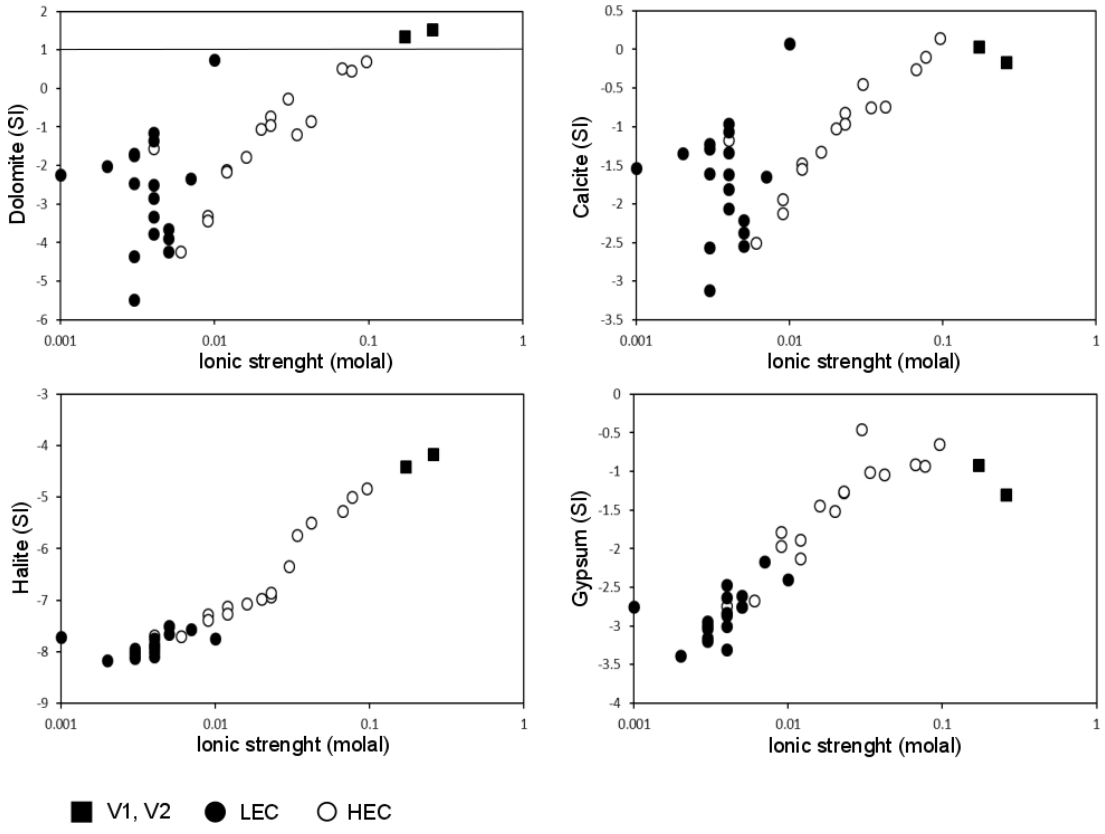

Figure 51 *– Plots of dolomite, Calcite, halite, and gypsum vs. ionic strength. LEC = low electrical conductivity, HEC = High electrical conductivity.*

However, more generally, both the subsets are largely under-saturated with calcite, gypsum, and halite (Table 11, Fig.51), suggesting limited residence times. Within this scenario, the only exceptions are in samples V1 and V2, which are oversaturated with dolomite, and some sample close to saturation with calcite (samples V1, V6, and V36) probably as a consequence of locally CO_2 supply from the depth in correspondence with main tectonic structures (Caracausi et al., 2013, 2015; Caracausi and Paternoster, 2015; Sinisi et al., 2016) (Fig.52).

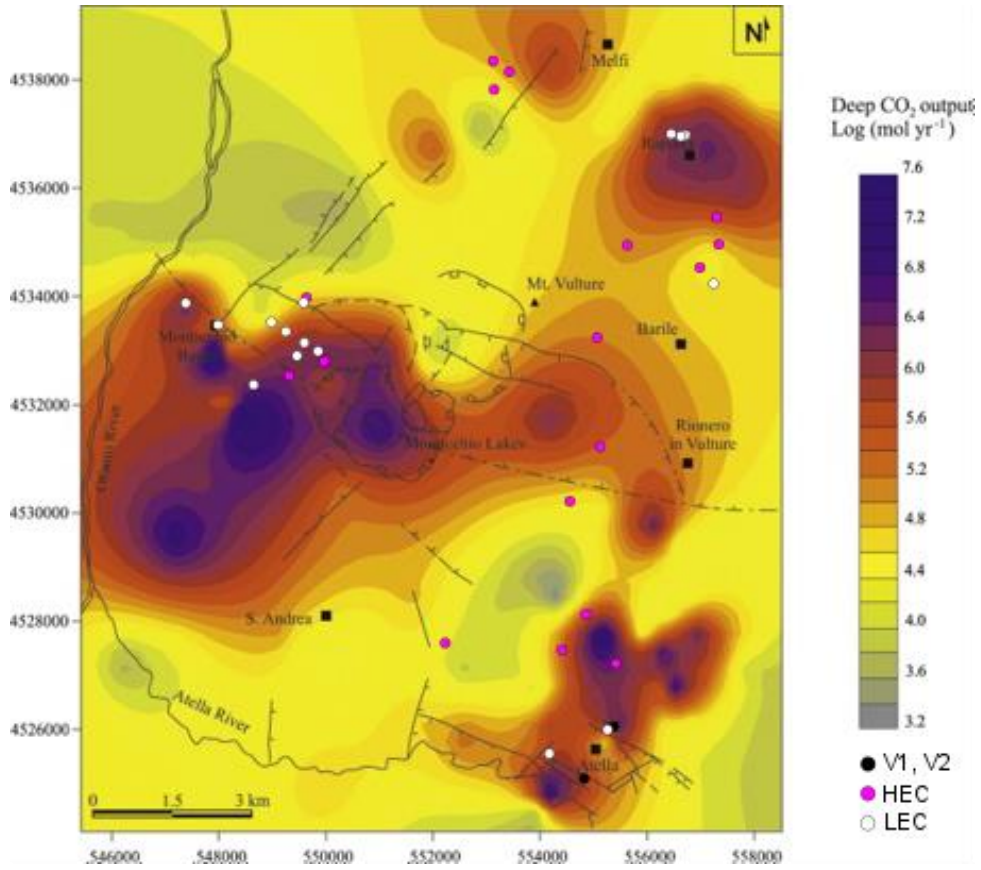

Figure 52– *Map of deep CO_2 output (log molyr^{-1}) of fluids in the Mt. Vulture line (from Caracausi et al., 2015). HEC = High electrical conductivity, LEC = low electrical conductivity.*

As for the REEs, despite the differences observed in the size of fractionation indexes, both the subset shows relevant changes with respect to the general trend associated with the volcanic rocks of the Mt. Vulture area, indicating that groundwater does not inherit volcanics REE signatures. As previously stated, the REE are dominantly complexed by carbonate ions, which form progressively stronger carbonato and dicarbonato complexes with increasing atomic number. The groundwater in the aquifer are thus MREE- and HREE-enriched relative to LREEs, a trend generally observed worldwide (Noack et al., 2014). It is generally assumed that the REE patterns in groundwater are controlled by several processes including complexation, chemical weathering, adsorption and desorption, redox control, and pH (Dia et al., 2000;

Johannesson et al., 2005; Tang and Johannesson, 2006; Pourret et al., 2010; Guo et al., 2010; Willis and Johannesson, 2011; Noack et al., 2014; Vazquez-Ortega et al., 2015; Liu et al., 2016, 2019). Therefore, the pH is thought to exert the greatest control as an independent variable over dissolved REEs with more acidic water resulting in enrichment with dissolved REEs (e.g. Worrall and Pearson, 2001; Janssen and Verweij, 2003). Overall, the relationship between the pH and the content of dissolved REEs in this study is observed to be significant ($n = 37$; $r = -0.39$, $\alpha < 0.05$; Fig.53a). Further, excluding few samples, mainly grouped along the W-NW flow path and characterised by relatively high REEs' content ($\sum$REE > 500 ng/l: V1, V6, V10, V27, V29), the correlation of the pH with dissolved REEs is stronger ($n = 33$; $r = -0.48$, $\alpha < 0.01$; Fig.53b), supporting the idea that pH exerts the main control on dissolved REEs in the Mt. Vulture aquifer.

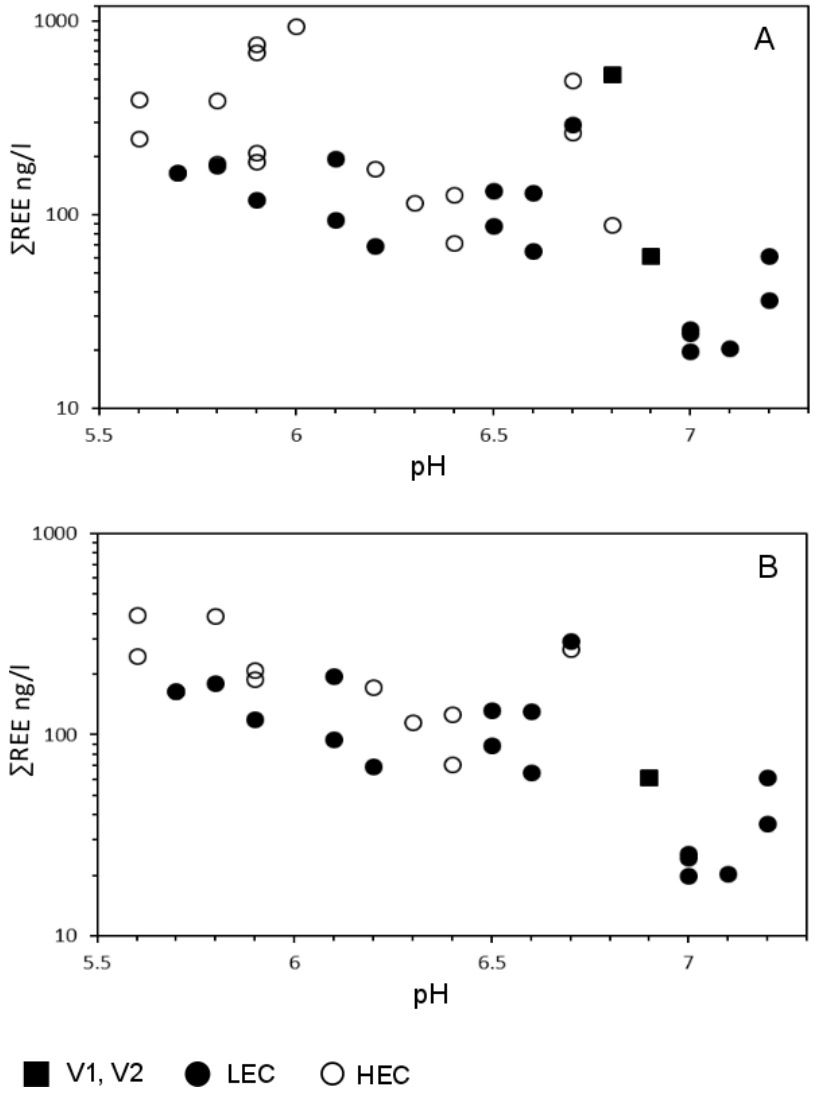

Figure 53 *– bivariate plots ∑REE vs pH. LEC = low electrical conductivity, HEC = high electrical conductivity. A) all samples, B) samples V1, V6, V10, V27, and V29 are not plotted in the diagram.*

In addition, more acidic pH promotes the existence of the LREEs in solution as free ions whereas at basic pH, the ratio of dicarbonato to carbonato species increases. It has also been suggested that the role of HCO_3^-, when pH is more basic, is not negligible (e.g. Liu et al., 2016).

However, the HCO_3^- -dissolved REEs correlation is not significant (n = 37, r = 0.23) and it is also interesting to observed that the samples of the HEC subset having ∑REE > 500 ng/l have HCO_3^- contents close to the subset average (1178 mg/l; V10 = 1214 mg/l, V27 = 1214 mg/l, V29 = 1104 mg/l), suggesting that the role of HCO_3^- on the dissolved REEs is negligible (Fig.54).

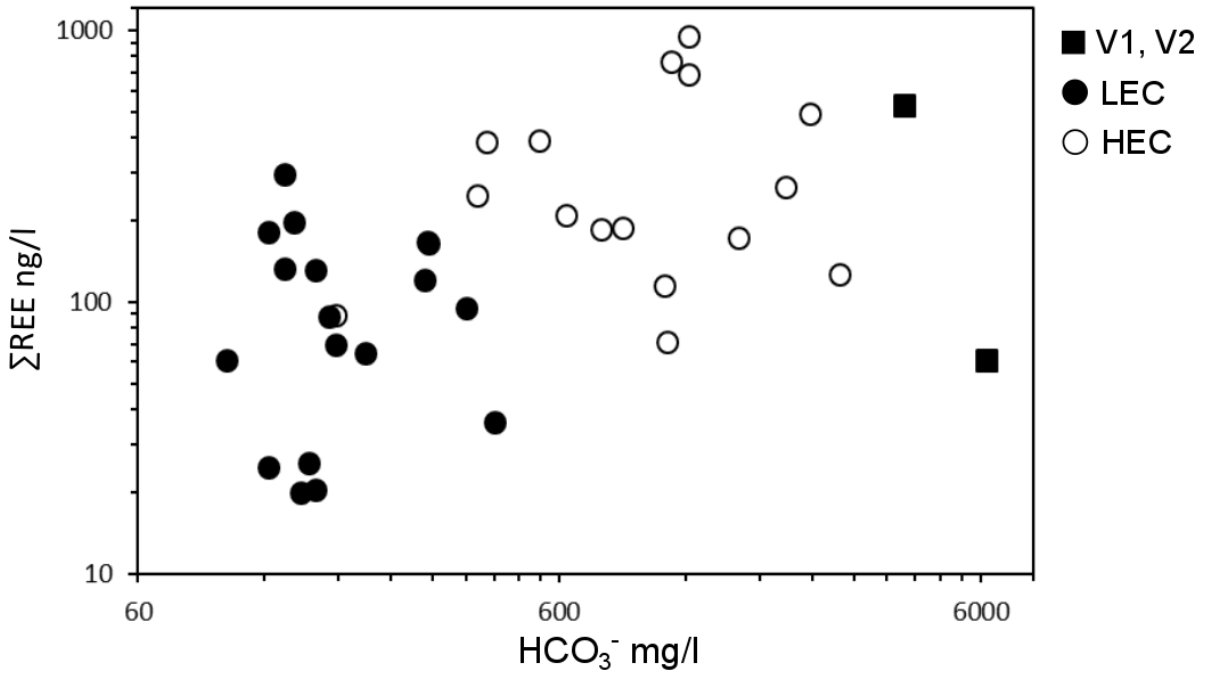

Figure 54 *– bivariate plot ∑REE vs. HCO_3^-. LEC = low electrical conductivity subset, HEC = high electrical conductivity subset.*

However, in this study, the carbonato $LnCO_3^+$ species, especially those involving HREEs, are predicted to prevail overall based on the $(La/Yb)_{PAAS}$ values observed, generally depicting an HREE enrichment relative to LREE in groundwater, especially in the discharge zone, and suggesting a preferential scavenging of the LREEs exerted by secondary minerals.

The REEs scavenging exerted by clay minerals (e.g. Johannesson and Hendry, 2000), and especially Fe(III)/Mn(IV) oxy-hydroxides (Dia et al., 2000; Gruau et al., 2004; Pourret et al., 2010; Pourret and Davranche, 2013; Liu et al., 2016, 2019), also coupled with co-precipitation,

and their possible reductive dissolution may affect the REEs' pattern of groundwater, as well as that of streamwater. For instance, Steinmann and Stille (2008) showed that, during streamwater transport, LREEs might preferentially coprecipitate with iron oxy-hydroxides in > 0.45 µm particles, affecting the LREE/HREE fractionation ratio and the Ce anomaly of the < 0.45 µm-particle stream water fraction.

Parisi et al., (2011b) showed that, especially in the discharge zone of the Mt. Vulture area, the amount of dissolved Fe and Mn might, in a few cases, reach concentrations of some thousands of µg/l, probably due to the reductive dissolution of oxyhydroxides.

The samples grouped along the W-NW flow path having ∑REE > 500 ng/l (V10, V27, V29) are characterised by very low contents of DO, well below 0.1 µmol/kg, and the sample V27 sample shows the minimum Eh value (244 mV) throughout the path. Similarly, the V1 sample, which has the highest REEs' concentration (530 ng/l) in the S-SE flow path shows very low DO (2.8 µmol/Kg) and Eh values (320 mV).

Overall, this suggests that the redox-controlled stability of Fe/Mn oxyhydroxides can significantly affect the amount of REEs in solution and the shape of the REEs' patterns. In this study, the reductive dissolution of Fe/Mn oxyhydroxides in the discharge zones can preferentially release LREE in solution (e.g. Tang and Johannesson, 2006) causing the observed reduction in the $(La/Yb)_{PAAS}$ average values compared to that in recharge zone, leading to flatter shale-normalised patterns (Willis and Johannesson, 2011).

Table 11 *- Ionic strength and saturation index (SI) of water sample. HEC = high electrical conductivity; LEC = low electrical conductivity.*

Sample	Ionic strength molal	SI Dolomite log Q/K	SI Calcite log Q/K	SI Halite log Q/k	SI Gypsum log Q/k	Subset
V1	0.172	1.34	0.03	-4.41	-0.92	-
V2	0.259	1.52	-0.17	-4.16	-1.3	-
V3	0.067	0.52	-0.26	-5.27	-0.91	HEC
V4	0.034	-1.2	-0.75	-5.73	-1.01	HEC
V5	0.009	-3.3	-1.94	-7.28	-1.78	HEC
V6	0.096	0.7	0.15	-4.83	-0.65	HEC
V7	0.077	0.45	-0.1	-4.99	-0.93	HEC
V8	0.042	-0.85	-0.74	-5.5	-1.04	HEC
V9	0.016	-1.77	-1.32	-7.07	-1.44	HEC
V10	0.023	-0.73	-0.82	-6.93	-1.27	HEC
V11	0.009	-3.43	-2.12	-7.39	-1.97	HEC
V12	0.012	-2.12	-1.48	-7.13	-1.89	HEC
V13	0.006	-4.23	-2.5	-7.7	-2.67	HEC
V14	0.03	-0.26	-0.45	-6.34	-0.45	HEC
V15	0.005	-3.64	-2.21	-7.66	-2.61	LEC
V16	0.005	-4.24	-2.54	-7.51	-2.75	LEC
V17	0.007	-2.35	-1.65	-7.56	-2.17	LEC
V18	0.004	-2.85	-1.81	-7.85	-2.47	LEC
V19	0.003	-2.47	-1.61	-8.09	-3.03	LEC
V20	0.003	-1.69	-1.28	-8.12	-2.99	LEC
V21	0.003	-4.36	-2.56	-8.03	-3.19	LEC
V22	0.003	-5.49	-3.12	-7.95	-3.15	LEC
V23	0.004	-1.55	-1.17	-7.68	-2.74	HEC
V24	0.004	-3.78	-1.33	-7.75	-2.63	LEC
V25	0.004	-2.5	-1.62	-7.91	-2.83	LEC
V26	0.001	-2.23	-1.54	-7.71	-2.75	LEC
V27	0.023	-0.95	-0.96	-6.86	-1.26	HEC
V28	0.012	-2.16	-1.55	-7.27	-2.13	HEC
V29	0.02	-1.05	-1.02	-6.97	-1.51	HEC
V30	0.004	-3.32	-2.06	-7.92	-2.86	LEC
V31	0.002	-2.02	-1.34	-8.17	-3.39	LEC
V32	0.004	-1.36	-1.06	-8.09	-3	LEC
V33	0.003	-1.73	-1.22	-8	-2.94	LEC
V34	0.004	-1.16	-0.96	-8	-3.31	LEC
V35	0.005	-3.9	-2.37	-7.51	-2.75	LEC
V36	0.01	0.75	0.08	-7.75	-2.4	LEC
V37	0.033	0.14	-0.41	-6.66	-1.11	HEC

10.2 Redox conditions and origin of the Ce and Eu anomalies

The differences in the Eh and DO values between the LEC and HEC subsets, as well as their decreasing trends along the two flow paths, suggest that redox buffering processes occur in the Mt. Vulture aquifer. As previously stated, the sulphate-bicarbonate alkaline groundwater of the aquifer, i.e. that associated with the discharge zone, has higher dissolved iron and manganese contents than those of the bicarbonate alkaline-earth and alkaline groundwater of the recharge zone (Parisi et al., 2011b), supporting the idea that Fe/Mn reduction is an important redox buffering process in the area.

It has been suggested that the Ce anomaly in groundwater reflects changes in redox conditions along the flow path (e.g. Dia et al., 2000; Gruau et al., 2004; Guo et al., 2010; Yuan et al., 2014; Liu et al., 2016) as a consequence of oxidative scavenging due to Ce^{3+} oxidation to Ce^{4+} and further adsorption/coprecipitation involving Fe/Mn oxyhydroxides.

The significant negative correlation observed in the Mt. Vulture aquifer between the DO and Ce anomaly ($n = 37$; $r = -0.57$, $\alpha < 0.05$; Fig.55) suggests that redox conditions are important in controlling the size and shape of the Ce^*_{PAAS}. Further, although the groundwater is characterised by an overall negative Ce anomaly and not clearly defined Ce^*_{PAAS} trends along the two flow paths, the HEC subset shows a smaller average size of the anomaly ($Ce^*_{PAAS} = -0.25$) compared to the LEC subset ($Ce^*_{PAAS} = -0.56$). This finding, coupled with what reported in Parisi et al. (2011b) relatively to dissolved iron and manganese, indicates that preferential desorption of Ce^{3+} occurs in the lower DO zone, i.e. in the discharge zone represented by the HEC subset, according to a three stage mechanism (Bau, 1999; Dia et al., 2000) involving initial sorption of Ce^{3+}, partial oxidation of Ce^{3+} to Ce^{4+} promoting cerianite (CeO_2) precipitation, and final preferential desorption of Ce^{3+} compared to Ce^{4+}. The lack of a significant correlation between Eh and Ce^*_{PAAS} may suggest that, in addition to the aqueous chemistry, the oxidative scavenging is affected by source composition, as proposed by Noack et al. (2014) based on the low significance of the Eh-Ce^*_{PAAS} correlation determined with a worldwide groundwater dataset.

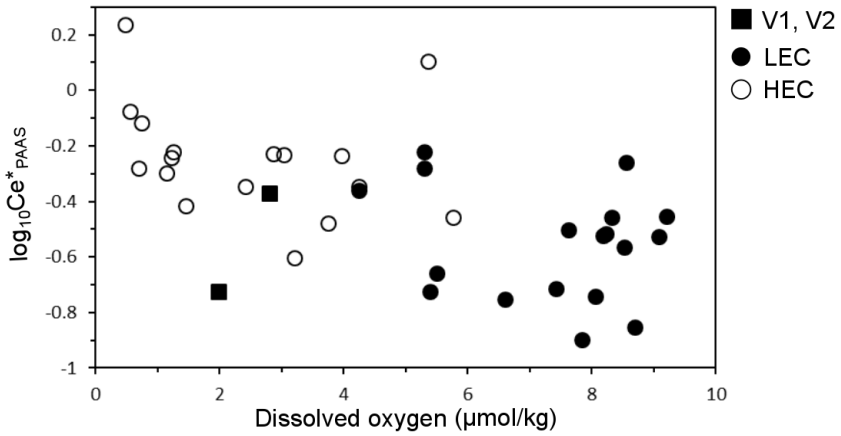

Figure 55 *- Groundwater Post-Archaean Average Shale (PAAS) Ce anomaly (Ce*) as a function of dissolved oxygen. LEC = low electrical conductivity, HEC = high electrical conductivity.*

The europium anomaly Eu^*_{PAAS} exhibits a positive correlation with both Eh ($n = 37$; $r = 0.75$, $\alpha < 0.01$) and DO ($n = 37$; $r = 0.65$, $\alpha < 0.01$) (Fig.56) although, similarly to what observed for the Ce^*_{PAAS}, not clearly defined trends are observed along the two flow paths.

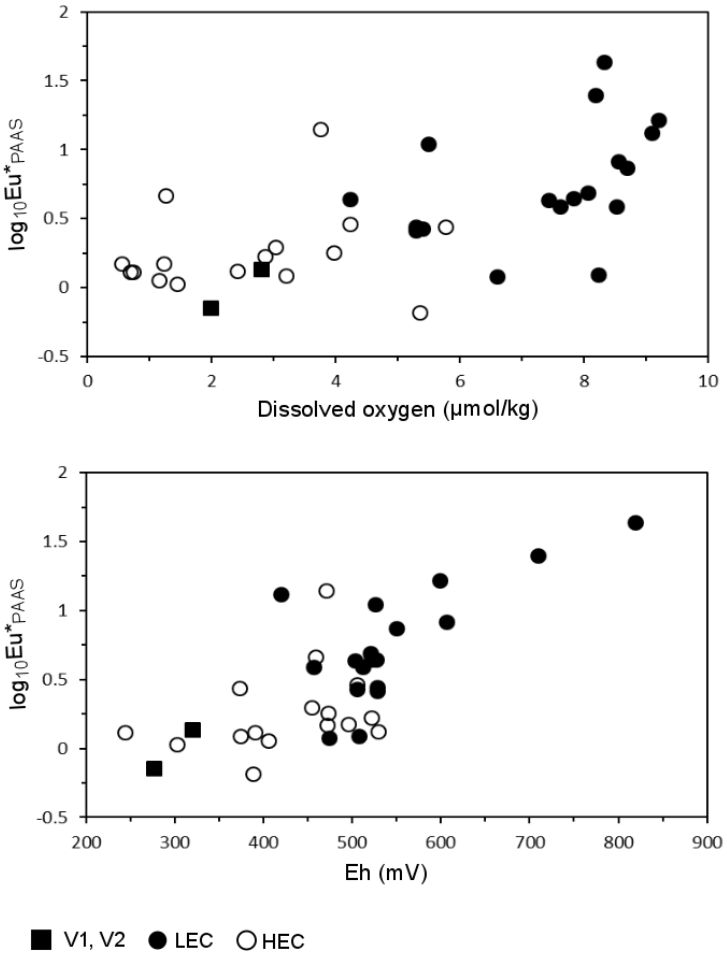

Figure 56 *- Groundwater Post-Archaean Average Shale (PAAS) Eu anomaly (Eu*) as a function of dissolved oxygen (DO) and redox potential (Eh). LEC = low electrical conductivity, HEC = high electrical conductivity.*

It is well known that positive Eu anomalies in groundwater have been mainly related to the preferential mobilisation of Eu^{2+} (e.g. Guo et al., 2010) under highly reducing conditions (e.g. Brioschi et al., 2013) requiring, at $\boldsymbol{a}_{Eu} = 10^{-8}$ and circa-neutral pH, Eh lower than -035 V (Brookins, 1988) (Fig.57). In such case, a larger positive Eu^*_{PAAS} should be observed in the discharge zone, i.e. in the HEC subset, and toward the end of the flow paths. However, the largest Eu^*_{PAAS} are observed in the LEC subset where the average Eh (543 mV) and DO (7.3 µmol/kg) values are decidedly higher than in the HEC subset (Eh = 421 mV; DO = 2.5 µmol/kg). Further, the environmental condition promoting the stability of divalent dissolved europium, namely highly reducing Eh, has never been detected in the Mt. Vulture groundwater.

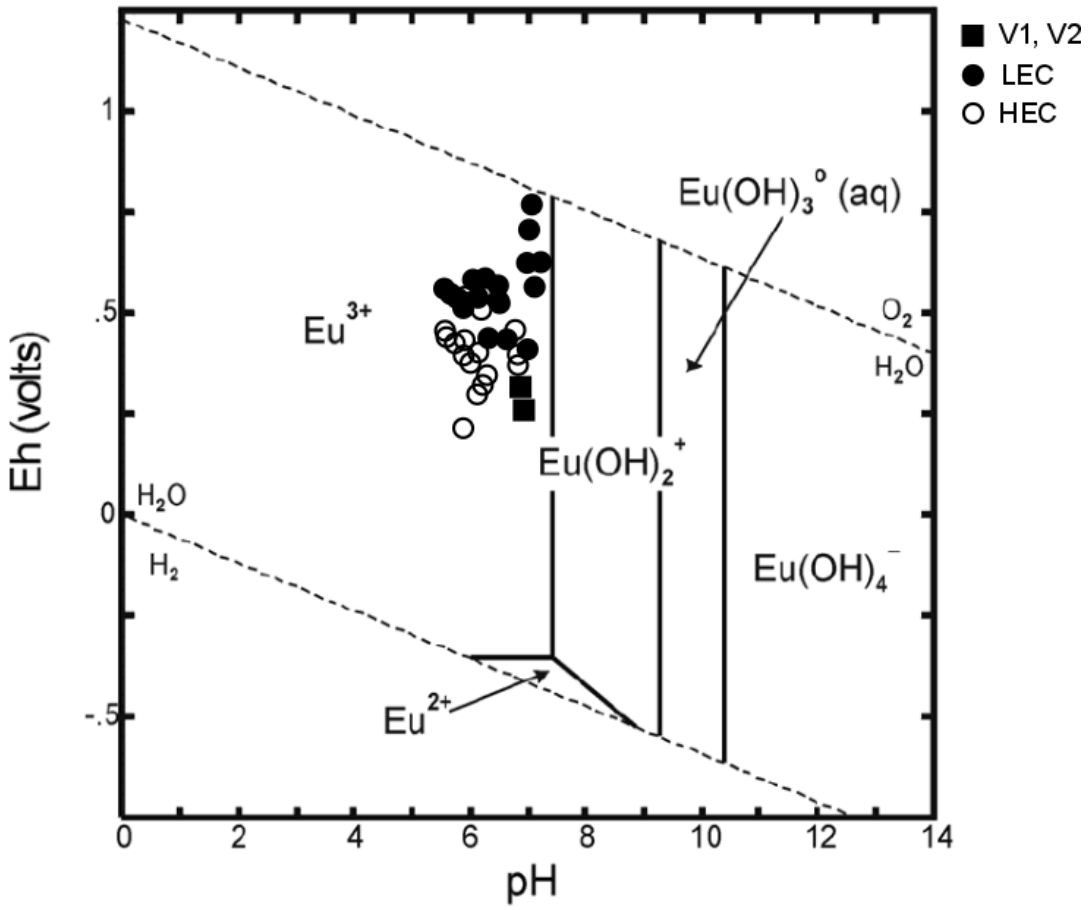

Figure 57 *– Eu Eh-pH diagram (from Brookins, 1988); LEC = low electrical conductivity, HEC = high electrical conductivity.*

Positive Eu anomalies in groundwater may also derive from water-rock interactions involving europium-rich minerals, especially feldspars (e.g. Feng, 2010; Ma et al., 2011; Brioschi et al., 2013; Vazquez-Ortega et al., 2015; Liu et al., 2016). In the Mt. Vulture, the volcanic lithologies show positive Eu^*_{PAAS}, and feldspars are frequently detected (Beccaluva et al., 2002; D'Orazio et al., 2008; Mongelli et al., 2013, 2014), supporting the hypothesis that size and shape of the

Eu^*_{PAAS} of groundwater in the recharge zone, i.e. in the LEC subset, originated by the dissolution of feldspars.

The dissolved silica content in the discharge and recharge zone is comparable (HEC average SiO_2 = 90.2 mg/l; LEC average SiO_2 = 71.5 mg/l). In the log***a***SiO_2(aq) vs log***a***(Na^+/H^+) activity diagram (Fig.58), although the most samples are in equilibrium in terms of Kaolinite, several HEC samples are close to kaolinite-smectite boundary or fall in the smectite range. This suggest that precipitation of a T-O-T clay phase probably contributes to reduce the content of dissolved silica in the discharge zone and play a role in the adsorption phenomenon.

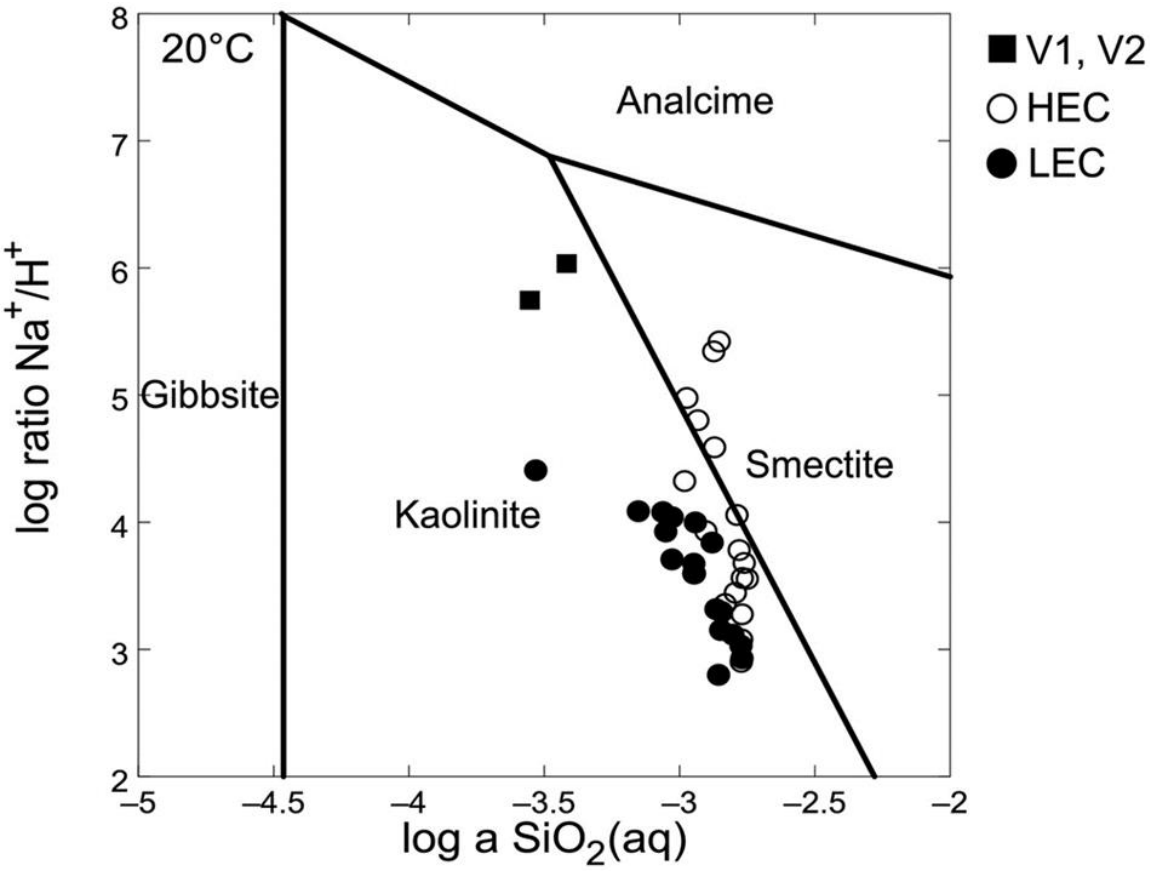

Figure 58 *- log**a** SiO2(aq) vs log**a** Na+/H+ activity plot. HEC = high electrical conductivity, LEC = low electrical conductivity.*

In the discharge zone, i.e. in the HEC subset, where most samples are in equilibrium with a 2:1 clay mineral lowest Eu^*_{PAAS} may involve, in addition to the partial oxidation of the Eu^{2+} pool, Eu^{2+} adsorption onto the clay phase surface or its inclusion in the mineral structure as exchangeable cations due to vicariance with Ca^{2+} and Sr^{2+}.

CONCLUSION

Groundwater collected from the Mt. Vulture aquifer can be categorised into recharge and discharge water subsets based on their physico-chemical features. Overall, the groundwater has REE concentrations well below 1000 ng/l, and in the discharge zone, the average content is approximately three times that in the recharge zone. In the recharge zone, the shale normalised patterns are characterised by a more negative average Ce anomaly, a more positive average Eu anomaly, and a larger average $(La/Yb)_{PAAS}$.

The observed relationship between Ce anomalies and DO supports the idea that Ce oxidative scavenging, probably involving Fe/Mn oxyhydroxides, has a role in determining the size and shape of the Ce anomaly. Further, the less negative average size of the Ce anomaly in the discharge zone also suggests desorption of Ce as Ce^{3+}, according to previous findings on the content of dissolved Fe and Mn. The desorption is related to changes in redox conditions, according to the lower Eh and DO average values observed in the discharge zone compared to the recharge zone. The lack of a significant correlation between Eh and Ce anomalies indicates that, in addition to the aqueous chemistry, the source composition affects Ce*.

Although a significant correlation is observed between Eu anomalies and Eh and DO, the strongly reducing condition promoting Eu^{3+} and Eu^{2+} is never attained in the Mt. Vulture aquifer, and the largest Eu* are associated with the recharge zone where the average Eh and DO values are higher. The volcanics occurring in the Mt. Vulture lithologies are characterised by PAAS-normalised patterns with positive Eu anomalies due to the presence of feldspars. This constraint indicates that, in the recharge zone, the size and shape of the Eu* of groundwater are largely due to the dissolution of feldspars. In the discharge zone, most samples are in equilibrium in terms of smectite content, and Eu^{2+} adsorption onto the clay phase surface or its inclusion in the mineral structure as an exchangeable cation, due to vicariance with Ca^{2+} and Sr^{2+}, could explain the smaller average size of the Eu anomaly.

Further, the occurrence of secondary minerals preferentially scavenging LREE also explains the difference in the LREE/HREE fractionation, indicated by the $(La/Yb)_{PAAS}$ index and observed between the recharge and discharge zones.

Finally, speciation calculations reveal that dissolved REEs consist mainly of carbonato complexes ($LnCO_3^+$), whereas the percentage of the dicarbonato complexes ($Ln(CO_3)_2^-$)

increases in samples with circa-neutral pH. At acidic pH, the Ln^{3+} species are important, and, in the samples from discharge zone affected by a large amount of dissolved sulphate derived by feldspathoids dissolution, the percentage of $LnSO_4^+$ species is not negligible.

Overall the REEs' distribution in the Mt. Vulture aquifer is originated by several mechanisms, including weathering reactions involving volcanic rocks, the occurrence of secondary minerals, and pH and redox control. Therefore, the REEs' geochemistry is a powerful tool in assessing the geochemical processes affecting the groundwater environment.

ACKNOWLEDGEMENTS

Undertaking this PhD has been a truly life-changing experience for me and it would not have been possible to do without the support and guidance that I received from many people.

I would like to express my deep gratitude to my supervisor **Prof. Giovanni Mongelli** for encouraging my research with his constant guidance and support and for sharing his immense knowledge, patience and kindness.

Many thanks also to **Dr. Michele Paternoster** for him precious contribution and collaboration in my research activities.

I would like to thank the National Metrology Institute of Japan (NMIJ), National Institute of Advanced Industrial Science and Technology (AIST), Tsukuba, Japan, that provided support for the REE's determination. Special thanks go to **Dr. Yanbei Zhu** of the National Institute of Advanced Industrial Science and Technology (AIST), for his professional support for the REE's determination.

Finally, I want to express my sincere gratitude to **Simona** and all **my family** for their support and encouragement during the whole period of my Ph.D.

REFERENCES

Adams, J.W., and Staatz, M.H., 1973, Rare-earth elements, in Brobst, D.A., and Pratt, W.P., eds., United States mineral resources: U.S. Geological Survey Professional Paper 820, p. 547–556. [Also available at http://pubs.er.usgs.gov/ publication/pp820.].

Alvarez, W. (1976). A former continuation of the Alps. *Geological Society of America Bulletin*, *87*(6), 891-896. https://doi.org/10.1130/0016-7606(1976)87%3C891:AFCOTA%3E2.0.CO;2.

Amato, A., & Selvaggi, G. (1993). Aftershock location and P-velocity structure in the epicentral region of the 1980 Irpinia earthquake.

Amodio-Morelli, L., Bonardi, G., Colonna, V., Dietrich, D., Giunta, G., Ippolito, F., Liguori, V., Lorenzoni, S., Paglionico, A., Perrone, V., Piccareta, G., Russo, M., Scandone, P., Zanettin-Lorenzoni, E. and Zuppetta, A. (1976) – *L'arco Calabro-Peloritano nell'orogene Appenninico-Maghrebide*. Bollettino della Società Geologica Italiana **1**7, 1-60.

Anderson, H., & Jackson, J. (1987). Active tectonics of the Adriatic region. *Geophysical Journal International*, *91*(3), 937-983. https://doi.org/10.1111/j.1365-246X.1987.tb01675.x.

Appleton, J. D. (1972). Petrogenesis of potassium-rich lavas from the Roccamonfina Volcano, Roman Region, Italy. *Journal of Petrology*, *13*(3), 425-456. https://doi.org/10.1093/petrology/13.3.425.

Aubert, D., Stille, P., Probst, A., Gauthier-Lafaye, F., & Pourcelot, L. (2002). Characterization and migration of atmospheric REE in soils and surface waters. *Geochimica et Cosmochimica Acta*, *66*(19), 3339-3350. https://doi.org/10.1016/S0016-7037(02)00913-4.

Bailey, D. K., & Collier, J. D. (2000). Carbonatite-melilitite association in the Italian collision zone and the Ugandan rifted craton: significant common factors. *Mineralogical Magazine*, *64*(4), 675-682. https://doi.org/10.1180/002646100549698.

Ball, J.W., & Nordstrom, D.K. (1991). User's manual for WATEQ4F, with revised thermodynamic data base and test cases for calculating speciation of major, trace, and redox elements in natural waters. *US Geological Survey Open File Report 91-183.*

Barbieri, M., Barbieri, M. Jr., D'orefice, M., Graciotti, R. and Stoppa, F. (2002). Il vulcanismo monogenico medio-pleistocenico della conca di Carsoli (L'Aquila). *Geologica Romana, **36**, 13-31.*

Bau, M. (1999). Scavenging of dissolved yttrium and rare earths by precipitating iron oxyhydroxide: experimental evidence for Ce oxidation, Y-Ho fractionation, and lanthanide tetrad effect. *Geochimica et Cosmochimica Acta*, *63*(1), 67-77. https://doi.org/10.1016/S0016-7037(99)00014-9.

Beccaluva, L., Bianchini, G., & Siena, F. (2004). Tertiary-Quaternary volcanism and tectono-magmatic evolution in Italy.

Beccaluva, L., Brotzu, P., Macciotta, G., Morbidelli, L., & Serri, G. (1989). Cainozoic tectono-magmatic evolution and inferred mantle sources in the Sardo-Tyrrhenian area.

Beccaluva, L., Coltorti, M., Di Girolamo, P., Melluso, L., Milani, L., Morra, V., & Siena, F. (2002). Petrogenesis and evolution of Mt. Vulture alkaline volcanism (Southern Italy). *Mineralogy and Petrology*, *74*(2-4), 277-297. https://doi.org/10.1007/s007100200007.

Beneduce, P., & Giano, S. I. (1996). Osservazioni preliminari sull'assetto morfostrutturale dell'edificio vulcanico del Monte Vulture (Basilicata). *Il Quaternario*, *9*(1), 325-330.

Beneduce, P., & Schiattarella, M. (1997). Relazioni tra tettonica regionale quaternaria e deformazione vulcanogenica nelle aree dei Campi Flegrei, Isola di Ustica e Monte Vulture (Italia meridionale). *Il Quaternario*, *10*, 583-588.

Bethke, C.M., and Yeakel, S., (2014). The Geochemist's Workbench User's Guides, Version 10.0. *Aqueous Solutions LLC, Champaign*.

Biddau, R., Cidu, R., & Frau, F. (2002). Rare earth elements in waters from the albitite-bearing granodiorites of Central Sardinia, Italy. *Chemical Geology*, *182*(1), 1-14. https://doi.org/10.1016/S0009-2541(01)00272-8.

Boccaletti, M., Elter, P., & Guazzone, G. (1971). Plate tectonic models for the development of the Western Alps and Northern Apennines. *Nature Physical Science*, *234*(49), 108-111.

Boenzi, F., La Volpe, L., & Rapisardi, L. (1987). Evoluzione geomorfologica del complesso vulcanico del Monte Vulture (Basilicata). *Bollettino della Società geologica italiana*, *106*(4), 673-682.

Bonadonna, F. P., Brocchini, D., Laurenzi, M. A., Principe, C., & Ferrara, G. (1998). Stratigraphical and chronological correlations between Monte Vulture volcanics and sedimentary deposits of the Venosa basin. *Quaternary International*, *47*, 87-96. https://doi.org/10.1016/S1040-6182(97)00074-8.

Bonardi, G., Amore, F. O., Ciampo, G., De Capoa, P., & Miconnet, P. (1988). Il complesso Liguride Auct.: Stato delle conoscenze e problemi aperti dulla sur evoluzione pre-Appenninica ed i suoli rapporti con l'Arco Calabro. *Memorie della Società Geologica Italiana*, *41*, 17-35.

Bonardi, G., Ciarcia, S., Di Nocera, S., Matano, F., Sgrosso, I., & Torre, M. (2009). Carta delle principali unità cinematiche dell'Appennino meridionale. Nota illustrativa. *Bollettino della Società Geologica Italiana*, *128*(1), 47-60.

Bonini, M., & Sani, F. (2000). Pliocene-Quaternary transpressional evolution of the Anzi-Calvello and northern S. Arcangelo basins (Basilicata, Southern Apennines, Italy) as a consequence of deep-seated fault reactivation. *Marine and Petroleum Geology*, *17*(8), 909-927. https://doi.org/10.1016/S0264-8172(00)00028-3.

Bordoni, P., & Valensise, G. (1999). Deformation of the 125 ka marine terrace in Italy: tectonic implications. *Geological Society, London, Special Publications*, *146*(1), 71-110. https://doi.org/10.1144/GSL.SP.1999.146.01.05.

Brioschi, L., Steinmann, M., Lucot, E., Pierret, M. C., Stille, P., Prunier, J., & Badot, P. M. (2013). Transfer of rare earth elements (REE) from natural soil to plant systems: implications for the environmental availability of anthropogenic REE. *Plant and soil*, *366*(1-2), 143-163. https://doi.org/10.1007/s11104-012-1407-0.

Brocchini, D., La Volpe, L., Laurenzi, M. A., & Principe, C. (1994). Storia evolutiva del Monte Vulture. *Plinius*, *12*, 22-25.

Brookins, D. G. (1988). Nickel. In *Eh-pH Diagrams for Geochemistry* (pp. 68-70). Springer, Berlin, Heidelberg. https://doi.org/10.1007/978-3-642-73093-1_28.

Bucher, K., & Stober, I. (2010). Fluids in the upper continental crust. *Geofluids*, 10(1-2), 241-253. https://doi.org/10.1111/j.1468-8123.2010.00279.x.

Buettner, A., Principe, C., Villa, I. M. Bocchini, D. (2006) - Geocronologia 39Ar -40Ar del Monte Vulture. La Geologia del Monte Vulture (a cura di Claudia Principe), 73-86, *Grafiche Finiguerra*.

Butler, R. W. H. (1989). The influence of pre-existing basin structure on thrust system evolution in the Western Alps. *Geological Society, London, Special Publications*, *44*(1), 105-122. https://doi.org/10.1144/GSL.SP.1989.044.01.07.

Byrne, R. H., & Kim, K. H. (1990). Rare earth element scavenging in seawater. *Geochimica et Cosmochimica Acta*, *54*(10), 2645-2656. https://doi.org/10.1016/0016-7037(90)90002-3.

Cadoux, A., Pinti, D. L., Aznar, C., Chiesa, S., & Gillot, P. Y. (2005). New chronological and geochemical constraints on the genesis and geological evolution of Ponza and Palmarola volcanic islands (Tyrrhenian Sea, Italy). *Lithos*, *81*(1-4), 121-151. https://doi.org/10.1016/j.lithos.2004.09.020.

Caiazzo, C., Giovine, G., Ortolani, F., Pagliuca, S., Schiattarella, M. and Vitale, C. (1992). Genesi ed evoluzione strutturale della depressione tettonica dell'alta valle del fiume Sele (Appennino Campano-Lucano*). Studi Geol. Camerti, Vol. Spec.*, 245-255.

Calcagnile, G., & Panza, G. F. (1980). The main characteristics of the lithosphere-asthenosphere system in Italy and surrounding regions. *Pure and Applied Geophysics*, *119*(4), 865-879. https://doi.org/10.1007/BF01131263.

Capitanio, F., Larocca, F., & Improta, S. (2004). High-temperature rapid pyrometamorphism induced by a charcoal pit burning: The case of Ricetto, central Italy. *International Journal of Earth Sciences*, *93*(1), 107-118. https://doi.org/10.1007/s00531-003-0374-3.

Caracausi, A., & Paternoster, M. (2015). Radiogenic helium degassing and rock fracturing: A case study of the southern Apennines active tectonic region. *Journal of Geophysical Research: Solid Earth*, *120*(4), 2200-2211. https://doi.org/10.1002/2014JB011462.

Caracausi, A., Martelli, M., Nuccio, P. M., Paternoster, M., & Stuart, F. M. (2013). Active degassing of mantle-derived fluid: A geochemical study along the Vulture line, southern Apennines (Italy). *Journal of volcanology and geothermal research*, *253*, 65-74. https://doi.org/10.1016/j.jvolgeores.2012.12.005.

Caracausi, A., Paternoster, M., & Nuccio, P. M. (2015). Mantle CO2 degassing at Mt. Vulture volcano (Italy): Relationship between CO2 outgassing of volcanoes and the time of their last eruption. *Earth and planetary science letters*, *411*, 268-280. https://doi.org/10.1016/j.epsl.2014.11.049.

Casciello, E., Pappone, G. and Zappetta, A. (2002b). Structural features of a shear-zone developed in an argillaceous medium: the southern portion of the Scorciabuoi fault (southern Apennines). *Boll. Soc. Geol. It.*, Volume Speciale 1, 659-667.

Casero, P., Roure, F., Moretti, I., Muller, C., Sage, L., & Vially, R. (1988). Evoluzione geodinamica neogenica dell'Appennino meridionale. *Mem. Soc. Geol. It*, *41*, 109-120.

Catalano, S., Monaco, C., Tortorici, L., & Tansi, C. (1993). Pleistocene strike-slip tectonics in the Lucania Apennine (southern Italy). *Tectonics*, *12*(3), 656-665. https://doi.org/10.1029/92TC02251.

Catalano, S., Monaco, C., Tortorici, L., Paltrinieri, W., & Steel, N. (2004). Neogene-Quaternary tectonic evolution of the southern Apennines. *Tectonics*, *23*(2). https://doi.org/10.1029/2003TC001512.

Celico, P., & Summa, G. (2004). Idrogeologia dell'area del Vulture (Basilicata). *Bollettino della Società geologica italiana*, *123*(3), 343-356.

Cello, G., & Mazzoli, S. (1998). Apennine tectonics in southern Italy: a review. *Journal of Geodynamics*, *27*(2), 191-211. https://doi.org/10.1016/S0264-3707(97)00072-0.

Cello, G., Lentini, F., & Tortorici, L. (1990). La struttura del settore calabro-lucano e suo significato nel quadro dell'evoluzione tettonica del sistema a thrust sudappenninico. http://dx.doi.org/10.15165/studgeocam-844.

Cello, G., Tondi, E., Micarelli, L., & Mattioni, L. (2003). Active tectonics and earthquake sources in the epicentral area of the 1857 Basilicata earthquake (southern Italy). *Journal of Geodynamics*, *36*(1-2), 37-50. https://doi.org/10.1016/S0264-3707(03)00037-1.

Cello, G., Tortorici, L., Martini, N., & Paltrinieri, W. (1989). Structural styles in the frontal zones of the southern Apennines, Italy: an example from the Molise district. *Tectonics*, *8*(4), 753-768. https://doi.org/10.1029/TC008i004p00753.

Cello, G., Turco, E., & Zuppetta, A. (1995). Cinematica del settore centrale del Mediterraneo ed implicazioni sulla struttura dell'arco calabro. *Cinquant'anni di attivita didattica del Prof. F. Ippolito, Napoli, Liguori Editore*, *293*.

Chakhmouradian, A. R., & Zaitsev, A. N. (2012). Rare earth mineralization in igneous rocks: sources and processes. *Elements*, *8*(5), 347-353. https://doi.org/10.2113/gselements.8.5.347.

Chiarabba, C., Jovane, L., & DiStefano, R. (2005). A new view of Italian seismicity using 20 years of instrumental recordings. *Tectonophysics*, *395*(3-4), 251-268. https://doi.org/10.1016/j.tecto.2004.09.013.

Choi, H. S., Yun, S. T., Koh, Y. K., Mayer, B., Park, S. S., & Hutcheon, I. (2009). Geochemical behavior of rare earth elements during the evolution of CO2-rich groundwater: a study from the Kangwon district, South Korea. *Chemical Geology*, *262*(3-4), 318-327. https://doi.org/10.1016/j.chemgeo.2009.01.031.

Ciaranfi, N., Ghisetti, F., Guida, M., Iaccarino, G., Lambiase, S., Pieri, P., ... & Vezzani, L. (1983). Carta neotettonica dell'Italia meridionale. *Progetto Finalizzato Geodinamica del CNR*, *515*, 62.

Ciccacci, S., Del Gaudio, V., La Volpe, L., & Sansò, P. (1999). Geomorphological features of Monte Vulture Pleistocene Volcano (Basilicata, southern Italy). *Zeitschrift für Geomorphologie. Supplementband*, (114), 29-48.

Cinque, A., Patacca, E., Scandone, P., & Tozzi, M. (1993). Quaternary kinematic evolution of the Southern Appennines. Relationships between surface geological features and deep lithospheric structures. *Annals of Geophysics*, *36*(2).

Civetta, L., Orsi, G., Scandone, P., & Pece, R. (1978). Eastwards migration of the Tuscan anatectic magmatism due to anticlockwise rotation of the Apennines. *Nature*, *276*(5688), 604-606.

Civetta, L., Francalanci, L., Manetti, P., & Peccerillo, A. (1989). Petrological and geochemical variations across the Roman Comagmatic Province: inference on magma genesis and crust-mantle evolution.

Cocco, E., Cravero, E., Ortolani, F., Pescatore, T., Russo, M., Sgrosso, I., & Torre, M. (1972). Les facies sedimentaires miocènes du bassin Irpinien (Italie Meridionale). *Atti Acc. Pontaniana*, *21*, 1-13.

Comodi, P., Liu, Y., Stoppa, F., & Woolley, A. R. (1999). A multi-method analysis of Si-, S-and REE-rich apatite from a new find of kalsilite-bearing leucitite (Abruzzi, Italy). *Mineralogical Magazine*, *63*(5), 661-672. https://doi.org/10.1180/002646199548826.

Conticelli, S., & Peccerillo, A. (1992). Petrology and geochemistry of potassic and ultrapotassic volcanism in central Italy: petrogenesis and inferences on the evolution of the mantle sources. *Lithos*, *28*(3-6), 221-240. https://doi.org/10.1016/0024-4937(92)90008-M.

Conticelli, S., D'antonio, M., Pinarelli, L., & Civetta, L. (2002). Source contamination and mantle heterogeneity in the genesis of Italian potassic and ultrapotassic volcanic rocks: Sr–Nd–Pb isotope data from Roman Province and Southern Tuscany. *Mineralogy and Petrology*, *74*(2-4), 189-222. https://doi.org/10.1007/s007100200004.

Corrado, G. & Rapolla, A. (1981) - The gravity field of Italy: analysis of its spectral composition and delineation of a three-dimensional crust model for Central-Southern Italy. *Boll. Geof. Teor. Appl.*, **23**, 17-29.

Corrado, S., Aldega, L., Di Leo, P., Giampaolo, C., Invernizzi, C., Mazzoli, S., & Zattin, M. (2005). Thermal maturity of the axial zone of the southern Apennines fold-and-thrust belt (Italy) from multiple organic and inorganic indicators. *Terra Nova*, *17*(1), 56-65. https://doi.org/10.1111/j.1365-3121.2004.00584.x.

Crisci, G., De Fino, M., La Volpe, L., & Rapisardi, L. (1983). Pleistocene ignimbrites of Monte Vulture (Basilicata, Southern Italy). *Neues Jahrbuch für Geologie und Paläontologie Monatshefte*, *12*, 731-746.

Cundari, A. (1979). Petrogenesis of leucite-bearing lavas in the Roman volcanic region, Italy. *Contributions to Mineralogy and Petrology*, *70*(1), 9-21. https://doi.org/10.1007/BF00371867.

Cundari, A. (1994). Role of subduction in the genesis of potassic rocks: a discussion paper on the unfashionable side of the role. *Miner. Petrol. Acta*, *37*, 81-90.

Cundari, A., & Ferguson, A. K. (1991). Petrogenetic relationships between melilitite and lamproite. *Contributions to Mineralogy and Petrology*, *107*(3), 343-357. https://doi.org/10.1007/BF00325103.

Davranche, M., Gruau, G., Dia, A., Marsac, R., Pédrot, M., & Pourret, O. (2015). Biogeochemical factors affecting rare earth element distribution in shallow wetland groundwater. *Aquatic geochemistry*, *21*(2-4), 197-215. https://doi.org/10.1007/s10498-014-9247-6.

Davranche, M., Grau, G., Dia, A., Le Coz-Bouhnik, M., Marsac, R., Pédrot, M., & Pourret, O. (2016). Rare earth elements in wetlands. In *Trace elements in waterlogged soils and sediments* (pp. 135-162). CRC Press Taylor & Francis Group Boca Raton, London, New York.

De Astis, G., Kempton, P. D., Peccerillo, A., & Wu, T. W. (2006). Trace element and isotopic variations from Mt. Vulture to Campanian volcanoes: constraints for slab detachment and mantle inflow beneath southern Italy. *Contributions to Mineralogy and Petrology*, *151*(3), 331-351. https://doi.org/10.1007/s00410-006-0062-y.

De Astis, G., Ventura, G. and Vilardo, G. (2003). Geodynamic significance of the Aeolian volcanism (Southern Tyrrhenian Sea, Italy) in light of structural, seismological and geochemical data. *Tectonics*, *22*. doi: 10.1029/2003TC001506.

De Fino, M., La Volpe, L., & Piccarreta, G. (1982). Magma evolution at mount vulture (Southern Italy). Bulletin Volcanologique, 45(2), 115-126. https://doi.org/10.1007/BF02600428.

De Fino, M., La Volpe, L., Peccerillo, A., Piccarreta, G., & Poli, G. (1986). Petrogenesis of Monte Vulture volcano (Italy): inferences from mineral chemistry, major and trace element data. *Contributions to Mineralogy and Petrology, 92(2), 135-145.* https://doi.org/10.1007/BF00375289.

Dercourt, J., Zonenshain, L. P., Ricou, L. E., Kazmin, V. G., Le Pichon, X., Knipper, A. L., ... & Pechersky, D. H. (1986). Geological evolution of the Tethys belt from the Atlantic to the Pamirs since the Lias. *Tectonophysics*, *123*(1-4), 241-315. https://doi.org/10.1016/0040-1951(86)90199-X.

Dewey, J. F., Helman, M. L., Knott, S. D., Turco, E., & Hutton, D. H. W. (1989). Kinematics of the western Mediterranean. *Geological Society, London, Special Publications*, *45*(1), 265-283. https://doi.org/10.1144/GSL.SP.1989.045.01.15.

Dia, A., Gruau, G., Olivié-Lauquet, G., Riou, C., Molénat, J., & Curmi, P. (2000). The distribution of rare earth elements in groundwaters: assessing the role of source-rock composition, redox changes and colloidal particles. *Geochimica et Cosmochimica Acta*, *64*(24), 4131-4151. https://doi.org/10.1016/S0016-7037(00)00494-4.

Dietrich, D. (1988). Sense of overthrust shear in the Alpine nappes of Calabria (southern Italy). *Journal of Structural Geology*, *10*(4), 373-381. https://doi.org/10.1016/0191-8141(88)90015-6.

Di Muro, A., Bonaccorsi, E., & Principe, C. (2004). Complex colour and chemical zoning of sodalite-group phases in a hauynophyre lava from Mt. Vulture, Italy. *Mineralogical Magazine*, *68*(4), 591-614. https://doi.org/10.1180/0026461046840206.

Doglioni, C. (1991). A proposal for the kinematic modelling of W-dipping subductions-possible applications to the Tyrrhenian-Apennines system. *Terra Nova*, *3*(4), 423-434. https://doi.org/10.1111/j.1365-3121.1991.tb00172.x.

Doglioni, C., Innocenti, F., & Mariotti, G. (2001). Why Mt Etna?. *Terra Nova*, *13*(1), 25-31. https://doi.org/10.1046/j.1365-3121.2001.00301.x.

Doglioni, C., Merlini, S., & Cantarella, G. (1999). Foredeep geometries at the front of the Apennines in the Ionian Sea (central Mediterranean). *Earth and Planetary Science Letters*, *168*(3-4), 243-254. https://doi.org/10.1016/S0012-821X(99)00059-X.

Doglioni, C., Mongelli, F., & Pieri, P. (1994). The Puglia uplift (SE Italy): an anomaly in the foreland of the Apenninic subduction due to buckling of a thick continental lithosphere. *Tectonics*, *13*(5), 1309-1321. https://doi.org/10.1029/94TC01501.

D'orazio, M., Innocenti, F., Tonarini, S., & Doglioni, C. (2007). Carbonatites in a subduction system: the Pleistocene alvikites from Mt. Vulture (southern Italy). *Lithos*, *98*(1-4), 313-334. https://doi.org/10.1016/j.lithos.2007.05.004.

D'Orazio, M., Innocenti, F., Tonarini, S., & Doglioni, C. (2008). Reply to the discussion of:"Carbonatites in a subduction system: The Pleistocene alvikites from Mt. Vulture (Southern Italy)" by M. D'Orazio, F. Innocenti, S. Tonarini and C. Doglioni (Lithos 98, 313–334) by F. Stoppa, C. Principe and P. Giannandrea. *Lithos*, *103*(3-4), 557-561.

Downes, H., Kostoula, T., Jones, A., Beard, A., Thirlwall, M., & Bodinier, J. L. (2002). Geochemistry and Sr–Nd isotopic compositions of mantle xenoliths from the Monte Vulture carbonatite–melilitite volcano, central southern Italy. *Contributions to Mineralogy and Petrology*, *144*(1), 78-92. https://doi.org/10.1007/s00410-002-0383-4.

Duncan, T., & Shaw, T. J. (2003). The mobility of rare earth elements and redox sensitive elements in the groundwater/seawater mixing zone of a shallow coastal aquifer. *Aquatic geochemistry*, *9*(3), 233-255. https://doi.org/10.1023/B:AQUA.0000022956.20338.26.

Duvert, C., Cendón, D. I., Raiber, M., Seidel, J. L., & Cox, M. E. (2015). Seasonal and spatial variations in rare earth elements to identify inter-aquifer linkages and recharge processes in an Australian catchment. *Chemical Geology*, *396*, 83-97. https://doi.org/10.1016/j.chemgeo.2014.12.022.

Elderfield, H., Upstill-Goddard, R., & Sholkovitz, E. R. (1990). The rare earth elements in rivers, estuaries, and coastal seas and their significance to the composition of ocean waters. *Geochimica et Cosmochimica Acta*, *54*(4), 971-991. https://doi.org/10.1016/0016-7037(90)90432-K.

Feng, J. L. (2010). Behaviour of rare earth elements and yttrium in ferromanganese concretions, gibbsite spots, and the surrounding terra rossa over dolomite during chemical weathering. *Chemical Geology*, *271*(3-4), 112-132. https://doi.org/10.1016/j.chemgeo.2010.01.003.

Ferranti, L., Oldow, J. S., & Sacchi, M. (1996). Pre-Quaternary orogen-parallel extension in the Southern Apennine belt, Italy. *Tectonophysics*, *260*(4), 325-347. https://doi.org/10.1016/0040-1951(95)00209-X.

Finetti, I.R. and Del Ben, A. (1986) - *Geophysical study of the Tyrrhenian opening.* Boll. Geof. Teor. Appl., **110**, 75-156.

Frape, S. K., Blyth, A., Blomqvist, R., McNutt, R. H., & Gascoyne, M. (2003). Deep fluids in the continents: II. Crystalline rocks. *Treatise on geochemistry*, *5*, 605. https://ui.adsabs.harvard.edu/link_gateway/2003TrGeo...5..541F/doi:10.1016/B0-08-043751-6/05086-6.

Freeze, R. A., & Cherry, J. A. (1979). Groundwater. Pretice-Hall. *Inc., Englewood Cliffs, NJ*.

Gallicchio, S., & Maiorano, P. (1999). Revised stratigraphy of the Serra Palazzo Formation, a Miocene foredeep turbidite succession of the Southern Apennines (Italy). *Rivista Italiana di Paleontologia e Stratigrafia*, *105*(2). https://doi.org/10.13130/2039-4942/5377.

Gasperini, D., Blichert-Toft, J., Bosch, D., Del Moro, A., Macera, P., & Albarede, F. (2002). Upwelling of deep mantle material through a plate window: evidence from the geochemistry of Italian basaltic volcanics. *Journal of Geophysical Research: Solid Earth*, *107*(B12), ECV-7. https://doi.org/10.1029/2001JB000418.

German, C. R., & Elderfield, H. (1990). Application of the Ce anomaly as a paleoredox indicator: the ground rules. *Paleoceanography*, *5*(5), 823-833. https://doi.org/10.1029/PA005i005p00823.

German, C. R., Holliday, B. P., & Elderfield, H. (1991). Redox cycling of rare earth elements in the suboxic zone of the Black Sea. *Geochimica et Cosmochimica Acta*, *55*(12), 3553-3558. https://doi.org/10.1016/0016-7037(91)90055-A.

Giannandrea, P. (2003). Analisi sedimentologica del Sintema di Monte Sirico (parte alta della successione del Bacino dell'Ofanto. *Il Quaternario, 16*, 511-521.

Giannandrea, P. (2004). I depositi terrazzati affioranti nell'alta valle del Fiume Ofanto (Foglio n. 451 ''Melfi'', Appennino campanolucano). *Il Quaternario, Italian Journal of Quaternary Sciences*, *17*, 511-521.

Giannandrea, P., La Volpe, L., Principe, C., & Schiattarella, M. (2004). Carta geologica del Monte Vulture alla scala 1: 25.000. *Litografia Artistica Cartografica, Firenze*.

Giannandrea, P., La Volpe, L., Principe, C., & Schiattarella, M. (2006). Unità stratigrafiche a limiti inconformi e storia evolutiva del vulcano medio-pleistocenico di Monte Vulture (Appennino meridionale, Italia). *Bollettino-Società Geologica Italiana*, *125*(1), 67.

Göb, S., Loges, A., Nolde, N., Bau, M., Jacob, D. E., &Markl, G. (2013). Major and trace element compositions (including REE) of mineral, thermal, mine and surface waters in SW Germany and implications for water–rock interaction. *Applied Geochemistry*, *33*, 127-152. https://doi.org/10.1016/j.apgeochem.2013.02.006.

Goldstein, S. J., & Jacobsen, S. B. (1988). Rare earth elements in river waters. *Earth and Planetary Science Letters*, *89*(1), 35-47.

Govers, R., & Wortel, M. J. R. (2005). Lithosphere tearing at STEP faults: Response to edges of subduction zones. *Earth and Planetary Science Letters*, *236*(1-2), 505-523. https://doi.org/10.1016/j.epsl.2005.03.022.

Gromet, L. P., Haskin, L. A., Korotev, R. L., & Dymek, R. F. (1984). The "North American shale composite": its compilation, major and trace element characteristics. *Geochimica et Cosmochimica Acta*, *48*(12), 2469-2482.

Gruau, G., Dia, A., Olivie-Lauquet, G., Davranche, M., & Pinay, G. (2004). Controls on the distribution of rare earth elements in shallow groundwaters. *Water Research*, *38*(16), 3576-3586. https://doi.org/10.1016/j.watres.2004.04.056.

Guo, H., Zhang, B., Wang, G., & Shen, Z. (2010). Geochemical controls on arsenic and rare earth elements approximately along a groundwater flow path in the shallow aquifer of the Hetao Basin, Inner Mongolia. *Chemical Geology*, *270*(1-4), 117-125. https://doi.org/10.1016/j.chemgeo.2009.11.010.

Gupta, A. K., & Fyfe, W. S. (2003). *The young potassic rocks*. Ane Books.

Gustafsson, J.P., (2010). Visual MINTEQ thermodynamic databases in GWB format. http://www2.lwr.kth.se/English/OurSoftware/vminteq/download.html.

Gvirtzman, Z., & Nur, A. (1999). The formation of Mount Etna as the consequence of slab rollback. *Nature*, *401*(6755), 782-785.

Inguaggiato, C., Burbano, V., Rouwet, D., & Garzón, G. (2017). Geochemical processes assessed by Rare Earth Elements fractionation at "Laguna Verde" acidic-sulphate crater lake (Azufral volcano, Colombia). *Applied geochemistry*, *79*, 65-74. https://doi.org/10.1016/j.apgeochem.2017.02.013.

Inguaggiato, C., Censi, P., Zuddas, P., Londono, J. M., Chacón, Z., Alzate, D., ... & D'Alessandro, W. (2015). Geochemistry of REE, Zr and Hf in a wide range of pH and water composition: The Nevado del Ruiz volcano-hydrothermal system (Colombia). *Chemical geology*, *417*, 125-133. https://doi.org/10.1016/j.chemgeo.2015.09.025.

Haccard, D., Lorenz, C. and Grandjacquet, C. (1972). *Essai sur l'evolution tectogenetique de la liaison Alpes-Apennines (de la Ligurie a la Calabre).* Memorie della Società Geologica Italiana **11**, 309-341.

Hannigan, R. E., & Sholkovitz, E. R. (2001). Rare earth element chemistry of natural waters: chemical weathering and dissolved REE contents in major river systems. *Chemical Geology*, *175*, 495-508. https://doi.org/10.1016/S0009-2541(00)00355-7.

Harkins, W. D. (1917). The evolution of the elements and the stability of complex atoms. I. A new periodic system which shows a relation between the abundance of the elements and the structure of the nuclei of atomsmc. *Journal of the American Chemical Society*, *39*(5), 856-879. https://doi.org/10.1021/ja02250a002.

Haas, J. R., Shock, E. L., & Sassani, D. C. (1995). Rare earth elements in hydrothermal systems: estimates of standard partial molal thermodynamic properties of aqueous complexes of the rare earth

elements at high pressures and temperatures. *Geochimica et Cosmochimica Acta*, *59*(21), 4329-4350. https://doi.org/10.1016/0016-7037(95)00314-P.

Henderson, P. (Ed.). (2013). *Rare earth element geochemistry*. Elsevier.

Herrmann, A. G. (1970). Yttrium and lanthanides. In Hand- book of Geochemistry, Vol. II/2 (ed. K. H. Wedepohl), Springer. P. 39, 57-71-E-11.

Hieke Merlin, O. (1967). *I prodotti vulcanici del Monte Vulture (Lucania)*. Mem. Ist. Geol. Mineral. Univ. Padova, **26**, 3-66.

Hippolyte, J. C., Angelier, J., & Roure, F. B. (1994a). A major geodynamic change revealed by Quaternary stress patterns in the Southern Apennines (Italy). *Tectonophysics*, *230*(3-4), 199-210. https://doi.org/10.1016/0040-1951(94)90135-X.

Hippolyte, J. C., Angelier, J., Roure, F., & Casero, P. (1994b). Piggyback basin development and thrust belt evolution: structural and palaeostress analyses of Plio-Quaternary basins in the Southern Apennines. *Journal of Structural Geology*, *16*(2), 159-174.

Hollenstein, C., Kahle, H. G., Geiger, A., Jenny, S., Goes, S., & Giardini, D. (2003). New GPS constraints on the Africa-Eurasia plate boundary zone in southern Italy. *Geophysical Research Letters*, *30*(18). https://doi.org/10.1029/2003GL017554.

Janssen, R. P., & Verweij, W. (2003). Geochemistry of some rare earth elements in groundwater, Vierlingsbeek, The Netherlands. *Water Research*, *37*(6), 1320-1350. https://doi.org/10.1016/S0043-1354(02)00492-X.

Johannesson, K. H., & Hendry, M. J. (2000). Rare earth element geochemistry of groundwaters from a thick till and clay-rich aquitard sequence, Saskatchewan, Canada. *Geochimica et Cosmochimica Acta*, *64*(9), 1493-1509. https://doi.org/10.1016/S0016-7037(99)00402-0.

Johannesson, K. H., Chevis, D. A., Burdige, D. J., Cable, J. E., Martin, J. B., & Roy, M. (2011). Submarine groundwater discharge is an important net source of light and middle REEs to coastal waters of the Indian River Lagoon, Florida, USA. *Geochimica et Cosmochimica Acta*, *75*(3), 825-843. https://doi.org/10.1016/j.gca.2010.11.005.

Johannesson, K. H., Cortés, A., Leal, J. A. R., Ramírez, A. G., & Durazo, J. (2005). Geochemistry of rare earth elements in groundwaters from a rhyolite aquifer, central México. In *Rare earth elements in groundwater flow systems* (pp. 187-222). Springer, Dordrecht.

Johannesson, K. H., Farnham, I. M., Guo, C., & Stetzenbach, K. J. (1999). Rare earth element fractionation and concentration variations along a groundwater flow path within a shallow, basin-fill

aquifer, southern Nevada, USA. *Geochimica et Cosmochimica Acta*, *63*(18), 2697-2708. https://doi.org/10.1016/S0016-7037(99)00184-2.

Johannesson, K. H., Lyons, W. B., Yelken, M. A., Gaudette, H. E., & Stetzenbach, K. J. (1996). Geochemistry of the rare-earth elements in hypersaline and dilute acidic natural terrestrial waters: complexation behavior and middle rare-earth element enrichments. *Chemical Geology*, *133*(1-4), 125-144. https://doi.org/10.1016/S0009-2541(96)00072-1.

Johannesson, K. H., Stetzenbach, K. J., & Hodge, V. F. (1997a). Rare earth elements as geochemical tracers of regional groundwater mixing. *Geochimica et Cosmochimica Acta*, *61*(17), 3605-3618. https://doi.org/10.1016/S0016-7037(97)00177-4.

Johannesson, K. H., Stetzenbach, K. J., Hodge, V. F., Kreamer, D. K., & Zhou, X. (1997b). Delineation of Ground-Water Flow Systems in the Southern Great Basin Using Aqueous Rare Earth Element Distributions. *Groundwater*, *35*(5), 807-819. https://doi.org/10.1111/j.1745-6584.1997.tb00149.x.

Johannesson, K. H., Tang, J., Daniels, J. M., Bounds, W. J., & Burdige, D. J. (2004). Rare earth element concentrations and speciation in organic-rich blackwaters of the Great Dismal Swamp, Virginia, USA. *Chemical Geology*, *209*(3-4), 271-294. https://doi.org/10.1016/j.chemgeo.2004.06.012.

Johannesson, K. H., Zhou, X., Guo, C., Stetzenbach, K. J., & Hodge, V. F. (2000). Origin of rare earth element signatures in groundwaters of circumneutral pH from southern Nevada and eastern California, USA. *Chemical Geology*, *164*(3-4), 239-257. https://doi.org/10.1016/S0009-2541(99)00152-7. https://doi.org/10.1016/S0009-2541(99)00152-7.

Jones, A. P., Kostoula, T., Stoppa, F., & Woolley, A. R. (2000). Petrography and mineral chemistry of mantle xenoliths in a carbonate-rich melilititic tuff from Mt. Vulture volcano, southern Italy. *Mineralogical Magazine*, *64*(4), 593-613. https://doi.org/10.1180/002646100549634.

Kawabe, I., Ohta, A., & Miura, N. (1999). Distribution coefficients of REE between Fe oxyhydroxide precipitates and NaCl solutions affected by REE-carbonate complexation. *Geochemical journal*, *33*(3), 181-197. https://doi.org/10.2343/geochemj.33.181.

Klinkhammer, G., German, C. R., Elderfield, H., Greaves, M. J., & Mitra, A. (1994). Rare earth elements in hydrothermal fluids and plume particulates by inductively coupled plasma mass spectrometry. *Marine Chemistry*, *45*(3), 179-186. https://doi.org/10.1016/0304-4203(94)90001-9.

Kogarko, L. N., Williams, C. T., & Woolley, A. R. (2006). Compositional evolution and cryptic variation in pyroxenes of the peralkaline Lovozero intrusion, Kola Peninsula, Russia. *Mineralogical Magazine*, *70*(4), 347-359. https://doi.org/10.1180/0026461067040340.

Koeppenkastrop D., De Carlo E. H. (1992) Sorption of rare-earth elements from seawater onto synthetic mineral particles: An experimental approach. *Chemical Geology*, 95, 251-263.

Kulaksız, S., & Bau, M. (2013). Anthropogenic dissolved and colloid/nanoparticle-bound samarium, lanthanum and gadolinium in the Rhine River and the impending destruction of the natural rare earth element distribution in rivers. *Earth and Planetary Science Letters*, *362*, 43-50. https://doi.org/10.1016/j.epsl.2012.11.033.

Laurenzi, M. A. (1993). Mt. Vulture volcano chronostratigraphy and the effectiveness of dating young phlogopites. Abstracts (Oral presentation to) EUG 7°, Strasburgo, France, April 1993. In *Terra Abstract* (Vol. 5, pp. 572-573).

Lavecchia, G., & Creati, N. (2006). A mantle plume head trapped in the transition zone beneath the Mediterranean: a new idea. *Annals of Geophysics*, *49*(1 Suppl), 373-387.

Lavecchia, G., & Stoppa, F. (1996). The tectonic significance of Italian magmatism: an alternative view to the popular interpretation. *Terra Nova*, *8*(5), 435-446. https://doi.org/10.1111/j.1365-3121.1996.tb00769.x.

La Volpe, L., & Principe, C. (1989). Stratigrafia e storia eruttiva del Monte Vulture: revisione e aggiornamenti. *Bollettino GNV*, *2*, 809-902.

La Volpe, L., & Principe, C. (1991). Comments on "Monte Vulture Volcano (Basilicata, Italy): an analysis of morphology and volcaniclastic facies" by JE Guest, AM Duncan and DK Chester. *Bulletin of Volcanology*, *53*(3), 222-227.

La Volpe, L., Patella, D., Rapisardi, L., & Tramacere, A. (1984). The evolution of the Monte Vulture volcano (Southern Italy): inferences from volcanological, geological and deep dipole electrical soundings data. *Journal of volcanology and geothermal research*, *22*(3-4), 147-162. https://doi.org/10.1016/0377-0273(84)90001-5.

Lee, J. H., & Byrne, R. H. (1992). Examination of comparative rare earth element complexation behavior using linear free-energy relationships. *Geochimica et Cosmochimica Acta*, *56*(3), 1127-1137. https://doi.org/10.1016/0016-7037(92)90050-S.

Leybourne, M. I., & Johannesson, K. H. (2008). Rare earth elements (REE) and yttrium in stream waters, stream sediments, and Fe–Mn oxyhydroxides: fractionation, speciation, and controls over REE+ Y patterns in the surface environment. *Geochimica et Cosmochimica Acta*, *72*(24), 5962-5983. https://doi.org/10.1016/j.gca.2008.09.022.

Leybourne, M. I., Goodfellow, W. D., Boyle, D. R., & Hall, G. M. (2000). Rapid development of negative Ce anomalies in surface waters and contrasting REE patterns in groundwaters associated with Zn–Pb massive sulphide deposits. *Applied Geochemistry*, *15*(6), 695-723. https://doi.org/10.1016/S0883-2927(99)00096-7.

Lide, D.R., ed., 2004, CRC handbook of chemistry and physics (85th ed.): Boca Raton, Fla., CRC Press, 2,712 p.

Liu, H., Guo, H., Pourret, O., Chen, Y., & Yuan, R. (2019). Role of Manganese Oxyhydroxides in the Transport of Rare Earth Elements Along a Groundwater Flow Path. *International journal of environmental research and public health*, *16*(13), 2263. https://doi.org/10.3390/ijerph16132263.

Liu, H., Guo, H., Xing, L., Zhan, Y., Li, F., Shao, J., ... Li, C., (2016). Geochemical behaviors of rare earth elements in groundwater along a flow path in the North China Plain. *Journal of Asian Earth Sciences* 117, 33–51. https://doi.org/10.1016/j.jseaes.2015.11.021.

Liu, H., Pourret, O., Guo, H., & Bonhoure, J. (2017). Rare earth elements sorption to iron oxyhydroxide: Model development and application to groundwater. *Applied Geochemistry*, *87*, 158-166. https://doi.org/10.1016/j.apgeochem.2017.10.020.

Liu, H., Pourret, O., Guo, H., Martinez, R. E., & Zouhri, L. (2018). Impact of hydrous manganese and ferric oxides on the behavior of aqueous rare earth elements (REE): Evidence from a modeling approach and implication for the sink of REE. *International journal of environmental research and public health*, *15*(12), 2837. https://doi.org/10.3390/ijerph15122837.

Locardi, E., & Nicolich, R. (1988). Geodinamica del Tirreno e dell'Appennino centro-meridionale: la nuova carta della Moho. *Memorie della Società Geologica Italiana*, *41*, 121-140.

Luo, Y. R., & Byrne, R. H. (2004). Carbonate complexation of yttrium and the rare earth elements in natural waters. *Geochimica et Cosmochimica Acta*, *68*(4), 691-699. https://doi.org/10.1016/S0016-7037(03)00495-2.

Lustrino, M., Melluso, L., & Morra, V. (2000). The role of lower continental crust and lithospheric mantle in the genesis of Plio–Pleistocene volcanic rocks from Sardinia (Italy). *Earth and Planetary Science Letters*, *180*(3-4), 259-270. https://doi.org/10.1016/S0012-821X(00)00185-0.

Ma, L., Jin, L., & Brantley, S. L. (2011). How mineralogy and slope aspect affect REE release and fractionation during shale weathering in the Susquehanna/Shale Hills Critical Zone Observatory. *Chemical Geology*, *290*(1-2), 31-49. https://doi.org/10.1016/j.chemgeo.2011.08.013.

Malinverno, A., & Ryan, W. B. (1986). Extension in the Tyrrhenian Sea and shortening in the Apennines as result of arc migration driven by sinking of the lithosphere. *Tectonics*, *5*(2), 227-245. https://doi.org/10.1029/TC005i002p00227.

Mantovani, E., & Finetti, I. R. (2005). Evolutionary reconstruction of the Mediterranean region: extrusion tectonics driven by plate convergence. *Deep Seismic Exploration of the Central Mediterranean and Italy, CROP PROJECT*, *32*, 705-746.

Mantovani, E., Albarello, D., Tamburelli, C., Babbucci, D., & Viti, M. (1997). Plate convergence, crustal delamination, extrusion tectonics and minimization of shortening work as main controlling factors of the recent Mediterranean deformation pattern. *Annals of Geophysics*, *40*(3). https://doi.org/10.4401/ag-3894.

Mantovani, E., & Finetti, I. R. (2005). Evolutionary reconstruction of the Mediterranean region: extrusion tectonics driven by plate convergence. *Deep Seismic Exploration of the Central Mediterranean and Italy, CROP PROJECT, 32*, 705-746.

Mantovani, E., Albarello, D., Babbucci, D., & Tamburelli, C. (1993). Post-Tortonian Deformation Pattern in the Central Mediterranean: A Result of Extrusion Tectonics Driven by the Africa-Eurasia Convergence. In *Recent evolution and seismicity of the Mediterranean region* (pp. 65-104). Springer, Dordrecht.

Mantovani, E., Albarello, D., Babbucci, D., Tamburelli, C., & Viti, M. (2002). Trench-Arc-BackArc systems in the Mediterranean area: examples of extrusion tectonics. *Journal of the Virtual Explorer*, *8*, 131-147.

Mantovani, E., Viti, M., Babbucci, D., Tamburelli, C., & Albarello, D. (2006). Geodynamic connection between the indentation of Arabia and the Neogene tectonics of the central-eastern Mediterranean region. *SPECIAL PAPERS-GEOLOGICAL SOCIETY OF AMERICA*, *409*, 15.

Marini, L., Paiotti, A., Principe, C., Ferrara, G., & Cioni, R. (1994). Isotopic ratio and concentration of sulfur in the undersaturated alkaline magmas of Vulture Volcano (Italy). *Bulletin of Volcanology*, *56*(6-7), 487-492. https://doi.org/10.1007/BF00302829.

Marsac, R., Davranche, M., Gruau, G., Bouhnik-Le Coz, M., & Dia, A. (2011). An improved description of the interactions between rare earth elements and humic acids by modeling: PHREEQC-Model VI coupling. *Geochimica et Cosmochimica Acta*, *75*(19), 5625-5637. https://doi.org/10.1016/j.gca.2011.07.009.

Martinis, B. & Pieri, M. (1964). Alcune notizie sulla formazione evaporitica del Triassico superiore nell'Italia centrale e meridionale. *Memorie della Società Geologica Italiana, (**1**), 649- 678*.

Maschio, L., Ferranti, L., & Burrato, P. (2005). Active extension in Val d'Agri area, Southern Apennines, Italy: implications for the geometry of the seismogenic belt. *Geophysical Journal International*, *162*(2), 591-609. https://doi.org/10.1111/j.1365-246X.2005.02597.x.

Mattei, M., Petrocelli, V., Lacava, D., & Schiattarella, M. (2004). Geodynamic implications of Pleistocene ultrarapid vertical-axis rotations in the Southern Apennines, Italy. *Geology*, *32*(9), 789-792. https://doi.org/10.1130/G20552.1.

Mauro, A., & Schiattarella, M. (1988). L'unita silentina di base: Assetto strutturale, metamorfismo e significado tettonico nel quadro geologico dell'Appennino meridionale. *Memorie della Societa Geologica Italiana*, *41*, 1201-1213.

Mazzoli, S. (1992). *Structural analysis of the Mesozoic Lagonegro Units in SW Lucania (Southern Italian Apennines).* Studi Geologici Camerti, **12**, 117-147.

Mazzoli, S. (1993a). Structural analysis of the Mesozoic Lagonegro units in SW Lucania (Southern Apennines, Italy). Unpublished PhD thesis, Geologisches Institut ETH Zürich, 205 pp.

Mazzoli, S., & Helman, M. (1994). Neogene patterns of relative plate motion for Africa-Europe: some implications for recent central Mediterranean tectonics. In *Active Continental Margins—Present and Past* (pp. 464-468). Springer, Berlin, Heidelberg. https://doi.org/10.1007/978-3-662-38521-0_19.

Mazzoli, S., Aldega, L., Corrado, S., Invernizzi, C., & Zattin, M. (2006). Pliocene-quaternary thrusting, syn-orogenic extension and tectonic exhumation in the Southern Apennines (Italy): Insights from the Monte Alpi area. *SPECIAL PAPERS-GEOLOGICAL SOCIETY OF AMERICA*, *414*, 55.

Mazzoli, S., Barkham, S., Cello, G., Gambini, R., Mattioni, L., Shiner, P., & Tondi, E. (2001). Reconstruction of continental margin architecture deformed by the contraction of the Lagonegro Basin, southern Apennines, Italy. *Journal of the Geological Society*, *158*(2), 309-319. https://doi.org/10.1144/jgs.158.2.309.

McLennan. (1989). Rare earth elements in sedimentary rocks: influence of provenance and sedimentary processes. *Geochemistry and Mineralogy of Rare Earth Elements, Reviews in Mineralogy 21*, 169-200.

McLennan, S. M. (1994). Rare earth element geochemistry and the “tetrad” effect. *Geochimica et Cosmochimica Acta*, *58*(9), 2025-2033. https://doi.org/10.1016/0016-7037(94)90282-8.

McKay, G. A. (1989). Partitioning of rare earth elements between major silicate minerals and basaltic melts. *Geochemistry and mineralogy of rare earth elements*.

Meletti, C., Patacca, E., & Scandone, P. (2000). Construction of a seismotectonic model: the case of Italy. *Pure and applied Geophysics*, *157*(1-2), 11-35. https://doi.org/10.1007/PL00001089.

Melluso, L., Morra, V., & Di Girolamo, P. (1996). The Mt. Vulture volcanic complex (Italy): evidence for distinct parental magmas and for residual melts with melilite. *Mineralogy and Petrology*, *56*(3-4), 225-250. https://doi.org/10.1007/BF01162605.

Michard, A., Albarede, F., Michard, G., Minster, J. F., & Charlou, J. L. (1983). Rare-earth elements and uranium in high-temperature solutions from East Pacific Rise hydrothermal vent field (13 N). *Nature*, *303*(5920), 795-797.

Migdisov, A. A., Williams-Jones, A. E., & Wagner, T. (2009). An experimental study of the solubility and speciation of the Rare Earth Elements (III) in fluoride-and chloride-bearing aqueous solutions at temperatures up to 300 C. *Geochimica et Cosmochimica Acta*, *73*(23), 7087-7109. https://doi.org/10.1016/j.gca.2009.08.023.

Möller, P. (2002). Rare earth elements and yttrium in geothermal fluids. *Water Science and Technology Library*, *40*, 97-125.

Moeller, P., Rosenthal, E., Dulski, P., Geyer, S., & Guttman, Y. (2003). Rare earths and yttrium hydrostratigraphy along the Lake Kinneret–Dead Sea–Arava transform fault, Israel and adjoining territories. *Applied Geochemistry*, *18*(10), 1613-1628. https://doi.org/10.1016/S0883-2927(03)00044-1.

Moffett, J. W. (1990). Microbially mediated cerium oxidation in sea water. *Nature*, *345*(6274), 421-423.

Moffett, J. W. (1994a). A radiotracer study of cerium and manganese uptake onto suspended particles in Chesapeake Bay. *Geochimica et Cosmochimica Acta*, *58*(2), 695-703. https://doi.org/10.1016/0016-7037(94)90499-5.

Moffett, J. W. (1994b). The relationship between cerium and manganese oxidation in the marine environment. *Limnology and Oceanography*, *39*(6), 1309-1318.

Monaco, C. (1993). Pleistocene strike-slip tectonics in the Pollino mountain range (Southern Italy). *Annales Tectonicae*, **7**, 100-112.

Monaco, C., & Tortorici, L. (1995). Tectonic role of ophiolite-bearing terranes in the development of the Southern Apennines orogenic belt. *Terra Nova*, *7*(2), 153-160. https://doi.org/10.1111/j.1365-3121.1995.tb00684.x.

Mongelli, G., Paternoster, M., Rizzo, G., Sansone, M. T. C., & Sinisi, R. (2013). Trace element geochemistry of the Mt Vulture carbonatites, southern Italy. *International Geology Review*, *55*(12), 1541-1552. https://doi.org/10.1080/00206814.2013.786310.

Mongelli, G., Paternoster, M., Rizzo, G., & Sinisi, R. (2014). Trace elements and REE fractionation in subsoils developed on sedimentary and volcanic rocks: case study of the Mt. Vulture area, southern Italy. *International Journal of Earth Sciences*, *103*(4), 1125-1140. https://doi.org/10.1007/s00531-014-1003-z.

Montone, P., Mariucci, M. T., Pondrelli, S., & Amato, A. (2004). An improved stress map for Italy and surrounding regions (central Mediterranean). *Journal of Geophysical Research: Solid Earth*, *109*(B10). https://doi.org/10.1029/2003JB002703.

Monaco, C., Tortorici, L., & Paltrinieri, W. (1998). Structural evolution of the Lucanian Apennines, southern Italy. *Journal of Structural Geology*, *20*(5), 617-638. https://doi.org/10.1016/S0191-8141(97)00105-3.

Mostardini, F. and Merlini, S. (1986). *Appennino Centro Meridionale*. *Sezioni geologiche e proposta di modello strutturale.* AGIP, Rome.

Munemoto, T., Ohmori, K., & Iwatsuki, T. (2015). Rare earth elements (REE) in deep groundwater from granite and fracture-filling calcite in the Tono area, central Japan: Prediction of REE fractionation in paleo-to present-day groundwater. *Chemical Geology*, *417*, 58-67. https://doi.org/10.1016/j.chemgeo.2015.09.024.

Nathenson, M., Thompson, J. M., & White, L. D. (2003). Slightly thermal springs and non-thermal springs at Mount Shasta, California: Chemistry and recharge elevations. *Journal of Volcanology and Geothermal Research*, *121*(1-2), 137-153. https://doi.org/10.1016/S0377-0273(02)00426-2.

Négrel, P., Guerrot, C., Cocherie, A., Azaroual, M., Brach, M., & Fouillac, C. (2000). Rare earth elements, neodymium and strontium isotopic systematics in mineral waters: evidence from the Massif Central, France. *Applied Geochemistry*, *15*(9), 1345-1367. https://doi.org/10.1016/S0883-2927(00)00008-1.

Noack, C. W., Dzombak, D. A., & Karamalidis, A. K. (2014). Rare earth element distributions and trends in natural waters with a focus on groundwater. *Environmental science & technology*, *48*(8), 4317-4326. https://doi.org/10.1021/es4053895.

Ogniben, L. (1969). Schema introduttivo alla geologia del confine calabro-lucano. *Mem. Soc. Geol. It.*, *8*, 453-763.

Ohta, A., & Kawabe, I. (2000). Rare earth element partitioning between Fe oxyhydroxide precipitates and aqueous NaCl solutions doped with NaHCO3: Determinations of rare earth element complexation constants with carbonate ions. *Geochemical Journal*, *34*(6), 439-454. https://doi.org/10.2343/geochemj.34.439.

Ohta, A., & Kawabe, I. (2001). REE (III) adsorption onto Mn dioxide (δ-MnO2) and Fe oxyhydroxide: Ce (III) oxidation by δ-MnO2. *Geochimica et Cosmochimica Acta*, *65*(5), 695-703. https://doi.org/10.1016/S0016-7037(00)00578-0.

Ohta, A., Kagi, H., Tsuno, H., Nomura, M., & Kawabe, I. (2008). Influence of multi-electron excitation on EXAFS spectroscopy of trivalent rare-earth ions and elucidation of change in hydration number through the series. *American Mineralogist*, *93*(8-9), 1384-1392. https://doi.org/10.2138/am.2008.2628.

Ojiambo, S. B., Lyons, W. B., Welch, K. A., Poreda, R. J., & Johannesson, K. H. (2003). Strontium isotopes and rare earth elements as tracers of groundwater–lake water interactions, Lake Naivasha, Kenya. *Applied Geochemistry*, *18*(11), 1789-1805. https://doi.org/10.1016/S0883-2927(03)00104-5.

Ökeler, A., Gu, Y. J., Lerner-Lam, A., & Steckler, M. S. (2009). Seismic structure of the southern Apennines as revealed by waveform modelling of regional surface waves. *Geophysical Journal International*, *178*(3), 1473-1492. https://doi.org/10.1111/j.1365-246X.2009.04229.x.

Oliveri, Y., Cangemi, M., Capasso, G., & Saiano, F. (2019). Pathways and fate of REE in the shallow hydrothermal aquifer of Vulcano island (Italy). *Chemical Geology*, *512*, 121-129. https://doi.org/10.1016/j.chemgeo.2019.02.037.

Ortolani, F., Pagliuca, S., Pepe, E., Schiattarella, M., & Toccaceli, R. M. (1992). Active tectonics in the Southern Apennines: Relationships between cover geometries and basement structure. A hypothesis for a geodynamic model. *Contributions to the Geology of Italy with special regard to the Paleozoic basements, IGCP*, (276), 413-419.

Otsuka, M., & Terakado, Y. (2003). Rare earth element abundances in high phosphorus and low iron groundwaters from the Nishinomiya district, Japan: Variations in Ce anomaly, redox state and heavy rare earth enrichment. *Geochemical journal*, *37*(1), 1-19. https://doi.org/10.2343/geochemj.37.1.

Parkhurst, D.L., (1995). User's Guide to PHREEQC, a computer model for speciation, reaction-path, advective-transport and inverse geochemical calculations. *US Geological Survey Water-Resources Investigations Report 95-4227*.

Parkhurst, D.L. and Appelo, C.A.J., (1999). User's Guide to PHREEQC (version 2), a computer program for speciation, batch-reaction, one-dimensional transport and inverse geochemical calculations. *US Geological Survey Water-Resources Investigations Report 99-4259*.

Panina, L. I., Stoppa, F., & Usol tseva, L. M. (2003). Genesis of melilitite rocks of Pian di Celle volcano, Umbrian kamafugite province, Italy: evidence from melt inclusions in minerals. *PETROLOGY C/C OF PETROLOGIIA*, *11*(4), 365-382.

Panza, G. F., Peccerillo, A., Aoudia, A., & Farina, B. (2007). Geophysical and petrological modelling of the structure and composition of the crust and upper mantle in complex geodynamic settings: the Tyrrhenian Sea and surroundings. *Earth-Science Reviews*, *80*(1-2), 1-46. https://doi.org/10.1016/j.earscirev.2006.08.004.

Parisi, S. (2009). Hydrogeochemical tracing of the groundwater flow pathways in the Mount Vulture volcanic aquifer system (Basilicata, Southern Italy). *PhD thesis*.

Parisi, S., Paternoster, M., Kohfahl, C., Pekdeger, A., Meyer, H., Hubberten, H. W., ... & Mongelli, G. (2011a). Groundwater recharge areas of a volcanic aquifer system inferred from hydraulic,

hydrogeochemical and stable isotope data: Mount Vulture, southern Italy. *Hydrogeology journal*, *19*(1), 133-153. https://doi.org/10.1007/s10040-010-0619-8.

Parisi, S., Paternoster, M., Perri, F., & Mongelli, G. (2011b). Source and mobility of minor and trace elements in a volcanic aquifer system: Mt. Vulture (southern Italy). *Journal of geochemical exploration*, *110*(3), 233-244. https://doi.org/10.1016/j.gexplo.2011.06.010.

Patacca, E., & Scandone, P. (1989). Post-Tortonian mountain building in the Apennines. The role of the passive sinking of a relic lithospheric slab. http://hdl.handle.net/11568/172693.

Patacca, E., & Scandone, P. (2007). Geology of the southern Apennines. *Bollettino della Società Geologica Italiana*, *7*, 75-119. https://www.researchgate.net/publication/267507693.

Patacca, E., Sartori, R. and Scandone, P. (1990) - *Tyrrhenian basin and Apenninic arcs: kinematic relations since Late Tortonian times*. Mem. Soc. Geol. It., **45**, 425-451.

Paternoster, M. (2019). Boron Isotopes in the Mount Vulture Groundwaters (Southern Italy): Constraints for the Assessment of Natural and Anthropogenic Contaminant Sources. *Geofluids*, *2019*. https://doi.org/10.1155/2019/9107636.

Paternoster, M., Mongelli, G., Caracausi, A., & Favara, R. (2016). Depth influence on the distribution of chemical elements and saturation index of mineral phases in twins maar lakes: The case of the Monticchio lakes (southern Italy). *Journal of Geochemical Exploration*, *163*, 10-18. https://doi.org/10.1016/j.gexplo.2016.01.001.

Paternoster, M., Parisi, S., Caracausi, A., Favara, R., & Mongelli, G. (2010). Groundwaters of Mt. Vulture volcano, southern Italy: chemistry and sulfur isotope composition of dissolved sulfate. *Geochemical Journal*, *44*(2), 125-135. https://doi.org/10.2343/geochemj.1.0050.

Patino, L. C., Velbel, M. A., Price, J. R., & Wade, J. A. (2003). Trace element mobility during spheroidal weathering of basalts and andesites in Hawaii and Guatemala. *Chemical Geology*, *202*(3-4), 343-364. https://doi.org/10.1016/j.chemgeo.2003.01.002.

Peccerillo, A. (2001). Geochemical similarities between the Vesuvius, Phlegraean Fields and Stromboli Volcanoes: petrogenetic, geodynamic and volcanological implications. *Mineralogy and Petrology*, *73*(1-3), 93-105. https://doi.org/10.1007/s007100170012.

Peccerillo, A. (2005). *Plio-quaternary volcanism in Italy* (Vol. 365). New York: Springer-Verlag Berlin Heidelberg.

Peccerillo, A., & Manetti, P. (1985). The potassium alkaline volcanism of central-southern Italy: a review of the data relevant to petrogenesis and geodynamic significance. *Verhandelinge van die Geologiese Vereniging van Suid-Afrika*, *88*(2), 379-394.

Pescatore, T. (1978). Evoluzione tettonica del Bacino Irpino (Italia Meridionale) durante il Miocene. *Boll. Soc. Geol. Ital.*, **97**, 783–805.

Pescatore, T., Renda, P., Schiattarella, M., & Tramutoli, M. (1999). Stratigraphic and structural relationships between Meso-Cenozoic Lagonegro basin and coeval carbonate platforms in southern Apennines, Italy. *Tectonophysics*, *315*(1-4), 269-286. https://doi.org/10.1016/S0040-1951(99)00278-4.

Pieri, P., Vitale, G., Beneduce, P., Doglioni, C., Gallicchio, S., Giano, S. I., ... & Schiattarella, M. (1997b). Quaternary tectonics in the Bradanic-Ionian area (Southern Italy). *Il Quaternario, Italian Journal of Quaternary Sciences*, *10*(2), 535-542.

Pondrelli, S., Morelli, A., Ekström, G., Mazza, S., Boschi, E., & Dziewonski, A. M. (2002). European–Mediterranean regional centroid-moment tensors: 1997–2000. *Physics of the Earth and Planetary Interiors*, *130*(1-2), 71-101. https://doi.org/10.1016/S0031-9201(01)00312-0.

Pondrelli, S., Salimbeni, S., Ekström, G., Morelli, A., Gasperini, P., & Vannucci, G. (2006). The Italian CMT dataset from 1977 to the present. *Physics of the Earth and Planetary Interiors*, *159*(3-4), 286-303. https://doi.org/10.1016/j.pepi.2006.07.008.

Pourret, O., & Davranche, M. (2013). Rare earth element sorption onto hydrous manganese oxide: A modeling study. *Journal of colloid and interface science*, *395*, 18-23. https://doi.org/10.1016/j.jcis.2012.11.054.

Pourret, O., Gruau, G., Dia, A., Davranche, M., & Molenat, J. (2010). Colloidal control on the distribution of rare earth elements in shallow groundwaters. *Aquatic Geochemistry*, *16*(1), 31. https://doi.org/10.1007/s10498-009-9069-0.

Principe, C. & Giannandrea, P. (2002). Stratigrafia ed evoluzione geologica del vulcano Vulture (Basilicata, Italia). Rapporti fra vulcanismo ed ambienti sedimentari. In: Cinematiche collisionali: tra esumazione e sedimentazione. *81° riunione estiva della Società Geologica Italiana, Torino 10-12 Settembre 2002, volume riassunti, 280-281*.

Principe C. & Giannandrea P. (2006). *Storia evolutiva del monte Vulture.* La geologia del Monte Vulture. Regione Basilicata. Grafiche Finiguerra Lavello, 217 pp.

Principe, C., & Stoppa, F. (1994). Caratteristiche litologiche delle piroclastiti associate alla genesi dei maar di Monticchio: prima segnalazione di depositi carbonatifico-melilititici al M. *Vulture (Basilicata). Plinius*, *12*, 86-90.

Prosser, G., Schiattarella, M., Tramutoli, M., Doglioni, C., Harabaglia, P., & Bigozzi, A. (1996, February). Una sezione rappresentativa dell'Appennino meridionale. In *Proceedings of the Conferenza Sulla Ricerca Scientifica in Basilicata* (pp. 150-154).

Quinn, K. A., Byrne, R. H., & Schijf, J. (2006). Sorption of yttrium and rare earth elements by amorphous ferric hydroxide: influence of temperature. *Environmental science & technology*, *41*(2), 541-546. https://doi.org/10.1021/es0618191.

Reed M.J. (1983). *Introduction*. In: Reed, M.J., (Ed.), Assessment of Low-temperature Geothermal Resources of the United States - 1982. *U.S. Geol. Surv. Circ*. 892, 1-8.

Roaldset, E. (1975). Rare earth element distributions in some Precambrian rocks and their phyllosilicates, Numedal, Norway. *Geochimica et Cosmochimica Acta*, *39*(4), 455-469. https://doi.org/10.1016/0016-7037(75)90100-3.

Romano, P. (1992). La distribuzione dei depositi marini pleistocenici lungo le coste della Campania. Stato delle conoscenze e prospettive di ricerca. *Studi Geologici Camerti, Special Volume*, 265-269.

Rosatelli, G., Stoppa, F., & Jones, A. P. (2000). Intrusive calcite-carbonatite occurrence from Mt. Vulture volcano, southern Italy. *Mineralogical Magazine*, *64*(4), 615-624. https://doi.org/10.1180/002646100549643.

Rosenbaum, G., & Lister, G. S. (2004). Neogene and Quaternary rollback evolution of the Tyrrhenian Sea, the Appennines, and the Sicilian Maghrebides: Tectonicas, v. 23. *TC, 1013*. doi:10.1029/2003TC001518.

Rosenbaum, G., Gasparon, M., Lucente, F. P., Peccerillo, A., & Miller, M. S. (2008). Kinematics of slab tear faults during subduction segmentation and implications for Italian magmatism. *Tectonics*, *27*(2). https://doi.org/10.1029/2007TC002143.

Ryan, P. D., Harper, D. A. T., & Whalley, J. S. (1995). PALSTAT, Statistics for palaeontologists. *Champman & Hall, London*.

Salvador, A. (1987). Unconformity-bounded stratigraphic units. *Geological Society of American Bulletin* **98**, 232-237.

Salvador, A. (1994) – International stratigraphic guide. *International Union of Geological Sciences, Trondheim, Norway, and Geological Society of America, Boulder*, 214.

Sartori, R. (1989). Evoluzione neogenico-recente del bacino tirrenico e suoi rapporti con la geologia delle aree circostanti. *Giornale di Geologia*, *51*(2), 1-39.

Sartori, R., Torelli, L., Zitellini, N., Carrara, G., Magaldi, M., & Mussoni, P. (2004). Crustal features along a W–E Tyrrhenian transect from Sardinia to Campania margins (Central Mediterranean). *Tectonophysics*, *383*(3-4), 171-192. https://doi.org/10.1016/j.tecto.2004.02.008.

Scandone, P. (1967). *Studi di geologia lucana: la serie calcareo-silico-marnosa e i suoi rapporti con l'Appennino calcareo*. Boll. Soc. Natur. Napoli, **76**, 301-469.

Scandone, P. (1972). Studi di geologia lucana: Carta dei terreni della serie calcareo-silicomarnosa e note illustrative. *Boll. Soc. Natur. in Napoli*, *81*, 225-300.

Scandone, P. (1982). Structure and evolution of the Calabrian Arc.

Schiano, P., Clocchiatti, R., Ottolini, L., & Busa, T. (2001). Transition of Mount Etna lavas from a mantle-plume to an island-arc magmatic source. *Nature*, *412*(6850), 900-904. https://doi.org/10.1038/35091056.

Schiattarella, M. (1996). Tettonica della Catena del Pollino (confine calabro-lucano). *Mem. Soc. Geol. It*, *51*, 543-566.

Schiattarella, M. (1998). Quaternary tectonics of the Pollino ridge, Calabria-Lucania boundary, southern Italy. *Geological Society, London, Special Publications*, *135*(1), 341-354. https://doi.org/10.1144/GSL.SP.1998.135.01.22.

Schiattarella, M., Beneduce, P., Di Leo, P., Giano, S. I., Giannandrea, P., & Principe, C. (2005). Assetto strutturale ed evoluzione morfotettonica quaternaria del vulcano del Monte Vulture (Appennino lucano). *Bollettino-Società Geologica Italiana*, *124*(3), 543.

Schiattarella, M., Di Leo, P., Beneduce, P., & Giano, S. I. (2003). Quaternary uplift vs tectonic loading: a case study from the Lucanian Apennine, southern Italy. *Quaternary International*, *101*, 239-251. https://doi.org/10.1016/S1040-6182(02)00126-X.

Schijf, J., & Byrne, R. H. (2004). Determination of SO4β1 for yttrium and the rare earth elements at I= 0.66 m and t= 25 C—implications for YREE solution speciation in sulfate-rich waters. *Geochimica et Cosmochimica Acta*, *68*(13), 2825-2837. https://doi.org/10.1016/j.gca.2003.12.003.

Scrocca, D. (2006). Thrust front segmentation induced by differential slab retreat in the Apennines (Italy). *Terra Nova*, *18*(2), 154-161. https://doi.org/10.1111/j.1365-3121.2006.00675.x.

Serpelloni, E., Anzidei, M., Baldi, P., Casula, G., & Galvani, A. (2005). Crustal velocity and strain-rate fields in Italy and surrounding regions: new results from the analysis of permanent and non-permanent GPS networks. *Geophysical Journal International*, *161*(3), 861-880. https://doi.org/10.1111/j.1365-246X.2005.02618.x.

Serpelloni, E., Anzidei, M., Baldi, P., Casula, G., & Galvani, A. (2006). GPS measurement of active strains across the Apennines. *Ann. Geophys*, *49*(1), 319-329.

Serri, G., Innocenti, F., & Manetti, P. (1993). Geochemical and petrological evidence of the subduction of delaminated Adriatic continental lithosphere in the genesis of the Neogene-Quaternary magmatism of central Italy. *Tectonophysics*, *223*(1-2), 117-147. https://doi.org/10.1016/0040-1951(93)90161-C.

Serri, G., Innocenti, F., & Manetti, P. (2001). Magmatism from Mesozoic to Present: petrogenesis, time-space distribution and geodynamic implications. In *Anatomy of an Orogen: the Apennines and adjacent Mediterranean Basins* (pp. 77-103). Springer, Dordrecht. https://doi.org/10.1007/978-94-015-9829-3_8.

Shannon, R. D. (1976). Revised effective ionic radii and systematic studies of interatomic distances in halides and chalcogenides. *Acta crystallographica section A: crystal physics, diffraction, theoretical and general crystallography*, *32*(5), 751-767. https://doi.org/10.1107/S0567739476001551. https://doi.org/10.1107/S0567739476001551

Sholkovitz, E. R. (1995). The aquatic chemistry of rare earth elements in rivers and estuaries. *Aquatic Geochemistry*, *1*(1), 1-34.

Sholkovitz, E. R., Landing, W. M., & Lewis, B. L. (1994). Ocean particle chemistry: the fractionation of rare earth elements between suspended particles and seawater. *Geochimica et Cosmochimica Acta*, *58*(6), 1567-1579. https://doi.org/10.1016/0016-7037(94)90559-2.

Sinisi, R., Petrullo, A. V., Agosta, F., Paternoster, M., Belviso, C., & Grassa, F. (2016). Contrasting fault fluids along high-angle faults: a case study from Southern Apennines (Italy). *Tectonophysics*, *690*, 206-218. https://doi.org/10.1016/j.tecto.2016.07.023.

Smedley, P.L., 1991. The geochemistry of rare earth elements in groundwater from the Carnmenellis area, southwest England. *Geochim. Cosmochim. Acta*, 55(10), 2767–2779. https://doi.org/10.1016/0016-7037(91)90443-9.

Spilotro, G., Canora, F., Caporale, F., Caputo, R., Fidelibus, M. D., & Leandro, G. (2006). Idrogeologia del M. Vulture (Basilicata, Italia). *Aquifer Vulnerability and Risk, 2nd International Workshop. 4th Congress on the Protection and Management of Groundwater, Colorno (Italia) (September 2005)*, pp. 21-23

Spilotro, G., Canora, F., Caporale, F., Caputo, R., Fidelibus, M. D., & Leandro, G. (2006). Idrogeologia del Monte Vulture [Hydrogeology of M. Vulture]. *La geologia del Monte Vulture [The geology of the Mount Vulture]. Regione Basilicata, Potenza, Italy*, 123-132.

Steinmann, M., & Stille, P. (2008). Controls on transport and fractionation of the rare earth elements in stream water of a mixed basaltic–granitic catchment basin (Massif Central, France). *Chemical Geology*, *254*(1-2), 1-18. https://doi.org/10.1016/j.chemgeo.2008.04.004.

Stolpe, B., Guo, L., & Shiller, A. M. (2013). Binding and transport of rare earth elements by organic and iron-rich nanocolloids in Alaskan rivers, as revealed by field-flow fractionation and ICP-MS. *Geochimica et Cosmochimica Acta*, *106*, 446-462. https://doi.org/10.1016/j.gca.2012.12.033.

Stoppa, F. (1988). L'euremite di Colle Fabbri (Spoleto): un litotipo ad affinità carbonatitica in Italia. *Boll. Soc. Geol. It.*, ***107***, *239-248.*

Stoppa, F. (2003). Consensus and open questions about Italian CO2-driven magma from the mantle. *Period. Mineral*, *1*, 1-8.

Stoppa, F., & Cundari, A. (1995). A new Italian carbonatite occurrence at Cupaello (Rieti) and its genetic significance. *Contributions to Mineralogy and Petrology*, *122(3), 275-288.* https://doi.org/10.1007/s004100050127.

Stoppa, F., & Lavecchia, G. (1992). Late Pleistocene ultra-alkaline magmatic activity in the Umbria-Latium region (Italy): an overview. *Journal of Volcanology and Geothermal Research, 52(4), 277-293.* https://doi.org/10.1016/0377-0273(92)90049-J.

Stoppa, F., & Lupini, L. (1993). Mineralogy and petrology of the Polino monticellite calciocarbonatite (Central Italy). *Mineralogy and Petrology, 49(3-4), 213-231*. https://doi.org/10.1007/BF01164595.

Stoppa, F., & Principe, C. (1997). Eruption style and petrology of a new carbonatitic suite from the Mt. Vulture Southern Italy: The Monticchio Lakes Formation. *Journal of volcanology and geothermal research, 78(3-4), 251-265.* https://doi.org/10.1016/S0377-0273(97)00004-8.

Stoppa, F., & Woolley, A. R. (1997). The Italian carbonatites: field occurrence, petrology and regional significance. *Mineralogy and Petrology*, *59*(1-2), 43-67. https://doi.org/10.1007/BF01163061.

Stoppa, F., Principe, C., & Giannandrea, P. (2008). Comments on: Carbonatites in a subduction system: The Pleistocene alvikites from Mt. Vulture (southern Italy) by D'Orazio et al.,(2007). *Lithos*, *103*(3-4), 550-556. doi:10.1016/j.lithos.2007.10.012.

Takahashi, Y., Yoshida, H., Sato, N., Hama, K., Yusa, Y., & Shimizu, H. (2002). W-and M-type tetrad effects in REE patterns for water–rock systems in the Tono uranium deposit, central Japan. *Chemical geology*, *184*(3-4), 311-335. https://doi.org/10.1016/S0009-2541(01)00388-6.

Tang, J., Johannesson, K.H., 2003. Speciation of rare earth elements in natural terrestrial waters: assessing the role of dissolved organic matter from the modeling approach. *Geochim. Cosmochim. Acta* 67 (13), 2321–2339. https://doi.org/10.1016/S0016-7037(02)01413-8.

Tang, J., & Johannesson, K. H. (2006). Controls on the geochemistry of rare earth elements along a groundwater flow path in the Carrizo Sand aquifer, Texas, USA. *Chemical Geology*, *225*(1-2), 156-171. https://doi.org/10.1016/j.chemgeo.2005.09.007.

Taylor, S. R., & McLennan, S. M. (1985). The continental crust: its composition and evolution. *Blackwell Science Publishers Taylor and McLennan*.

Torrente, M. M. (1990). Folding and thrusting in the calcareo-silico-marnosa sequence (Lagonegro area, southern Apennine). *Memorie della Società Geologica Italiana*, *45*, 511-517.

Trua, T., Serri, G., & Marani, M. P. (2003). Lateral flow of African mantle below the nearby Tyrrhenian plate: geochemical evidence. *Terra Nova*, *15*(6), 433-440. https://doi.org/10.1046/j.1365-3121.2003.00509.x.

Turco, E., & Zuppetta, A. (1998). A kinematic model for the Plio-Quaternary evolution of the Tyrrhenian–Apenninic system: implications for rifting processes and volcanism. *Journal of Volcanology and Geothermal Research*, *82*(1-4), 1-18. https://doi.org/10.1016/S0377-0273(97)00055-3.

Turco, E., Maresca, R., & Cappadona, P. (1990). La tettonica plio-pleistocenica del confine calabro-lucano: modello cinematico. *Memorie della Societa Geologica Italiana*, *45*, 519-529.

Tweed, S. O., Weaver, T. R., Cartwright, I., & Schaefer, B. (2006). Behavior of rare earth elements in groundwater during flow and mixing in fractured rock aquifers: an example from the Dandenong Ranges, southeast Australia. *Chemical geology*, *234*(3-4), 291-307. https://doi.org/10.1016/j.chemgeo.2006.05.006.

Van Dijk, J. P., & Scheepers, P. J. J. (1995). Neotectonic rotations in the Calabrian Arc; implications for a Pliocene-Recent geodynamic scenario for the Central Mediterranean. *Earth-Science Reviews*, *39*(3-4), 207-246. https://doi.org/10.1016/0012-8252(95)00009-7.

Van Gosen, B. S., Verplanck, P. L., Seal II, R. R., Long, K. R., & Gambogi, J. (2017). *Rare-earth elements* (No. 1802-O). US Geological Survey. https://doi.org/10.3133/pp1802O.

Vázquez-Ortega, A., Perdrial, J., Harpold, A., Zapata-Ríos, X., Rasmussen, C., McIntosh, J., ... & Chorover, J. (2015). Rare earth elements as reactive tracers of biogeochemical weathering in forested rhyolitic terrain. *Chemical Geology*, *391*, 19-32. https://doi.org/10.1016/j.chemgeo.2014.10.016.

Ventura, G., Cinti, F. R., Di Luccio, F., & Pino, N. A. (2007). Mantle wedge dynamics versus crustal seismicity in the Apennines (Italy). *Geochemistry, Geophysics, Geosystems*, *8*(2). https://doi.org/10.1029/2006GC001421.

Viti, M., Mantovani, E., Babbucci, D., & Tamburelli, C. (2006). Quaternary geodynamics and deformation pattern in the Southern Apennines; implications for seismic activity. *Bollettino della Società Geologica Italiana*, *125*(3), 273-291.

Washington, H. S. (1906). *The Roman comagmatic region* (No. 57). Carnegie Institution of Washington.

Weber, R. J. (2008). *An experimental study of fractionation of the rare earth elements in poplar plants (Populus eugenei) grown in a calcium-bearing smectite soil* (Doctoral dissertation, Kansas State University).

Westaway, R. (1992). Seismic moment summation for historical earthquakes in Italy: tectonic implications. *Journal of Geophysical Research: Solid Earth*, *97*(B11), 15437-15464. https://doi.org/10.1029/92JB00946.

Westaway, R. (1993). Quaternary uplift of southern Italy. *Journal of Geophysical Research: Solid Earth*, *98*(B12), 21741-21772. https://doi.org/10.1029/93JB01566.

Willis, S. S., & Johannesson, K. H. (2011). Controls on the geochemistry of rare earth elements in sediments and groundwaters of the Aquia aquifer, Maryland, USA. *Chemical Geology*, *285*(1-4), 32-49. https://doi.org/10.1016/j.chemgeo.2011.02.020.

Wilson, M., & Bianchini, G. (1999). Tertiary-Quaternary magmatism within the Mediterranean and surrounding regions. *SPECIAL PUBLICATION-GEOLOGICAL SOCIETY OF LONDON*, *156*, 141-168.

Worrall, F., & Pearson, D. G. (2001). Water-rock interaction in an acidic mine discharge as indicated by rare earth element patterns. *Geochimica et Cosmochimica Acta*, *65*(18), 3027-3040. https://doi.org/10.1016/S0016-7037(01)00662-7.

Wortel, M. J. R., & Spakman, W. (2000). Subduction and slab detachment in the Mediterranean-Carpathian region. *Science*, *290*(5498), 1910-1917. DOI: 10.1126/science.290.5498.1910.

Yuan, J., Mao, X., Wang, Y., Deng, Z., & Huang, L. (2014). Geochemistry of rare-earth elements in shallow groundwater, northeastern Guangdong Province, China. *Chinese Journal of Geochemistry*, *33*(1), 53-64. https://doi.org/10.1007/s11631-014-0659-1.